Università degli Studi di Firenze
Dipartimento di Fisica e Astronomia

Scuola di Dottorato in Scienze
Dottorato di Ricerca in Fisica - XXIII ciclo
SSD FIS/01 Fisica Sperimentale

Dissertation in Physics

to Obtain the Degree of

Dottore di Ricerca
in Fisica

Title:

Advances In Diamond-based Heterostructures

presented by

Stefano Lagomarsino

Supervisor Silvio Sciortino

Coordinator Alessandro Cuccoli

December 2010

"Sow your seed in the morning and do not be idle in the evening, for you do not know whether morning or evening sowing will succeed, or whether both of them alike will be good." (Book of Ecclesiastes, chapter 11, verse 6)

Contents

I Silicon On Diamond laser bonding 9

1 Why bonding silicon to diamond and how 11
1.1 Motivations of the research on the subject 11
1.1.1 Silicon-On-Diamond as heat spreader 12
1.1.2 Silicon-On-Diamond as radiation detector 12
1.1.3 Silicon-On-Diamond as bio-electrode 13
1.2 Methods for Silicon-on-Diamond fabrication 15
1.2.1 Diamond growth on silicon substrates 15
1.2.2 High temperature and pressure method 18

2 Silicon-on-Diamond by pulsed laser irradiation 23
2.1 Bonding apparatus and experiments 24
2.1.1 Preliminary study 24
2.1.2 Experimental set-up 27
2.1.3 Samples and bonding experiments 30
2.2 Functional tests 30
2.2.1 Tensile strength tests 32
2.2.2 Thermal conductivity tests 33
2.3 Structural characterization of the interface 35
2.3.1 Electron Microscopy 36
2.3.2 Micro-Raman analysis 38
2.3.3 Fourier Transform Infrared Analysis 40

2.4 Conclusions and perspectives 43

3 Modeling of laser bonding 45

3.1 Phenomena involved and their time and length scales 46

3.1.1 absorption, transmission, reflection of radiation 46

3.1.2 generation, diffusion, recombination and energy relaxation of electron-hole plasma 47

3.1.3 Temperature, pressure and phase fields 48

3.2 The model 48

3.2.1 Energy transfer to matter 51

3.2.2 Energy balance and equation of motion 53

3.2.3 Physical parameters 55

3.2.4 Equations of state and thermodynamic functions 57

3.3 Numerical implementation 60

3.4 Results of calculations 64

3.5 Comparison with experiments 68

4 Pre-bonding silicon-diamond elastic contact 71

4.1 Experimental diamond and silicon profiles 74

4.2 Contact mechanics at high pressure 75

4.3 Contact mechanics of the diamond and silicon samples 81

4.4 Measurement of the local pressure 83

II Ion implantation in diamond for monolithic photonic devices 89

5 Why diamond as a photonic devices substrate 91

5.1 Quantum information and quantum computation 92

5.1.1 Quantum Fourier Transform 94

5.1.2 Phase estimation 96

5.1.3 Order-finding and factoring 97

5.1.4 Universal quantum gates 98
5.2 Physical implementation of quantum gates 99
5.3 Diamond and quantum computation 102

6 Optical properties of proton damaged diamond 107
6.1 Experimental 109
6.1.1 Samples 109
6.1.2 Ion implantation 109
6.1.3 Optical characterization 111
6.2 Data analysis 113
6.2.1 Dependence on fluence of the OPD and the ALD 113
6.2.2 Simulation of the ion damage 114
6.2.3 Phenomenological model 115
6.2.4 Multi-layer model and validation of the phenomenological model 117
6.3 Discussion and Conclusions 118

7 Ion-beam writing of waveguides in diamond 121
7.0.1 Experimentals: implantation and measurements 122
7.1 Intepretation of the phase maps 123
7.1.1 Finite element modeling of the waveguides 125
7.1.2 Fitting of the experimental maps 126
7.1.3 Conclusions 127

A Persson's theory of contact mechanics and applications 129

B Additional proofs to chapter 6 137
B.1 Swelling and optical path difference 137
B.2 Fluence calculation 139

Preface

The research on the possible applications of Chemical Vapor Deposited (CVD) Diamond became very popular in the 80s of the last century, when the progress in the CVD technique of diamond growth seemed to fulfill the requirements necessary to allow an industrial scale-up. At that time diamond high power high frequency electronics was believed to be within reach in a few years. Even 3D stacked electronics was foreseen in the short term. Other appealing applications exploiting the extreme properties of diamond were envisaged, as thermal infrared windows, synthetic diamond dosimeters, diamond coatings for medical tools, diamond trackers in high energy physics experiments, UV solar blind diamond detectors sensors for space applications. After some decades some of these expectations were found to be too optimistic.

A true development of diamond electronics is heavily hampered by the fact that no viable n-doping has been achieved so far, whilst boron doping makes diamond a p-type semiconducting material, nonetheless the acceptor levels are as deep as 0.37 eV from the valence band. Other drawbacks to the applications of this outstanding material are:

- the polycrystalline nature of CVD diamond and, as a a consequence, the defects related to grain boundaries;
- the single-crystal CVD diamond can be grown homoepitaxially on diamond substrates with excellent quality, but it is limited to an area the order of 1 square centimeter;
- the cost of the material remains high, unless until the use of this material becomes so widespread to allow for mass production, and the reproducibility of the final product of the CVD growth is still an issue.

At present it seems clear that:

- diamond-based electronic devices will require a long term research effort;

- radiation tolerant, high speed, radiation sensors are still an appealing solution in future high energy experiments and space experiments;
- biological devices, taking advantages of the superior biocompatibility of diamond and of its very favourable electrochemical properties is the most viable and interesting application of CVD diamond in the short term.
- several luminescent centers in diamond have been identified to be of great potential in integrated photonics.

All the items listed above but the first are dealt with by my Ph. D. work.

The first part of this dissertation is dedicated to the study of a silicon-on-diamond bonding technology which was invented and developed in my research group during the last three years. The Silicon-on-Diamond (SOD) material that we developed promises to be a stepping stone to the integration of silicon electronics and diamond devices operating in various fields as bio-sensing and particle detection. In the second part, in the framework of the possible monolithical integration of photonic devices in diamond, I present a work on the modification of the optical characteristics of diamond by means of ion implantation and on the integration of waveguiding structures in bulk diamond, to which I collaborated with several italian research groups during my Ph.D course.

In spite of the highly-applicative character of this works, my contribution was mainly theoretical. The optimization of the Silicon-on-Diamond bonding, based on a pulsed laser technique, required the study and the modelization of the physical processes involved, which represent the main, although not the exclusive, part of my work. On the other hand, the interpretation of the optical data obtained from the ion-implantation of diamond was conditioned by a sub-lying modelistic effort which represented my principal contribute to the research programme of the modifications of optical characteristics of diamond by ion implantation.

Part I

Silicon On Diamond laser bonding

Chapter 1

Why bonding silicon to diamond and how

1.1 Motivations of the research on the subject

Mono-crystalline silicon and diamond, the cubic crystalline forms of silicon and carbon, underwent different developments both in research and industry. High-efficiency purification techniques and crystallization methods allow to obtain, in form of silicon ingots, the biggest and most defect-free mono-crystals at a moderate cost. At the same time, the development of scalable electronic integration techniques on large-area silicon wafers has determined a 50-years enduring exponential growth of the microelectronic technology in terms of performance. Progresses in Chemical Vapor Deposition (CVD) of synthetic diamond has been, in comparison, much slower and problematic. The mono-crystals available at present on the market are limited in size to the square centimeter area and to the millimeter thickness, with a relatively high cost, and in spite of their very good chemical purity, they often present structural defect densities (mainly dislocations) not comparable with the standard electronic-grade silicon wafer. Moreover, even if the availability of diamond as a new wide band-gap, low dielectric constant semiconductor of IV group seemed to open the way, at the beginning of the 1980s, to important progresses especially in power electronics, the actual applications of diamond in research and industry has remained limited to some niche sectors, discouraging the investments and slowing down progresses in the production techniques. Nevertheless, the exceptional characteristics of diamond, which, in principle, could make it a decisive tool for current issues in several research fields, justify the efforts made until now to avoid the obstacles to its wider employment. In this context, the development of a composite material which combines the versatility of silicon as base material for electronic in-

tegration and the extreme characteristics of diamond, as heat spreader, radiation detector, or bio-sensor, remains a prominent interest for the scientific community. Here I report on some of the motivations for the research on the subject of Silicon-on-Diamond (SOD) bonding, moving from the traditional thermal application of diamond to more recent and challenging issues.

1.1.1 Silicon-On-Diamond as heat spreader

The exponential growth in integration capability of silicon industry is believed to be about to reach, in the next decade, the limits imposed by the physics. These are determined not only by the atomic dimensions [1] but, quite before it, by the dissipation capability [2] both of the silicon substrate and (much more) of the SiO_2 layers which insulate the electronics from the substrate in Silicon-On-Insulator (SOI) structures. The SOI concept is at present the commonly adopted solution to the latch-up problems limiting the velocity of the last-generations of digital processing chips [3] , but the thermal budget weighs upon further increases in integration capacity of this devices. Since diamond yields extreme performances both as electric insulator and as heat spreader (see Tab. 1.1.I), and possesses also the advantage of a relatively low dielectric constant, it has been only natural to suggest that diamond could be the ideal substrate in a SOI structure joining together high thermal dissipation capability (i.e.: high integration capacity) and high operational speed [4, 5, 6, 7] . Moreover, the advantage of the employment of diamond could remain very strong also with a very poor-quality nanocrystalline material, being its thermal conductivity, and, much more, thermal diffusivity (the principal figure of merit during transients) at least three times higher than that of silicon or copper, letting alone the SiO_2 employed in SOI devices whose thermal performance is three orders of magnitude worse.

1.1.2 Silicon-On-Diamond as radiation detector

As a radiation detector, diamond has a number of interesting characteristics (see Tab. 1.1.II for this and other data relative to diamond in comparison to silicon). Low dielectric constant and high saturation velocity of the charge carriers determine very fast response times. High electrical resistivity enhances the signal to noise ratio, largely compensating the disadvantage of a smaller number of electron-hole couples generated per unit energy, with respect to silicon. Blindness to visible light, due to one of the highest band-gaps (5.5 eV) among semiconductors, makes diamond interesting in space physics [11]. Being an allotrope of carbon, diamond is nearly tissue-equivalent for radiation absorption (equivalent atomic number is 7.2 for soft tissue, compared with 6 for diamond and 14 for silicon), and the calibration

Table 1.1: Thermal conductivity and diffusivity of some types of mono and poly-crystalline diamond, in comparison with silicon, SiO_2 and Copper.

	Thermal conductivity ($Wcm^{-1}K^{-1}$)	Thermal diffusivity (cm^2s^{-1})
Diamond mono-crystal	20	11
Poly-crystalline [8] diamond wafer	$\perp$ to the wafer: ≈ 20 $\parallel$ to the wafer: ≈ 18	$\perp$ to the wafer: ≈ 11 $\parallel$ to the wafer: ≈ 10
Poly-crystalline diamond [8] wafer (isotopically enriched)	$\parallel$ to the wafer: ≈ 35	≈ 20
Nano-crystalline diamond film [9]	$5\div 14$	$3\div 7$
Silicon	1.49	0.9
SiO_2 thin films [10]	$0.005\div 0.015$	$0.003\div 0.009$
Copper	4	1.2

of a diamond device is less problematic than for other semiconductors, making it a promising material in clinical dosimetry [12] . But the most interesting characteristic of diamond as detector, the one which drew the attention of the high energy physics community from the very beginning of the CVD fabrication technology, is its radiation tolerance, i.e., the possibility to remain operative after high radiation fluences with no significant increase of leakage current, no need of increasing the polarization bias or lowering the operating temperature, which for diamond can equal or exceed room temperature. Looking forward to the next hadronic colliders (SLHC) and to their high beam luminosity and necessity of increased radiation tolerance of the inner trackers, several R & D activities are ongoing [13, 14, 15]. Solutions to increase the resistance of silicon are under study, but also the diamond option has arisen an increasing interest (see [16] and relating references). For all these applications, the development of high resolution diamond pixel sensors should require suitable architectural solutions for the electrical connections to the read-out electronics. The common hybrid flip-chip technique, employed for instance in the inner trackers of LHC, could be a viable solution. Nevertheless, a monolithic silicon-on-diamond device, with the read-out electronics integrated on the silicon-side and the detectors fabricated on the diamond side, could be much more convenient with regard both to fabrication costs and to set-up reliability (at the moment, flip-chip technology presents a very high failure ratio).

1.1.3 Silicon-On-Diamond as bio-electrode

The electrochemical properties of diamond and its bio-compatibility[17] make this material of absolute interest as an electrode for measuring and evoking extracellular,

Table 1.2: Comparison between relevant properties of diamond, silicon carbide (4H allotrope) and silicon, as radiation detectors

Property	Diamond	4HSiC	Si
Bandgap (eV)	5.5	3.3	1.12
Breackdown field (Vcm^{-1})	10^7	4×10^6	3×10^5
Resistivity (Ω cm)	$> 10^{11}$	10^{11}	2.3×10^5
Electron mobility ($cm^2V^{-1}s^{-1}$)	1800	800	1350
Hole moblility	1200	115	480
Saturation velocity (kms^{-1})	220	200	82
Relative dielectric constant	5.7	9.7	11.9
Displacement energy (eV)	50	25	13÷20
Enenergy per e-h pair (eV)	13	8.4	3.6
Radiation length (cm)	12.2	8.7	9.4
Average signal per 100 μm (e)	3600	5100	8900

electro-physiologic activity for both in-vivo and in-vitro applications. Although for these applications the most typical probe materials are at present the noble metals and some nano structured materials such as TiN and black-Pt, interest rose recently in the unique interface properties between a diamond electrode and the electrolyte, superior to any other material used nowadays[18, 19]. Semiconducting boron-doped diamond possess a large potential window between the oxygen and hydrogen peaks [20] . This results in a wider range of applied potential between diamond and electrolyte, which does not result in redox reactions and allows the application of stimuli to neurons in a more effective and non-toxic way. Other appealing characteristics of diamond are the low background current during electrochemical measurements, due to its adsorption inertia, the low interface capacitance with aqueous solutions and the independence from pH. Moreover, a p-type conduction, which can be obtained in bulk diamond by B-doping both during growth and by post-growth ion implantation, is not the only way to obtain conductive paths in diamond. Surface p-type conductivity can also be achieved, in humid environment, by hydrogen termination of the diamond surface, being also possible to modulate it down to the micro [21] and nano-scale [22] . Conductive graphite channels can be fabricated in bulk diamond both by laser graphitization [23] and by heavy ion-damaging followed by thermal annealing [24] . If we also consider the possibility of diamond surface functionalization for cells adhesion by a suitable termination of superficial carbon bonds [25], we can explain the strong interest manifested in the last years for diamond in living cells sensing and stimulation (e.g. in neuro-prosthetics). Also in this field, Silicon-On-Diamond technology can play a major role especially in applications where it is advisable, both regarding to band-passing and to electrical noise reduction, to process part of the signal-information as close as possible to the

electrodes. A Reliable SOD technique can be, in this context, an ideal approach to implement biosensors with integrated micro-electrodes on the diamond side and the electronics on the silicon side.

1.2 Methods for Silicon-on-Diamond fabrication

Several techniques have been employed, until now, in the search for a reliable procedure to bond together silicon and diamond in a way to obtain interfaces with suitable mechanical, thermal and electrical characteristics. Some of them did not lead to industrial implementation of the Silicon-on-Diamond concept due to unavoidable drawbacks of the fabrication methods, detrimental of the material quality, others seems to be more promising but, till now, have not gone beyond the R& D stage. In the next paragraphs I refer about the two main techniques employed in Silicon-On-Diamond fabrication, emphasizing their advantages and disadvantages with regards to material quality, easiness of employment and versatility. My research group has invented and developed a fourth method which promises to join together many of the advantages of the formers, avoiding most of the drawbacks, the next chapter will be dedicated to its exposition.

1.2.1 Diamond growth on silicon substrates

Silicon is one of the first and, till now, most widely employed substrates for CVD polycrystalline diamond growth, so that diamond growth on silicon substrates has been the first natural option for SOD fabrication. The growth process, generally, begins with the formation of a silicon carbide layer [26] , upon which randomly dispersed nucleation seeds grow and coalesce determining the formation of a columnar-arranged polycrystalline matrix. Due to the difference in growth speed of the various crystalline plains, some grains grow faster than others, determining competition and selection of the grain orientations in the first stages of the film growth. In order to determine the electrical, mechanical and thermal properties of the silicon-diamond interface and of the diamond bulk, several factors are under control of the growers. Tribologic treatments with diamond-powders can enhance nucleation density, with advantages for mechanical adhesion and thermal conduction of the SOD interface, but high nucleation density means also high grain-boundary concentration, which is detrimental of the electrical characteristics of the bulk diamond material. Bias-Enhanced nucleation [27] , on the other hand, prevents SiC formation and permits to exploit the almost-rational ratio of diamond and silicon lattice constants (2/3) for etero-epitaxial growth of diamond on silicon. Also in this case, though, the not perfect matching of silicon and diamond crystalline constants does not result in a

monocrystal growth, but at most in a highly oriented polycrystalline material, thus not avoiding the presence of a high density of grain boundaries.

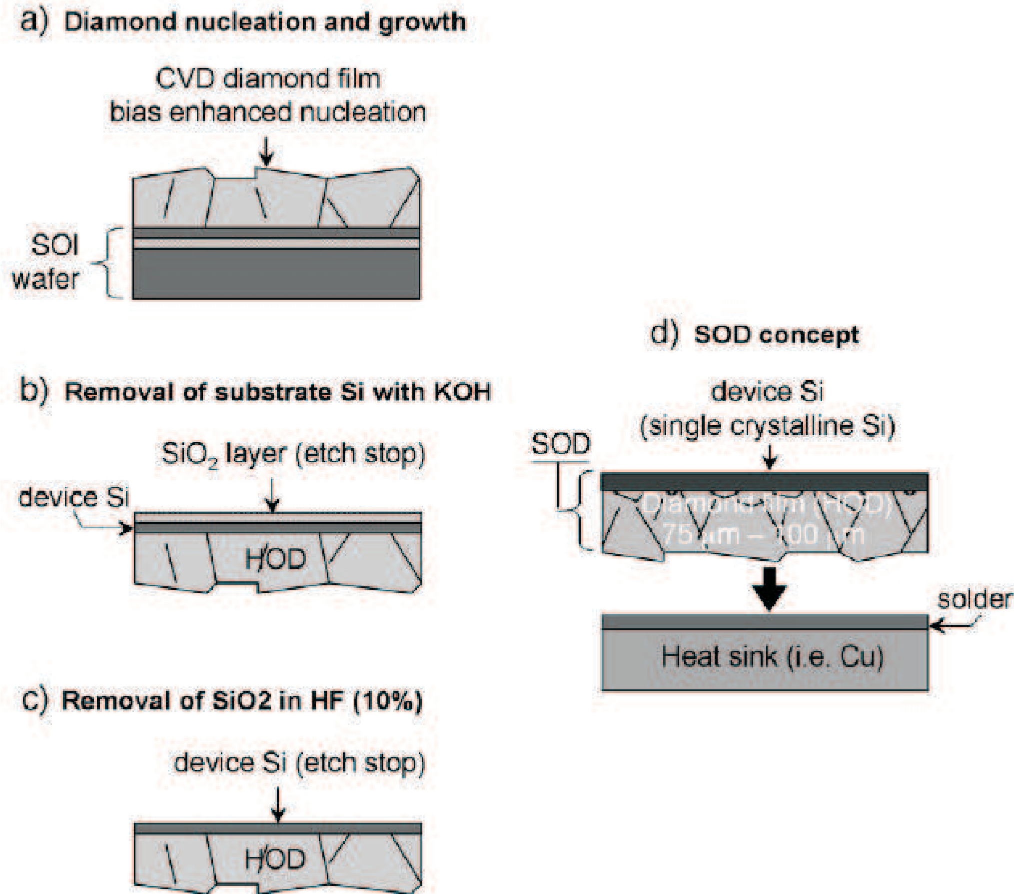

Figure 1.1: fabrication steps of a Silicon-On-Diamond wafer by CVD poly-crystalline diamond on a SOI wafer[28]

Silicon-on-Diamond wafers suitable for electronic integration have been fabricated [28, 4] growing highly oriented diamond on a SOI structure, removing afterwards the silicon substrate in potassium hydroxide (KOH), then the SiO2 layer in fluoric acid (HF) leaving a 1.5 μm thick layer of silicon on top of the 75-100 μm thick diamond film (see 1.1). The authors soldered the rough diamond surface to a copper heat sink to perform thermal conductivity measurements across the diamond layer, without needing any smoothing of the growth side of diamond, but in order to substitute a diamond film for the SiO_2 Buried Oxide (BOX) layer in a SOI structure, the problem of planarization of the poly-crystal diamond layer and of its bonding to a silicon handler have to be faced. Recently, a new planarization process has been developed [29] based on the covering of the diamond surface with a

relatively thick Oxide layer and its conventional chemical-mechanical planarization (CMP). This process is followed by a reactive ion etching (RIE) performed on the surface, adjusting the SF_6/O_2 ratio, in a way to accomplish a same etch rate for oxide and diamond (see Fig.1.2). The roughness of the obtained surface is greatly

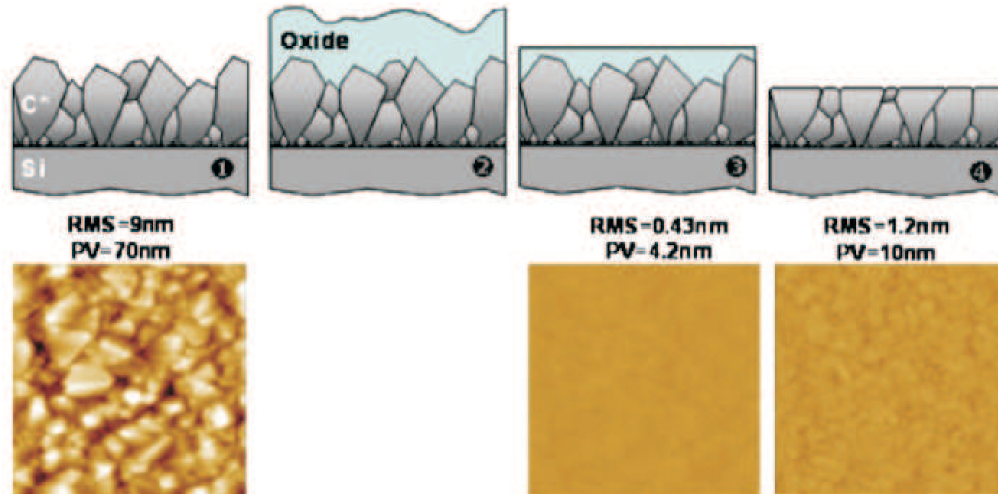

Figure 1.2: Schematic view of the diamond planarization process[29] and AFM scans made on a 200 nm C* surface for the as-deposited C* layer (RMS = 9 nm, PV = 70 nm), after the oxide planarization step (RMS = 0.43 nm, PV = 4.2 nm), and after the total process (RMS = 1.2 nm, PV = 10 nm).

decreased (down to 1.2 nm) but doesnt reach the level of 0.5 nm required for direct bonding of diamond to a silicon handler. In order to overcome this problem, Widiez et al. deposited a polysilicon layer on the polished diamond, smoothed it with a CMP technique and finally used a hydrophilic wafer bonding technique to bond poly-silicon to the handler (see Fig.1.3). The measurements performed by Aleksov et al. on their Silicon-On-(highly oriented)Diamond to assess the thermal diffusive properties of the diamond layer grown on the silicon one, were made by comparison of the temperatures of identically build heaters (see Fig.1.4) on top of the SOD and of the SOI structure, respectively. Measurements show remarkable improvement of the thermal properties, confirming the potential of diamond (also of the poorest crystalline quality) for thermal application. The main drawback of the diamond-on-silicon growth techniques is the inherent very poor electrical quality of most of the polycrystalline material including the highly oriented diamond material obtainable by epitaxial growth. This prevents applications aimed to exploit the characteristics of diamond as radiation detector. For instance, measurements with a UV pixel sensor obtained by deposition of micro-crystalline diamond on top of the silicon read-out electronics evidenced very poor performances [30] , most likely

arising just from the very high structural defect density of diamond. It is worth

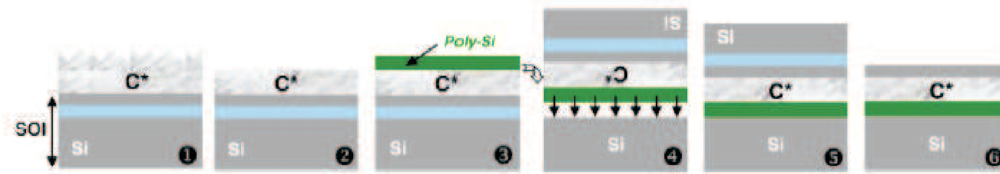

Figure 1.3: Process description of the SOD substrates fabricated by technology described in ref.[29]. 1 C* deposition on SOI wafer. 2 C* planarization by the DPE process. 3 PolySi layer deposition. 4, 5 Hydrophilic wafer bonding (polySi——Si) on Si report wafer. 6 Final SOD substrate.

mentioning that also the concept of silicon growth on diamond substrates has been exploited in recent years [31] . Obviously, the poor quality of polycrystaline silicon prevents, for this material, any application in electronic integration.

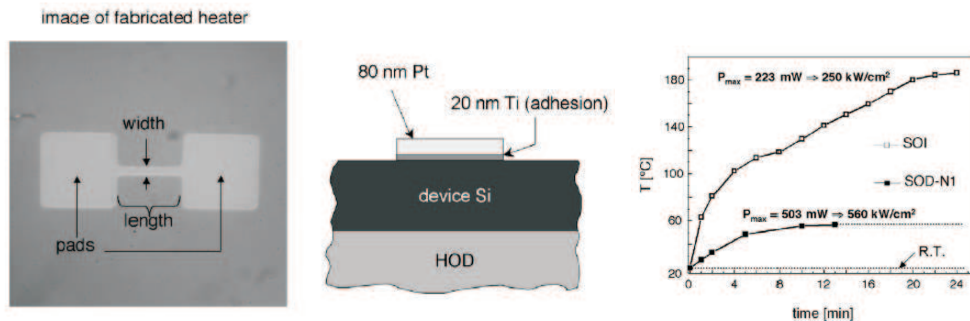

Figure 1.4: Optical micrograph of a fabricated metal strip micro heater (a) and a schematic cross section of the heater on an SOD wafer (b). (c) Results of the R(T) self heating measurements of the micro heaters on SOD and SOI; the applied power density was 250 and 560 kW cm2, Respectively[28].

1.2.2 High temperature and pressure method

Since it is not possible to grow on silicon a diamond material qualified for application as detector, the only alternative for the use of SOD as monolithic radiation sensor could be the bonding of independently obtained silicon and diamond wafers with suitable characteristics. Though conventional bonding methods are somewhere believed to be applicable also to silicon-diamond bonding in the future [29], under the condition of the improvement of the diamond polishing, neither research nor

industrial application of such a technique is reported up to now. As a matter of fact, the only attempt to bond directly silicon and diamond [32, 33] was based on heating a diamond and a silicon sample under uniaxial pressure. The samples were pressed together at about 30 MPa in a ultra-high vacuum chamber, and heated from 850 to 1200C. Contact between samples and heaters were assured by a buffer layer of graphite or borum nitride, to avoid fractures. Heating and cooling was performed in 2 and 5 hours, respectively, and the maximum temperature was maintained for about 15 hours. The quality of the obtained interface was tested by scanning acoustic microscopy (SAM), to verify effective adhesion and possible formation of cracks, and with transmission electron microscopy (TEM), to investigate the nature of the bonding between silicon and diamond. SAM images of the bonded samples (see Fig.1.5) show that the quality of the bonding strictly depends on the processing temperature.

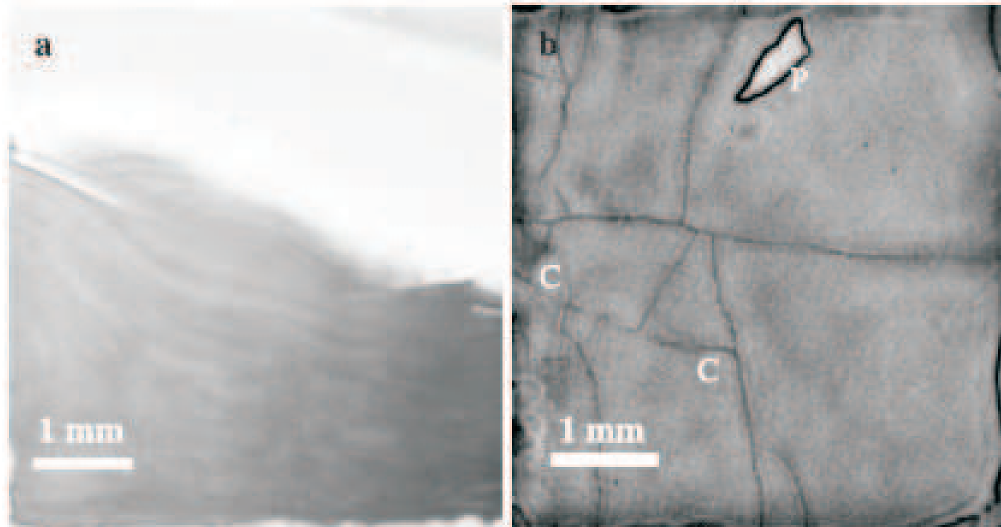

Figure 1.5: SAM images of polished HOD diamond bonded to Si at 850C (a) and 1050C (b). White regions of the sample in image (a) represent unbonded areas; cracks (C) and polishing defects (P) are observed in the image (b)[32, 33].

For temperatures below about 950C large areas of the samples (brighter in the SAM images) remain unbonded (40-60% of the surface at 850C). On the other hand, for temperatures above this limit, complete adhesion is achieved, but diamond presents cracks propagating along the bulk, only at the peripheral region of the sample at lower temperatures, along all the interface at higher ones. This fact can be easily explained by observing that although diamond has a linear expansion coefficient lower than that of silicon at room temperature, an inversion of the two coefficients holds at about 700 K, so that a diamond sample having the same length

of a silicon one at room temperature, will be longer once above about 1300K (See Fig. 1.6). From this temperature on, if adhesion holds, it will result in a tensile force in diamond after cooling. Polycrystalline diamond, as the one employed by Yushin et al., has only a little tensile strength resistance in the direction parallel to the wafer, due to the easiness of crack propagation along grain boundaries so that a failure of the bonding process at the higher temperatures was quite expectable. TEM images of the silicon-diamond interface, in the points where they adhere, shows two different kind of Si-diamond transition: abrupt transition, with a good matching of crystal planes of the two materials, and smooth transition, with an amorphous 20-30nm thick amorphous layer containing oxygen (see Fig. 1.7), probably related to the roughness of the diamond surface (tens of nanometers).

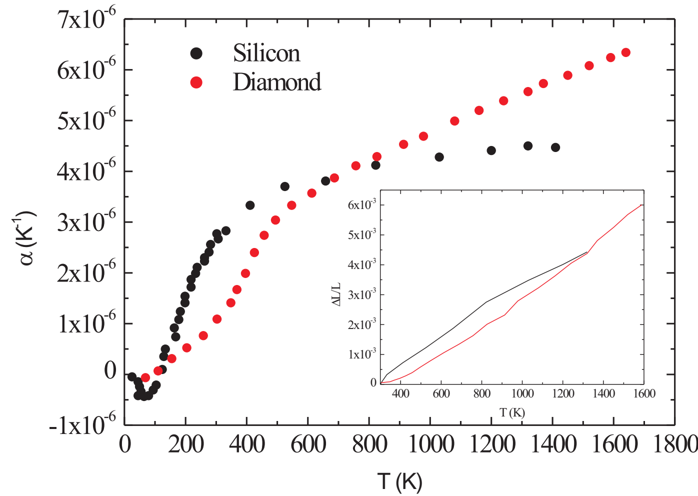

Figure 1.6: Linear expansion coefficients of silicon (black) and diamond (red) from 0 to 1500K [34, 35] . In the inset, the integrals of the linear expansion coefficients of silicon and diamond calculated from 300K to the temperature T, as a function of T. This last plot represents the relative increment in length for two samples having, at room temperature, the same dimensions. It can be seen that at temperatures above 1300K a diamond sample should be longer than the silicon one.

The state of the art of the direct, thermal bonding of silicon on diamond suggests the following conclusions:

- At least at the pressure under consideration of about 30 MPa, the temperature which is necessary for the adhesion determines rupture of the polycrystalline diamond material during cooling. Practical implementation of this method

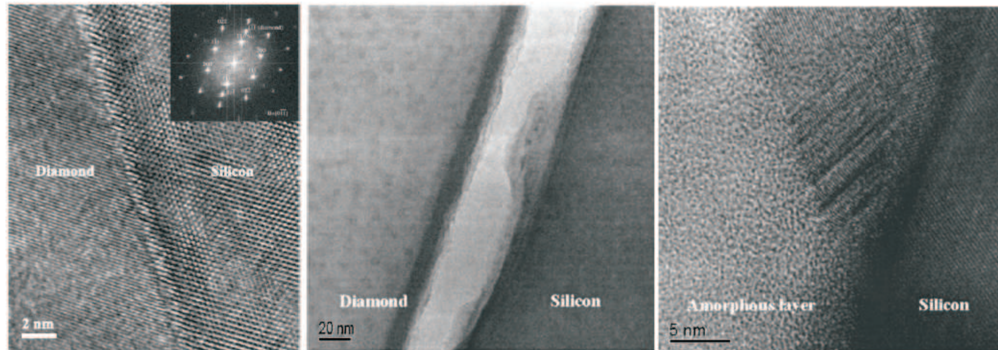

Figure 1.7: (left) TEM image of the abrupt diamond-silicon transition, the inset shows a FFT image of this area. (center) smooth transition, with the interface layer that (right) clearly shows its amorphous nature at higher resolutions[32, 33].

should require, thus, either the use of mono-crystals (desirable, anyway, for many applications), or the use of lower temperatures and higher pressures or both.

- In order to obtain an interface with good properties of thermal conductivity and electrical insulation, an abrupt diamond-silicon transition is probably desirable. To this aim, a better polishing of (especially) the diamond surface is required.

- The temperatures involved with this method, in any case, prevent the possibility of a pre-processing of the silicon electronics: any integration of electronics on the free surface of the silicon wafer has to be performed after the bonding process.

This last point, particularly, is worth of attention. If it could be ever possible to bond diamond not to a bare silicon wafer, but to a conventional integrated chip, without damaging the electronics, this could open the way to exploit the presently available small-sized diamond mono-crystals without the need of developing expensive small scale electronic-integration techniques. Such a room-temperature bonding technique is now disposable, thanks to the efforts of the research group with which I have worked during my Ph.D. program. To the results of our work, with emphasis on my personal contribution to it, is devoted the next chapter.

Chapter 2

Silicon-on-Diamond by pulsed laser irradiation

The concept of Silicon-On-Diamond (SOD) bonding which I worked on during my doctorate program is based on the simple consideration that while diamond is a transparent material from the microwave well into the deep ultraviolet region of the spectrum, down to about 225 nm of wavelength, the penetration length of visible and UV radiation in silicon ranges only from 10 to 1000 nm. That is, if a light pulse of suitable energy and duration passes through a diamond film in close contact with a silicon substrate, it releases all its energy (to the net of the reflection) in a thin interface region, melting silicon and, possibly, a carbon layer, resulting in the adhesion of the two samples. This simple idea has been exploited during a three year experiment of the Italian Institute For Nuclear Physics (INFN) called RAPSODIA (Radiation Active Pixel Silicon On DIAmond) to assess the feasibility of the process and to test the quality of the obtained material in view of future application in monolithic active pixel detectors for particle physics. The members of the collaboration belong to several italian institutions, namely the University and the INFN of Florence, the European Laboratory for Non-Linear Spectroscopy (LENS) of Florence, where all the bonding experiments and the spectroscopic diagnostics of the resulting material were performed, the Institute of Applied Optics (INOA) of Florence, where we studied the morphology of the diamond samples, the University of Perugia and the Institute for Microelectronics and Microsystems (IMM) where silicon devices have been realized and the tests have been performed for the thermal characteristics of the interface. The work is still in progress under a new project called CHIPSODIA (CHIPs by Silicon On DIAmond), whose focus has been enlarged to encompass also biological applications in neuronal interfaces, with the involvement of the Italian Institute of Technology (IIT) of Genova. I participated to the creation of the project since its beginning and collaborated to all the phases of

the experimental activity performed in Florence. Moreover, I have performed theoretical studies for the optimization of the process, whose results will be presented in the next chapters. In this chapter, after an illustration of the bonding apparatus and experiments, results are presented in term of mechanical, structural and thermal analysis of the interface between diamond and silicon in our SOD samples.

2.1 Bonding apparatus and experiments

The simple concept of pulsed laser bonding of Silicon-On-Diamond illustrated in the previous paragraph involves several issues which have to be carefully taken into account. First, which are the most suitable wavelength and pulse duration of the laser source, in order to obtain adhesion (in the first place) and favorable characteristics of the silicon-diamond interface? Which is the most favorable energy density (that is, how much have we to focalize the laser beam) and which is the right number of pulses for each welded point? And last, how close has to be the contact between diamond and silicon before irradiation to be sure that adhesion holds after the treatment? All these questions will be carefully and quantitatively addressed in chapters 4 and 5, which are dedicated to the optimization of the process. Nevertheless, the choice of the laser source and the project of the irradiation chamber had obviously to deal such problems at least in a preliminary, qualitative or semi-quantitative way, in order to have a reasonable probability to obtain some workable results since the first experiments. Thus, I will first expose a semi-quantitative study of the bonding process, then I will describe our set up for the bonding experiments.

2.1.1 Preliminary study

During the irradiation of the silicon-diamond interface two kind of processes occur, namely the release of radiation energy to matter, which occurs in silicon on a scale-length dependent both on the wavelength (shorter for shorter wavelengths) and on thermal diffusion both in silicon and in diamond, at a rate dependent on thermal diffusivity. Since the heat diffusion length is proportional to the square root of the time, at the end of a single light pulse the energy released can be divided into two contributions, the first proportional to the absorption length and to the attained temperature, and the second proportional to the square root of the pulse duration and to the interface temperature itself. Roughly, but effectively, we can write down the relation:

$$E \approx S w_\lambda c_{\mathrm{Si}} T + S c_{\mathrm{Si}} T \sqrt{D_{\mathrm{Si}} \tau} + S c_{\mathrm{Dia}} T \sqrt{D_{\mathrm{Dia}} \tau} \tag{2.1}$$

where E is the energy of the single pulse (to the net of reflections), τ is its duration, S is the cross-sectional area of the laser beam on target, T is the temperature reached

at the end of the pulse, $c_{\mathrm{Si,Dia}}$ is the specific heat for unit volume of the material, w_λ is the penetration length of the radiation (of wavelength λ) and $D_{\mathrm{Si,Dia}}$ is the thermal diffusivity (see Fig. 2.1 for an intuitive illustration). Application of Eq. 2.1

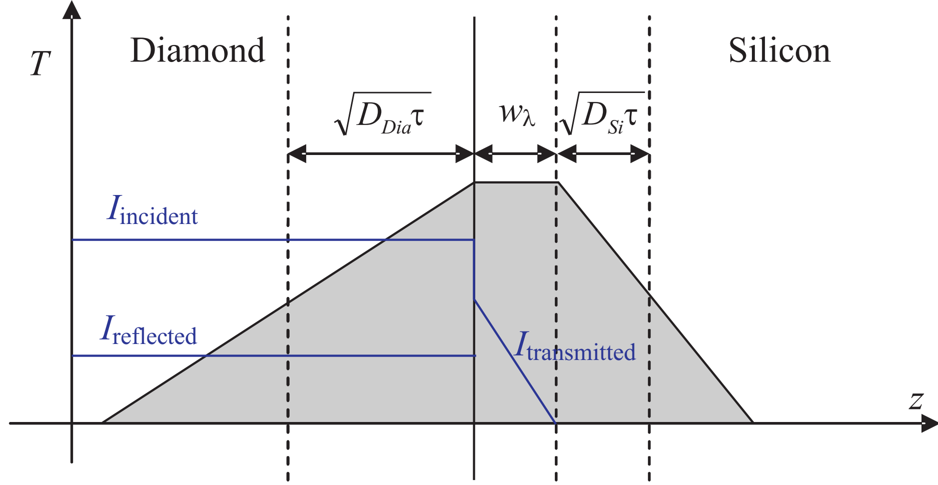

Figure 2.1: Black: approximative temperature profile at the end of the laser pulse. Blue: approximative incident, reflected and transmitted light intensity.

permits to estimate, for a laser source of given wavelength, pulse width and energy, the level of focalization (that is, the cross section S) which is necessary to reach a given temperature T, say, the melting point of silicon. The same relation permits to infer that, in order to reduce the thermal budget in charge of the interface (related with the width of the layer damaged by the process), short pulse durations and absorption lengths are preferable. More difficult is to evaluate the thickness of the damaged layer. An over-estimated limit can be taken as the energy per unit surface divided by the silicon heat of fusion per unit volume:

$$w_{\mathrm{melt.}} = \frac{E}{Sc_f}, \tag{2.2}$$

supposing that all the energy impinging on the sample is dissipated in silicon melting. In this way, we neglect the thermally diffused heat during re-solidification, which is dependent on the time employed by the melting front to reach it maximum extension, and the heat absorbed by diamond during carbon melting, which comes from thermal conduction both from melted silicon and from melted carbon, this latter on its turn absorbing energy from radiation. It is not possible to evaluate these contributions by means a ”rule of thumb” method.

Under these assumptions we can evaluate, by means of Eq. 2.1 and 2.2, the energy density necessary to reach the melting temperature of carbon and the correspondent thickness of the damaged layer. We compare three typical light sources: A

Table 2.1: Comparison between typical operating parameters for three different sources, calculated as in Eqs. 2.1 and 2.2, with c_f = 4180J/cm^3, c_{Si} = 1.64 J/(cm^{3}K),c_{Dia} = 1.78 J/(cm^{3}K), D_{Si} = 0.9 cm^2/s, D_{Dia} = 11.2 cm^2/s and with T which has been taken as 4000 K.

Wavelength (nm)	Penetration length (nm)	Pulse width (s)	Threshold energy (Jcm^{-2})	Energy per pulse (J)	Spot surface (mm^2)	Damaged layer (μm)
280	5	20 n	8.5	1	12	10
355	10	7 n	5.1	0.1	2	6
355	10	20 p	0.28	0.01	3.5	0.34

280 nm radiation from an excimer laser, with 20 ns pulses of 1 J, the third harmonic of a Q-switched NdYAG laser at 355 nm, with 7 ns pulses of 0.1 J, and the same wavelength of a mode locked NdYAG, with 20 ps pulses of 0.01 J. All the energies have been multiplied by a factor about 2 to take into account the reflectivity of a diamond-liquid silicon interface. Results are shown in table 2.1, where, on the basis of the energy density the surface of the spot is evaluated. In all the calculations, the room temperature parameters were adopted. It can be seen that the energy density required for the carbon fusion in the picosecond range is of the order of tenths of J/cm^2, while the nanosecond range requires one or more J/cm^2, with a damaged layer one order of magnitude thicker. Since we are interested to applications of SOD in the field of micro-electronics integration, with desirable interface thicknesses of tens of nanometers or less, we avoided form the start to choose a more widely available and less expensive nanosecond pulsed laser and moved toward the choice of a mode locked laser source.

Because the thicknesses involved in the bonding process have to be of the order of one hundred nanometers or less, it is natural to require that, in order to obtain adhesion, most of the two silicon and diamond surfaces have to be in close contact during the irradiation. This can be achieved in two ways: either polishing the two surfaces down to a sub-nanometric scale, or pressing them together with a sufficient uni-axial pressure. Very well polished, detector-grade mono-crystals are now available on the market at quite a high cost (order of 1k$ per typically 5×5mm^2 samples), but we programmed to define the process with bonding tests performed on polycrystals whose price is one order of magnitude lower, with a roughness of the order of tens of nanometers and a peak to peak horizontal distance of order tens of micrometers. Thus, we had to evaluate, in the first place, the order of magnitude of the pressure which deforms the silicon lattice (whose elastic constants are 5-10 times lower than that of diamond) in a way to obtain a contact as close as possible. A full-quantitative theoretical treatment of the problem will be given in chapter 4, but at the beginning I started with a simple dimensional consideration, exploited also in

ref.[36] for the study of the contact between rubber and a hard, rough surface: the only physical quantities intervening in the phenomenon, under the assumption that the silicon thickness is much greater than the mean peak-peak horizontal distance l, are the roughness h, l itself, and the bulk modulus J, and the simplest consistent way to obtain a pressure with this three quantities is to pose:

$$P \approx J\frac{h}{l}. \tag{2.3}$$

We will see later that Eq. 2.3, in its simplicity, catch the essence of the physics involved. Equation 2.3 tells us two important things: first, roughness, intended as the rms value of the deepness of the asperities on the diamond surface, is not the only scale involved in the problem. That is, a waved surface with a long distance between peaks can perform better than a well polished one but with a higher depth over width aspect ratio. Secondly, sicne the silicon bulk modulus is about 100 GPa, about 100 MPa are required with our present samples to obtain a good pre-bonding adhesion. This value has been our reference for the project of the bonding chamber described in the next paragraph

2.1.2 Experimental set-up

The project of a steel chamber for the compression and the irradiation of the silicon-diamond interface had to satisfy these requirements:

- To press together samples of 5×5 mm^2 at a pressure of about 100 MPa in a reproducible way.
- To ensure transmission of a 355 nm light pulse on the whole surface of the sample.
- In order to avoid oxygen and other contaminations, it has to be possible to keep the samples in inert atmosphere during irradiation.

To these aims, we realized the chamber whose scheme is shown in figure 2.2. The light penetrates in a 8 mm-diameter hole through a 1.5 cm thick, 2 cm wide fused silica window (a in Fig.2.2), onto which the samples (b) are pressed by a piston (c) pushed by a screw (f) and a spring (e). The samples are adjusted in a central position by means of a shaped ring (g). The silicon surface, when necessary, has been protected against damage due to compression by a 3 μm thick graphite buffer. The spring is coupled to the piston by a sphere (d) in order not to communicate to the piston any rotational motion with associated shear solicitation. The maximum force exerted by the spring is 200 kgp, with a compression of 15 mm length.

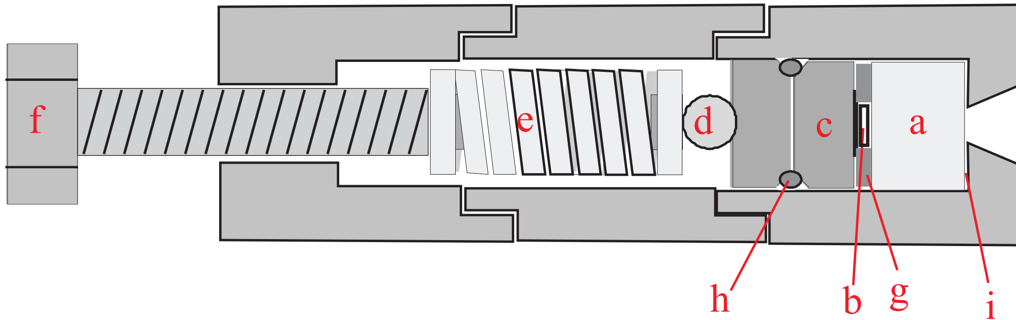

Figure 2.2: Scheme of the irradiation chamber. Letters are referred to in the text.

In order to avoid oxygen contamination the chamber has been mounted in argon atmosphere. While a Viton O-ring (h) seals the space between the piston and the cylinder, an aluminum ring (i) covered by a thin layer of vacuum grease is interposed between the fused silica window and the back of the cylinder. The mounting of the samples requires a special care to the cleaning of the two plates, which are cleaned in ultrasonic bath with solvents, rinsed in deionized water and finally blowed with dry nitrogen. Since one of the two diamond surfaces, the growth side one, can be possibly much better than the other in term of roughness, both the sides are previolusly tested by a white-light Vygo profilometer, in order to press the silicon plate onto the smoother diamond surface. The polishing is easily tested observing the fringes created by the interference of the light reflected by the diamond and the silicon surfaces in reciprocal contact: with a good cleaning they disappear also with a relatively small pressure.

The main laser source used in our bonding experiments was an EKSPLA PL2143 Nd:YAG mode-locked laser, operating at the 1064 nm wavelength of the fundamental mode, with a set of non-linear crystals offering the possibility to operate in the second harmonic at 532 nm or at the frequency mixing of the fundamental and the second harmonic at 355 nm wavelength. The pulse duration is 20 ps, repetition rate is 10 Hz, and the single pulse energy at 355 nm ranges up to about 16 mJ (optimal 10 mJ). The 355 nm harmonic of another Nd:YAG mode-locked laser of about 60 ps pulse width, 15 mJ per pulse, was occasionally employed, as well as the same harmonic of a Q-switched laser operating at 7 ns pulse width and about 100 mJ energy per pulse.

An image of the second harmonic laser beam of the EKSPLA PL2143 laser, at 532 nm, has been taken with a Thorlabs DCx camera, and it is shown in Fig. 2.3.

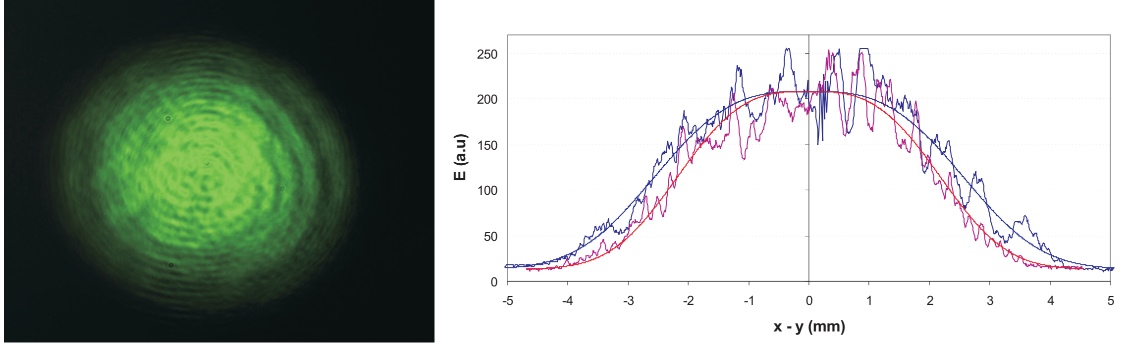

Figure 2.3: (a) Image of the 532 nm 2nd harmonic laser beam. (b,c) Intensity distribution along the x and y direction (blue and magenta, respectively), along with the best fit in term of Eq.2.4

For a given overall energy per pulse E_0 of the laser beam, and a reduction factor ρ of the optics, we can evalutate the highest energy density per unit surface $\mathscr{E}_M$ and the minimum one $\mathscr{E}_m(A)$ which we could obtain irradiating the surface with a square matrix of spots with a pitch R. The profile represented in Fig.2.3 is well described, to the net of the diffraction profile, by a quasi-Gaussian distribution of kind:

$$\mathscr{E}\left(x,y\right)=\frac{E_0}{2\pi\rho^2\sigma_x\sigma_y\int_0^\infty e^{-z^\alpha}dz}e^{-\left(\frac{x^2}{2\rho^2\sigma_x^2}+\frac{y^2}{2\rho^2\sigma_y^2}\right)^\alpha}, \tag{2.4}$$

with $\sigma_x = 2.3$ mm, $\sigma_y = 2.0$ mm, $\alpha = 1.51$ and $\int_0^\infty e^{-z^\alpha}dz = 0.902$ (with the errors smaller than the less significant figures). Taking into account Eq.2.4 we have straightforwardly:

$$\mathscr{E}_M=\frac{E_0}{2\pi\rho^2\sigma_x\sigma_y\int_0^\infty e^{-z^\alpha}dz} \quad \text{and} \quad \mathscr{E}_m=\mathscr{E}_M e^{-\left[R^2\left(\frac{1}{8\rho^2\sigma_x^2}+\frac{1}{8\rho^2\sigma_y^2}\right)\right]^\alpha} \tag{2.5}$$

The beam has been focused on the diamond-silicon interface by means of a 1” diameter fused silica lens with a 50 mm focal length, in a way to control the spot size. If f is the focal length of the lens, s the thickness and n the refraction index of the fused silica window, the distance x between the optical center of the lens (in the thin lens approximation) and the window surface in order to obtain a reduction

factor ρ is simply:

$$x = (1 - \rho)\, f - \frac{s}{n}. \tag{2.6}$$

Each bonded point has been exposed to 1 to 50 pulses in our bonding experiments, and the whole surface of the sample has been exposed to the laser light by translation of the irradiation chamber in the xy plane by means of a micrometric setup.

The maximum and the minimum irradiance can be calculated by Eqs. 2.4. As a typical example, the energy density per pulse on the irradiated surface, assuming $E_0 = 10$ mJ, $\rho = 1/6$ and $R = 0.75$ mm, ranges in the interval $\mathscr{E}_m = 0.44$ Jcm^{-2} $\div$ $\mathscr{E}_0 = 1.3$ Jcm^{-2}.

2.1.3 Samples and bonding experiments

We performed our bonding experiments exploiting standard $5 \times 5 \times 0.3$ mm^3, highly resistive silicon dies and $5{\times}5{\times}0.5$ mm^3 poly-crystalline detector-grade diamond films produced by Element Six$_{\mathrm{TM}}$. Three different batches of diamond were exploited, exhibiting decreasing roughness (Ra) from about 6 to less than 2 nm. A deeper insight in the surface properties and in their influence on the bonding process will be given in chapter 4. Bonding experiments were performed with the set-up described in the previous paragraph, varying several parameters under our control, namely:

- Reduction factor ρ of the optics, which ranged mainly between 0.13 and 0.17, with a single experiment at ρ=1.
- Pulse energy, with values between 10 and 16 mJ per pulse.
- Number of pulses, between 1 and 50.
- Pulse width: one experiment has been performed with a Q-switched Nd:Yag laser with 7 ns pulse duration and about 100 mJ pulse energy.

In all the experiments the 355 nm wavelength was exploited, and the uni-axial pressure imposed was the maximum exerted by the spring: 200 kgp/0.25cm^2, that is about 80 MPa. In Tab. 2.2 a survey of the bondings performed is given, with indication of the process parameters and of the diagnostics exploited in the interface characterization.

2.2 Functional tests

Whichever application Silicon-On-Diamond is designed for, the interface between the two materials has to fit certain demands: mechanical resistance is crucial in every

Table 2.2: Table of the bonding experiments with indication of the process parameters and of the performed diagnostics.

Sample	Batches Silicon Diamond	Shot matrix red. factor interdistance	Pulse energy duration number	Diagnostics
SOD 1	$< 100 > 300\mu$m Batch 2007	3×3 0.17 1 mm	16 mJ 20 ps 50	RAMAN FTIR
SOD 2	$< 100 > 300\mu$m Batch 2007	3×3 0.17 1 mm	16 mJ 20 ps 20	FTIR shear test
SOD 3	$< 100 > 300\mu$m Batch 2007	5×5 0.23 1 mm	16 mJ 20 ps 10	RAMAN FTIR
Unnamed	$< 100 > 300\mu$m Batch 2007	5×5 0.23 1 mm	16 mJ 20 ps 1	not adherent
SOD 4	$< 100 > 300\mu$m Batch 2007	5×5 0.23 1 mm	16 mJ 20 ps 10	only one point adherent
SOD 5	$< 100 > 300\mu$m Batch 2007	5×5 0.23 1 mm	16 mJ 20 ps 10	RAMAN tens. str. test
SOD 6	$< 100 > 300\mu$m Batch 2007	5×5 0.23 1 mm	16 mJ 20 ps 10	RAMAN, FTIR section & SEM heated 400C
SOD 7	$< 100 > 50\mu$m Batch 2007	7×7 0.23 1 mm	16 mJ 20 ps 10	Tensile strenght test
SOD 8	$< 100 > 50\mu$m Batch 2007	7×7 0.17 0.75 mm	10 mJ 20 ps 20	thermal conductivity STEM, TEM
SOD 9	$< 100 > 300\mu$m Batch 2007	7×7 0.17 0.75 mm	100 mJ 7 ns 10	RAMAN
SOD 10	$< 100 > 300\mu$m Batch 2007	2×2 width 1mm 3 mm	$5 \div 10$ mJ 20 ps $2 \div 10$	(with. diffuser)
SOD 11	$< 100 > 50\mu$m Batch 2007	7×7 0.17 (nom.) 0.75 mm	10 mJ 20 ps 10	thermal conductivity STEM, TEM
SOD 12	$< 100 > 50\mu$m Batch 2007	7×7 0.13 0.75 mm	10 mJ 20 ps 5	thermal conductivity STEM

SOD 13	$< 100 >$ 480μm Batch 2007	10×10 0.14 0.5 mm	10 mJ 20 ps 5	electrical measurements
SOD 14	$< 100 >$ 480μm Batch 2009	10×10 0.22 0.5 mm	10 mJ 20 ps 5	electrical measurements
SOD 15	$< 100 >$ 300μm Batch 2010	3×3 0.06-0.33 1 mm	3.3-10 mJ 20 ps 10	

post-bonding processing, thermal shock safeness should be a must if current photolithographic processes have to be performed on the silicon side after bonding, good thermal conductance properties is obviously mandatory for silicon-on-"diamond as thermal spreader". In this section the functional characterizations performed on our SOD samples are described in some detail.

2.2.1 Tensile strength tests

Mechanical strength of the bonding between the two silicon and diamond dies is important in a double respect: first, it is an index of closeness of the physical contact between the two materials, hopefully both from thermal and electrical point of view. Secondly, for any post-bonding mechanical processing as polishing and planarization the need for a resistant interface is prominent. We performed tensile strength tests

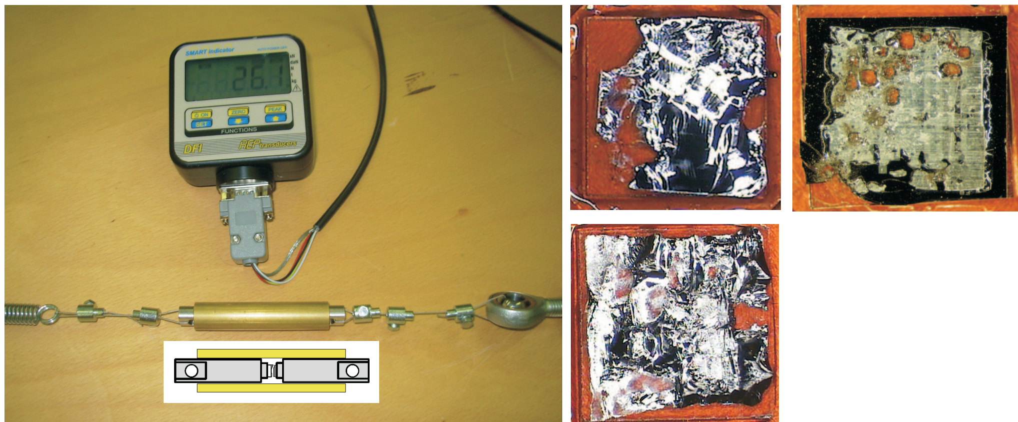

Figure 2.4: (left) Tensile strength test set-up along with the scheme of the two cylindrical holders running inside the gauged hollow cylinder. (right) The two samples SOD 5 (up-left), SOD 7 (up-right) and SOD 14 (down) after detachment, photographed by the silicon side.

on the samples SOD 5, SOD 7 and SOD 14, with a home-made setup whose *core* is shown in Fig.2.4. Two steel cylindrical holders, running inside a gauged hollow cylinder to assure axial coincidence, are fixed to the opposite sides of the bonded sample with an epoxidic resin. The two holders are drawn by means of a spring and a screw, in order to dose the strain stress, which is measured by means of a load cell. The samples were found resistant to strain stress up to 13 kgp (SOD 5), 29 kgp (SOD 7) and 60 kgp (SOD 14). Taking into account the spot diameter (which is about the beam diameter of 6 mm times the reduction factor of the optics) we found that the maximum specific strain stress tolerated by the interface was about 5, 12 and 24 MPa, respectively. The rupture behavior was quite different for the three samples: SOD 5 and SOD 14, (300 μm silicon thickness) were broken mainly inside the silicon bulk, apparently for crack propagation from the silicon surface; SOD 7 (50 μm silicon thickness) was detached by the holder mainly for failure of the epoxidic resin, with only a limited amount of the silicon sample being damaged (see Fig. 2.4).

2.2.2 Thermal conductivity tests

In order to test the thermal conductivity of the silicon-diamond interface, resistive devices integrated on 50 μm-thick silicon dies were bonded to 500 μm-thick diamond films, and electrical power-resistance measurements were performed and compared with a finite-element model of the resulting device, including thermal conductance of the interface as a free parameter. The device consisted of planar resistors obtained by sputtering of a 10 nm-thick TiN adhesion layer and a 150 nm-thick platinum one, on a silicon substrate obtained removing the silicon handler and the SiO_2 layer from a bare Silicon-on-Insulator wafer. A picture of the silicon wafer on which several devices were integrated is shown in Fig. 2.5. Two types of devices were fabricated at the CNR-IMM laboratories, the first with two W-shaped resistances of about 12 mm of length and 0.125 mm of width (Fig.2.5.b), the other with 25 micrometric coils arranged in a 5×5 square matrix (Fig..c). At the moment, only the first type of device was utilized in our thermal conductivity measurements. Four samples were bonded in this way, namely SOD 8, 9, 11 and 12. Since the metalizations was not passivated, mechanical adhesion of the platinum resistors to the silicon substrate was very sensitive to the mounting procedure before bonding and to the diseases caused by transportation after bonding. A graphite 2.5 μm-thick buffer layer was interposed between the metalizations and the the steel cylinder exerting the uniaxial pressure, but other special precautions had to be adopted during preparation and transportation, in order to avoid failure of the procedure. SOD 8 and 9 were seriously damaged before electrical measurements, and practically destroyed during wafer level measurements. SOD 11 seemed mechanically

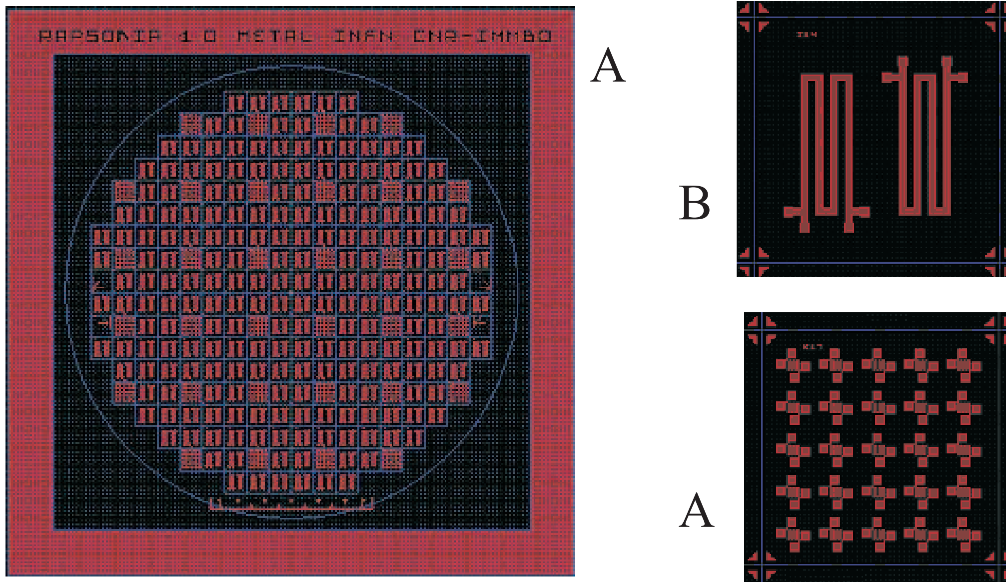

Figure 2.5: (A) Mask and the different dies of the mask: (B) wide structure and (C) narrow structure

integral, but a first temperature-ramp evidenced an abnormally high thermal resistance probably due to a not perfect platinum-silicon adhesion, confirmed also by a pronounced non-repeatability of the power-temperature characteristics. Only SOD 12, till now, has presented reproducible characteristics, probably due to the refinement of the bonding and transportation procedure. The resistors were designed to the aim of performing 4-probes measurements of injected current-voltage drop, in order to test the thermal resistance between the heat source (the resistor) and a copper sink thermally connected to the back of the sample by means of a silicon paste. During the measurements it appeared evident that the thermal resistance of the silicon-diamond interface was completely masked by the overwhelming resistance of the silicon paste. Consequently, two 4-probe contemporary measurements were performed on two adjacent resistors, the first used as a heater, with an injected current between 20 and 80 mA, the second used as a sensor, with a current of 1 mA. In this way, the high resistance of the back interface make the sensor more sensitive to the temperature drop across the silicon-diamond interface, allowing a relatively good estimate of the thermal resistivity of the interface created by the bonding procedure. A 2-dimensional finite-element simulation of the thermal behavior of the device was performed, in which thermal and geometrical characteristics of silicon and diamond were taken as known, as well as the thickness of the silicon-diamond interface (about 150 nm, from TEM measurements) and of the back interface (about 150 μm). Thermal conductance of the interfaces were left as free parameters, in or-

der to reproduce, as a function of the current in the heater, the behaviors both of heater and sensor temperatures. In Fig.2.6 a scheme of the simulation grid and the temperature field across a section of the sample are represented, as well as the best fit of the two temperatures as a function of the current in the heater. The best fit is obtained with a value of the conductance of the silicon-diamond interface of about 200 $Wm^{-1}K^{-1}$, which is intermediate between that of silicon (148 $Wm^{-1}K^{-1}$) and silicon carbide (490 $Wm^{-1}K^{-1}$).

In conclusion, at present, the thermal behavior of the silicon-diamond interface, in our devices, appears to be fully compatible with applications of SOD as silicon-on-"diamond as thermal spreader".

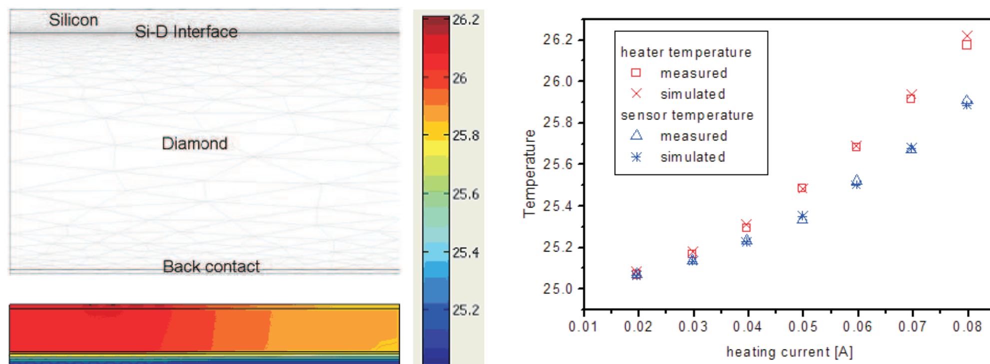

Figure 2.6: (left-up) Finite element simulation grid (left-down) Cross section of the simulated structure showing the temperature distribution. (right)Comparison between measured and simulated results for the temperature of the heater and of the sensor at various heater currents.

2.3 Structural characterization of the interface

To the aim of determining the structural and microscopical characteristics of the silicon-diamond interface, several microscopic (and destructive) techniques, as well as spectroscopic (and non-destructive) methods have been employed. All these techniques give a consistent picture of an interface resulting from melting of both a silicon and a carbon layer, followed by inter-diffusion of the two specie and the final formation of an amorphous-nanocrystalline layer whose stoichiometry depends on the grade of inter-diffusion at the moment of re-solidification. In this section the characterisation techniques and the results are presented in some detail.

2.3.1 Electron Microscopy

Three SOD samples, namely SOD8, SOD11 and SOD12 have been prepared for transmission electron microscopy (TEM) and for scanning transmission electron microscopy(STEM) with the same procedure, involving first a mechanical polishing on the silicon side until reaching a 20-30 μm thickness on the silicon die, then the preparation of a sharp slice with three electron-transparent zones by means of focused ion beam (FIB) and in situ lift-out. The preparation of each slice involves deposition of a protective layer on the sample by means of ion beam induced deposition (IBID), high current cut of the slice with 30 keV Ga^+ ions, extraction of the slice by means of micro-manipulators, welding on a TEM holder by IBID and finally low-current polishing of three zones 5 μm large and 50-80nm thick. Figure 2.7 shows a SEM and a bright field STEM image of the slice cut from SOD8. The samples have been prepared with a workstation Dual Beam FEI Strata 235M, which was used also for low energy SEM and STEM analysis, while TEM analysis has been performed with a TEM/STEM 200 keV Jeol 2200 workstation.

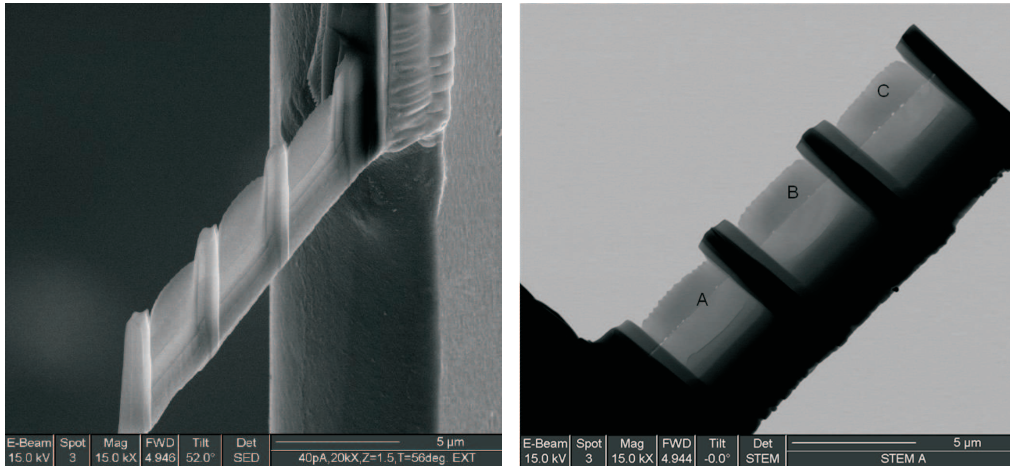

Figure 2.7: Bright field, 15 keV STEM image of the slice cutted from SOD8.

The STEM analysis of the three samples under consideration shows interfaces whith similar characteristics, quantitatively related to the process parameters. Figure 2.8 evidences an interface with quite a constant thickness for SOD8, which appears brighter than silicon and diamond, in dark field, due to the higher stopping power for electrons of the silicon carbide phases. In comparison, SOD11 (not shown) and SOD12 have interfaces of increasing and less uniform thicknesses, which are probably due to the higher energy density employed for these samples. The decreasing number of pulses per point of SOD11 and SOD12 doesn't seem to have an effect on the interface thickness, except perhaps the lower uniformity. All the

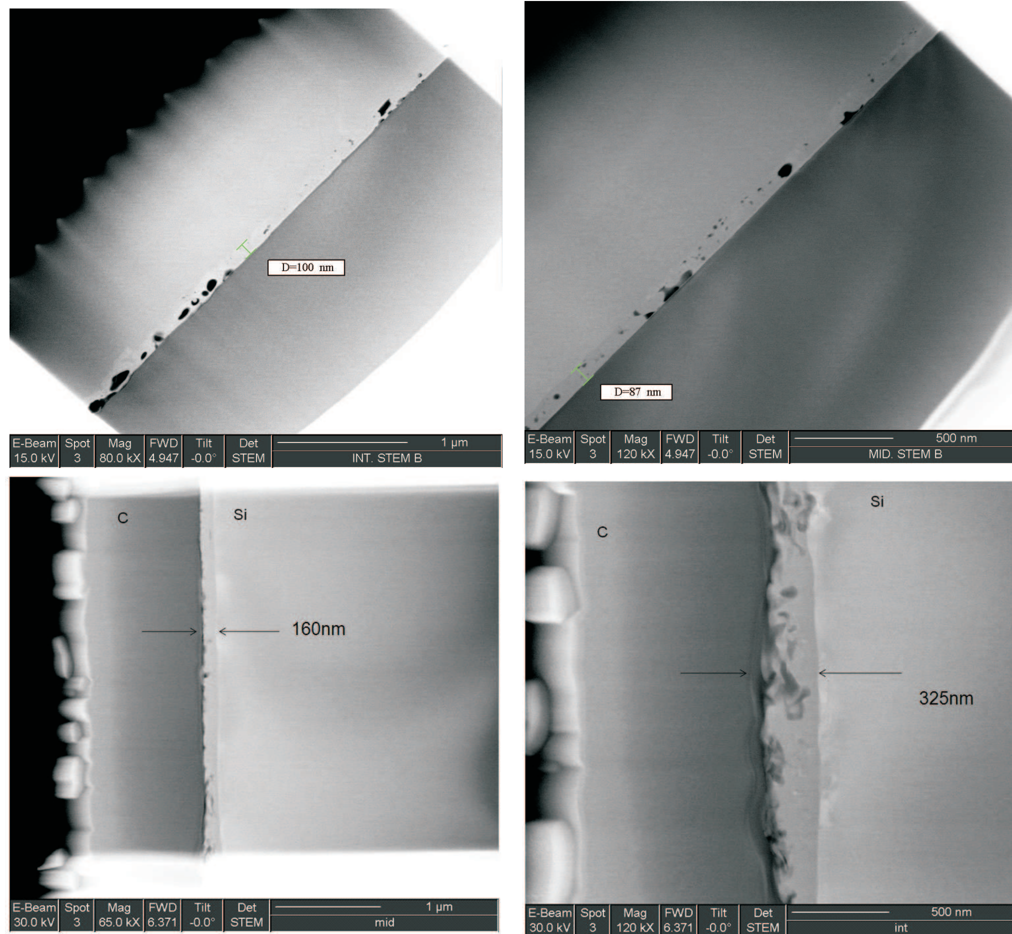

Figure 2.8: Dark field, 15 keV STEM images of SOD8 (up) and SOD12 (down).

samples under consideration present cavities, which are quite dispersed in the interface in SOD8 and more concentrated near the diamond side in SOD11 and SOD12. Cavities take up roughly 10% of the overall interface volume, and this suggested their origin to be due to the contraction of the silicon-carbide phases in comparison with an equivalent molar quantity of diamond and silicon. In fact, amorphous and crystalline silicon carbide have from 6 to 19% less volume than that of the diamond and the silicon from which they are formed. Other hypotheses for the formation of the cavities will be taken under consideration in chapter 4.

X rays microanalysis of the interface zone (see Fig. 2.9)shows a graded stoichiometry passing from carbon to silicon-rich zone in 20-30 nm (SOD8) or 40-50 nm (SOD11-12). Also a little amount of oxigen is detected, probably originated from the oxigen termination of the diamond surfaces.

High resolution TEM analysis evidences mainly an amorphous structure of the interface, with traces of crystals of nanometric size only in sample SOD8 (see Fig.2.9).

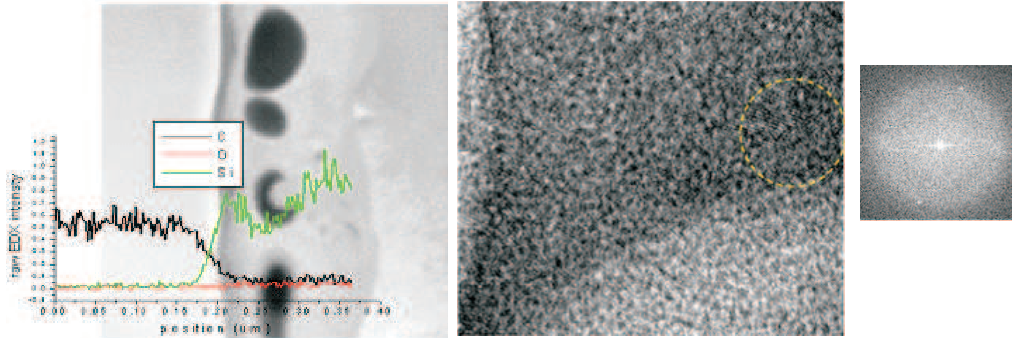

Figure 2.9: (left) Electron dispersion spectroscopy profile X ray profile of the interface of SOD8. (center) TEM image of a detail of the same sample, between two cavities. (right) Fourier transform image of the same TEM field from which results traces of nanocrystalline structures.

In conclusion, microscopic STEM and TEM analyses of the interfaces evidence an amorphous or nano-crystalline layer whose thickness seems to be related to the surface energy density per pulse of the laser beam and whose uniformity is perhaps better for a larger number of pulses per welding point. The interface appears to be carbon-rich on the diamond side with increasing depths at increasing energy density, and is affected by voids whose total volume is roughly around 10% of the overal interface volume.

2.3.2 Micro-Raman analysis

Raman analysis was performed in back-scattering configuration on the samples SOD1, SOD3, SOD5 and SOD6 with a micro-Raman apparatus, in order to investigate the chemical and structural nature of the obtained SOD interface. The back-diffused spectra, after passage through a notch filter, were analyzed with a single monochromator, and a CCD array, with a spectral resolution of about 1 cm^{-1}. Measurements were performed, in the range from 100 cm^{-1} to 3500 cm^{-1}, with the 647.1 nm and the 752.5 nm Kr laser lines: the two red emissions were used to evidence possible sp^2 bonds[37] and to minimize contributions of diamond fluorescence. Only in some of the points of all the samples under consideration, signature from sp^2 carbon[38] was found (see Fig.2.10) while a sensible amorphous silicon signature[39] was ubiquitously detected in all the investigated samples (see Figure 2.10).

By inspection of the Raman profile, the thickness of the amorphous layer can be evaluated by comparison of the intensity of the silicon Raman peak at 520 cm^{-1} with that of the broad band of amorphous silicon[40] between 400 and 550 cm^-1. Their ratios can be related to the Raman cross-section per unit volume of amorphous ($1/\lambda_a$) to crystalline silicon ($1/\lambda_{cr}$), and to the absorption coefficients of the amorphous (α_a) and crystalline phase (α_{cr}) in the following way. The radiance of the Raman scattered radiation from a layer of thickness dz at the depth z is given by

$$dL = L_0 \frac{dz}{\lambda} \exp \left[-2 \int_0^z \alpha(z') \, dz' \right], \tag{2.7}$$

where the absorption coefficient of the Raman radiation was assumed to be about equal to that of the incident light. It follows that, if silicon is amorphous up to the depth d and crystalline in the deeper layers, the ratio between the radiance from the amorphous and that from the crystalline silicon is given by:

$$r_{a-cr} \equiv \frac{L_{\text{a-Si}}}{L_{\text{cr-Si}}} = \frac{\int_0^d \frac{dz}{\lambda_a} \exp(-2\alpha_a z)}{\exp(-2\alpha_a d) \int_d^\infty \frac{dz}{\lambda_{cr}} \exp(-2\alpha_{cr} z)} = 2\alpha_{cr} d \times \frac{\lambda_{cr}}{\lambda_a} f(2\alpha_a d); \tag{2.8}$$

where $f(x) = (e^x - 1)/x$ approaches 1 for small values of x. It is worth noting that the ratio r_{a-cr} is not dependent on the presence of a possible silicon carbide layer *above* the amorphous silicon one. In order to exploit equation2.7 for measurement of the amorphous layer thickness, an evaluation of the ratio $\frac{\lambda_{cr}}{\lambda_a}$ is necessary. This ratio depends on the grade of silicon amorphization, in fact it ranges from about 10 for completely amorphous phases[39], to about 1 in cases of nanocrystallites whose size greatly exceeds about 25 nm. According to ref.[41], the behavior of the ratio $\frac{\lambda_{cr}}{\lambda_a}$ as a function of the crystallite size s is well described by $\frac{\lambda_{cr}}{\lambda_a} = 1 + 10 \exp(-s/25\text{nm})$, thus, the thickness of the amorphous layer could be calculated by:

$$d \times (1 + 10 \exp(-s/25\text{nm})) = \frac{r_{a-cr}}{2\alpha_{cr}} \equiv d_{\text{eff.}}. \tag{2.9}$$

Unfortunately, in Eq.2.9, the size s ranges *a priori*, in its very nature, from 0 to d, which implies a considerable uncertainty on the esteem of d itself for a given $d_{\text{eff.}}$. For example, with $r_{a-cr} = 0.05$, given $\alpha_{cr} = 2.1 \times 10^3 \text{cm}^{-1}$ (relative to the wavelength of 753 nm), we have $d_{\text{eff.}} = 120\text{nm}$, which gives a range of uncertainty for d from 10 to 100 nm. Also the TEM analysis performed on some of the samples gives a limited information on the size s of the crystallites, being their presence non uniformly assessed on all the samples surface. Nevertheless, to the aim of disposing of a non destructive, semi-quantitative estimate of the amorphous damaged layer, the length $d_{\text{eff.}}$ gives a good upper limit easily deduced from the Raman profile.

Back diffused spectra were fitted, in the range 400-580 cm^{-1}, with a sum of three contributions: a Gaussian distribution centered at 480 cm^{-1} with standard

deviation 25 cm^{-1}, reproducing the Raman spectrum of amorphous silicon as indicated in ref.[40], a pseudo-Voight profile centered at 520 cm^{-1} taking into account the contribution of crystalline silicon, whose form is given by

$$L_{cr}(x) = L_{\text{cr-Si}} \left(\frac{1-\eta}{\sigma_G \sqrt{2\pi}} e^{\left[-\frac{\left(x-520\ \text{cm}^{-1}\right)^2}{2\sigma_G^2} \right]} + \frac{\eta \sigma_L}{2\pi} \frac{1}{\left(x-520\ \text{cm}^{-1}\right)^2 + \left(\sigma_L/2\right)^2} \right) \tag{2.10}$$

and a linear function reproducing, in the relatively limited range under consideration, the luminescence of diamond, whose characteristics are widely variable also in a single sample at different positions. The fit parameters were the two luminescences $L_{\text{cr-Si}}$ and $L_{\text{a-Si}}$, relative to crystalline and amorphous silicon respectively, the width of the Gaussian and Lorentzian contribution σ_G and σ_L, and the relative weight η in the pseudo-Voigt profile, the relative weight η of the Lorentzian part. Several points in the four samples under consideration were analyzed and compared with three spectra acquired in points where silicon were hit by radiation. In figure 2.10 an histogram of the relative frequency of the values of the ratio r_{a-cr} for irradiated and non irradiated points is shown, together with a typical spectra from which the linear contribution of luminescence has already been subtracted. The negative value of r_{a-cr} for un-irradiated points can be attributed to a slight convexity of the luminescence profile, correction to this effect can be acquainted taking as effective values for the irradiated samples the difference between the fit value and the mean value of the un-irradiated points. It is evident from the histogram the significance of the yet weak feature attributed to amorphous silicon.

It was not possible to correlate definitely the ratio r_{a-cr} to the different energy density per pulse or to the different number of pulses with which the samples under consideration were irradiated. In fact, the uniformity of the irradiation, at this level, is still too poor to allow such an analysis. Nevertheless, a feature we can usefully extract from these measurements was that the effective thickness $d_{\text{eff.}}$, a good superior estemate of the physical extension of the amorphized layer, never exceeded 170 nm, with a mean value of about 85 nm.

2.3.3 Fourier Transform Infrared Analysis

A Fourier transform infrared analysis set-up with a principal Michelson arm of 3 meters, and a frequency resolution of 0.3 cm^{-1}, utilizing a thermal source and a cooled InSb photoconductor as sensor, has been employed in the infrared transmittance analysis of the samples SOD1, SOD2, SOD3 and SOD6, in the range 570-5000 cm^{-1}. Both silicon and diamond show important features in the range under consideration, mainly due to 2-phonon absorption. Thus, a possible signature from the

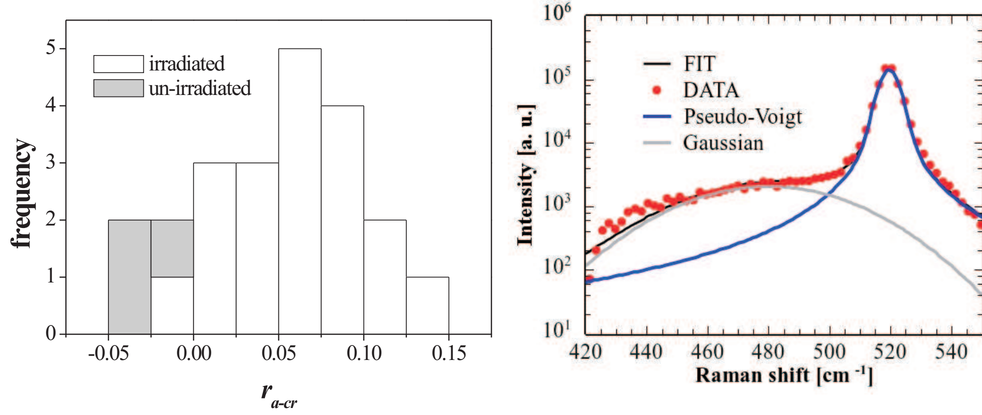

Figure 2.10: (right) Raman SOD profile (after subtracting the diamond luminescence background) fitted to a sum of a c-Si pseudo-Voigt profile and an a-Si broad Gaussian, centered at 480 cm-1 with a 25 cm-1 sigma. (left) frequency distribution of the ratios a-Si/c-Si compared to that of unirradiated samples.

polar bonds C-Si needs to be revealed by comparison of bounded and un-bounded samples. To this aim absorbance of different areas of a same sample, either invested by the laser pulses or left un-exposed, has been subtracted, in a way to have about the same absorption by crystalline silicon and diamond and to reveal, by the ratio of the signal I/I_{ref},(proportional to the difference in absorbance), the contribution of the silicon-carbon (or silicon carbide) layer. In this way, we extracted the absorbance of the interface layer in term of

$$Abs = -\log_{10}\left(\frac{I}{I_{\text{ref}}}\right) = \alpha x \log_{10} e, \tag{2.11}$$

where α and x are respectively the absorption coefficient and the layer thickness.

A typical result in shown in Fig.2.11, were a definite, wide feature centered at about 800 nm emerges from a weak oscillating background due to multiple reflections between the parallel-plane faces of the sample. Comparison with literature[42] allows to assign this signature to stretching-modes of an amorphous or nano-crystalline form of silicon carbide. Since the thickness of the nanocrystalline layer in ref. [42] is known, the analysis gives straightforwardly the equivalent thickness of our silicon carbide layers. By a closer inspection, the peak at 800 cm^{-1} shows a shoulder at the lower wavenumber side whose height is not proportional to the intensity of the principal peak. For this reason, this feature has been assigned to a different, not yet understood mechanism of absorption, and has been subtracted from the signal in order to extract the contribution of the silicon-carbide absorption alone.

The analysis of the spectra was performed fitting the profiles before 700 cm^{-1} and between 950 and 1250 cm^{-1} with a linear profile, plus a sinusoidal one, plus a Gaussian one centered at 700 cm^{-1}, reproducing the shoulder at the left of the principal peak. The difference Abs_{SiC}, between the spectrum and the sum of all these contributions, has been assumed to be due to the silicon carbide layer, and its integral over the frequency has been compared with that of the reference[42] whose thickness of 35 nm was independently assessed. Two plots of Abs_{SiC}, together with the reference one, are shown in figure 2.11. Since some points of the samples with the lower number of pulses per point (10) give no detectable signal, it is important to determine the limit of sensitivity of the method. This was done by varying some of the fitting parameters of the background (e.g. the frequency, or the amplitude) in a way not to alter significantly the adherence to the experimental profile, then re-calculating Abs_{SiC}, and finally assuming the error of the measure (and the sensitivity of the method) equal to the difference with the previous value. We found a limit of sensitivity of about 3 nm of equivalent silicon carbide thickness.

The evaluated thickness of the silicon-carbon layer, yet not uniform over the sample surface, shows a loose correleation with the number of pulses per point, ranging from about 50 nm at the higher number of pulses (50) to the limit of sensitivity or below at 10 pulses per point.

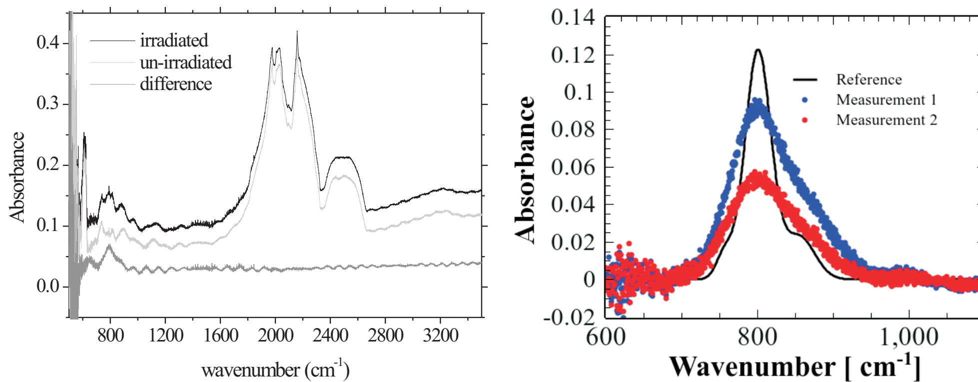

Figure 2.11: (left) FTIR profile of the absorbance for irradiated and un-irradiated areas of the sample SOD1, along with the difference between them. (right) Absorbance profiles of two different irradiated areas of the same sample, to be compared with the reference profile[42] also shown in black.

2.4 Conclusions and perspectives

Functional and structural tests of the silicon-on-diamond samples obtained by pulsed-laser bonding give indications about the validity of this technique for the applications of interest, moreover, they also put in evidence some limits and drawbacks which underline some possible directions toward the optimization of the process. It is evident that a mechanically stable and thermally conducting interface has been obtained, which opens the way toward post bonding processing and thermal applications, but the damaged silicon layer, at present, seems slightly too thick for the most large integration scales, which requires, in the SOI concept, silicon thicknesses of a few tens nanometers. Moreover, the presence of nano-cavities inside the interface volume is undoubtedly detrimental of its thermal characteristics, and should be avoided if possible. Another weak point of the process is the very high pre-bonding pressure that is necessary, with the present silicon and (mostly) diamond surfaces, to make the contact close enough to assure success of the bonding process. A substantial reduction of the pre-bonding uni-axial stress seems mandatory for the scaling-up of the bonding process from the die (5 mm) to the wafer (5 cm) scale.

A thorough theoretical investigation of the physical processes that take place during irradiation and also before it, in the compression phase, is highly desirable in order to make progresses in the optimization of the bonding process. In fact, the huge number of process-parameters which are in our control make unworkable in term of time and costs an exhaustive experimental investigation, involving independent variations in laser wavelength, pulse width, energy density, number of pulses per point, degree of polishing of the surfaces, uni-axial exerted pressure. To such an investigation the next two chapters are devoted.

Chapter 3

Modeling of laser bonding

Microelectronics applications of the Silicon-on-Diamond concept, possibly with diamond directly bonded to a pre-integrated silicon chip, requires on one hand a damaged layer as thin as possible, on the other, a low thermal budget in charge of the integrated electronics. Thus, the optimization of the process has to deal with modeling of the laser heating, in a way to predict, at a specific power density and wavelength, the evolution of the temperature field and of the fusion front during and after laser irradiation.

To this aim, I developed a numerical model of the bonding process which takes into account three process parameters, that are wavelength, energy density per unit surface, and pulse width, and gives predictions about the energy threshold for the silicon-diamond adhesion and about the minimum thickness of the damaged layer which corresponds to this threshold [43]. I limited the analysis to the first pulse, without taking into account the further ones, because their dynamics depends strictly on the optical characteristics of the amorphous layer left behind by the first one, which are believed to be strongly dependent on the amorphization conditions, whose determination should require an additional experimental effort. Nevertheless, this limitation doesn't alter the validity of the conclusions, because the carbon-melting threshold depends much more on the absorption-reflection characteristics of the melted silicon than on those of the pre-existing solid phase. Moreover, I concentrated on the carbon-melting threshold, without considering the dynamics of carbon fusion and inter-diffusion in silicon, avoiding further considerable thermodynamic complications also because, in order to optimize the process, it is of prominent interest to remain as close as possible to the threshold conditions. This is particularly true for the issue of cavity formation in the diamond-silicon interface (described in chapter 2) which, if ascribable to the contraction of the carbon-rich phases, can be partially avoided by the minimization of the thickness of the melted carbon layer.

Theoretical modelization of the laser bonding method can take advantage of a huge amount of experimental and theoretical studies on the interaction between matter and light under extreme conditions, but has to deal also with certain unexplored issues. Silicon was one of the first and better studied targets for pulsed laser irradiations, particularly since, in the late seventies, laser annealing of ion implanted silicon came to the attention of the researchers (see ref.[44] for a comprehensive review). Nevertheless, in our experimental conditions, with a very rigid and thermally conductive diamond layer in front of the silicon one, the temperature field acquires some peculiar characteristics: variations in pressure fields can no more be neglected, moreover, melting begins inside silicon while two melting-recrystallization fronts propagates in opposite directions during and after the pulse. Moreover, if we want to follow the behavior of the interface until carbon begins to melt, in such a way that silicon carbide phases can be formed, as suggested by infrared spectroscopy[45], we have to model the behavior of carbon at high temperatures and pressures, in a regime which has been intensively studied but yet not clearly understood, remaining significant uncertainty in some key-parameters as thermal conductivity of the liquid phase (see ref.[46] for a review).

In this chapter, after an extended survey of the physical phenomena and relative time and length scales occurring at the interface of silicon and diamond (section 3.1), a description of the analytical model is given in section 3.2, while in section 3.3 details are given about the numerical solution of the equations. In section 3.4 several key parameters as energy thresholds, interface reflectance and thickness of the damaged layer are determined by calculation, as functions of the parameters under our control. Finally, in section 3.5, I compare the results of calculation with the data available so far, in order to underline strategies for the optimization of the process.

3.1 Phenomena involved and their time and length scales

3.1.1 absorption, transmission, reflection of radiation

If we follow the heating process before diamond reaches its graphitization conditions, transport of radiation is mainly ruled by the contrast in refraction index both between diamond and silicon and between solid and liquid silicon (determining reflection of the radiation), as well as by the absorption coefficient of silicon in the solid and the liquid phase. At a wavelength of 355 nm (for instance), the reflection coefficient of the diamond-silicon interface varies from about 0.25 to 0.5 passing from room temperature to the melting condition of silicon. The absorption length,

at the same wavelength, ranges from 19 nm in the solid phase to 13 nm (at longer wavelengths the difference is much sharper, for instance, at 532 nm it passes from 970 nm in the solid to 17 nm in the liquid phase). The optical properties of silicon are also significantly affected by the presence of the electron-hole plasma generated by laser irradiation, which has to be properly taken into account. Moreover, during the fusion process, while the melting front propagates in silicon, internal reflection and refraction play a relevant role, requiring the implementation of a full multilayer model of light propagation, in order to calculate the power absorption at each layer inside the material. The presence of a rigid diamond layer in contact with silicon determines significant differences in the behavior of silicon at high temperatures. In heating experiments, for which the volume of a liquid metal can freely expand, one expects that in proximity of the critical temperature the resistivity drops several order of magnitude and the material becomes transparent[47, 48]. This is not the case of silicon if it is confined by a rigid material like diamond, because liquid silicon cannot reach the volume that is necessary for the metal-dielectric transition. In this case we expect that, in the diffuse liquid-gas transition taking place well above the critical pressure (530 atm) of silicon, the optical characteristics of the material do not undergo dramatic variations.

3.1.2 generation, diffusion, recombination and energy relaxation of electron-hole plasma

In the solid phase, light absorption does not determine a direct thermal release to the lattice, but a hot electron-hole plasma, generated by the over band-gap irradiation, diffuses across the silicon bulk, recombining and releasing its energy to the lattice. Thus, the width of the heated layer is not limited only by the absorption length of the radiation and the thermal diffusion length, but it extends to the carrier diffusion length, which on its turn depends on the ambipolar diffusion coefficient and the recombination time. For the high power densities under interest, recombination is expected to occur mainly by the Auger mechanism, with a lower limit to the recombination time of about 6 ps imposed by screening effects[49]. Ambipolar diffusion depends both on plasma and on lattice temperatures (see subsection 3.2.3) with values ranging over several hundreds of cm^2s^{-1}, giving a diffusion length of several hundreds of nanometers, much more large than the simple absorption length in the UV range. Since Auger recombination does not affect the energy balance of the plasma, because the energy of each electron-hole recombining couple is relaxed to the plasma itself, the only significant way of relaxing energy to the lattice is electron-phonon interaction, which occurs with a time constant of a few hundreds femtoseconds[50] if plasma densities does not exceed about 10^{21} cm^{-3}. On the other hand, for electron densities much above this value the population of electronic bands

dramatically weakens covalent bonds, resulting in a melting transition to a metallic state[51]. In our modelization we will not consider silicon in such a transformation, thus limiting ourself to pulse width of no less than some hundreds of femtoseconds and energies not exceeding about 10 J/cm^2.

3.1.3 Temperature, pressure and phase fields

Before melting, the pressure field is influenced by temperature by means of a source term depending on bulk modulus and on the thermal expansion coefficient of the media. On the other hand, also the pressure is involved in temperature evolution trough the associated TdS equation. During melting, pressure is also strongly affected by the change in volume of the melting material. There is in general a time scale much above which these reciprocal influences of temperature and pressure can be neglected, which is given by the ratio of the typical lengths involved in heat release over the sound velocity. This time scale amount to some tens of picoseconds, being sound velocity in silicon about 8400 m/s and the typical thickness of the layers interested by the heat release ranging over tens to hundreds of nanometers. Since we are also interested in pulse durations of this order of magnitude or below, we are forced to consider all the possible interactions of temperature, pressure and a phase field representing, for each layer in the media, the fraction of the melted material. In this way, important pressure-dependent parameters, such as the graphitization temperature of diamond, can be taken into account.

After the laser-pulse duration, two solidification fronts propagates in the media in opposite directions, instead of only one as in silicon laser annealing or any other case in which irradiation takes place in air or vacuum. The velocity of these solidification fronts strongly influences the solid phase observed, thus the model has been applied to the simulation of the solidification phase too.

3.2 The model

The model takes into account five mutually interacting fields: electron-hole plasma density n, its kinetic energy density E, the lattice temperature T and pressure P, and the phase field ϕ, defined as the mass fraction of the material which is melted in a "small" neighborhood of the point under consideration. The power released to the unit volume of the material by the radiation is indicated with w, and it is calculated taking into account also the internal reflections between different layers inside silicon, considering, for each layer in the media, the energy released by a progressive and a regressive wave, with the appropriated boundary conditions between each layer and the neighbor ones. Details about the calculation of w are given in subsection 3.2.1.

In order not to interrupt the development of the theory with necessary but minor specifications, proofs of equations employed in the theory and details about physical parameters intervening in calculations are also contained in the subsections 3.2.2, 3.2.3 and 3.2.4.

Electron-hole plasma dynamics is taken into account adopting a set of equations which are basically those adopted by Lietoila and Gibbon[52] and Agassi[53], but considering that in the partially melted layers ($0 < \phi < 1$), the energy is released to the plasma and to the atoms of the melted phase in parts which are proportional to $(1-\phi)$ and ϕ, respectively. The equations for the n and for E are then:

$$\frac{\partial n}{\partial t} = \frac{\partial}{\partial x}\left(D_a \frac{\partial n}{\partial x}\right) + \psi\left(1-\phi\right)\frac{w}{h\nu} - \frac{n-n_0}{\tau_A}, \tag{3.1}$$

$$\frac{\partial E}{\partial t} = \frac{\partial}{\partial x} k_e \frac{\partial}{\partial x}\frac{E}{3k_B n} + \frac{\partial}{\partial x} D_a \frac{E}{n}\frac{\partial}{\partial x} n - \frac{E-3k_B nT}{\tau_{e-ph}} + \left(1-\phi\right)\frac{h\nu - \psi E_g}{h\nu} w + E_g \frac{n-n_0}{\tau_A} - n\frac{\partial E_g}{\partial t}. \tag{3.2}$$

In Eq. 3.1 and 3.2, D_a is the ambipolar diffusivity, k_e is the plasma thermal conductivity, τ_A and τ_{e-ph} are the Auger recombination time and the electron-phonon relaxation time, respectively, n_0 is the equilibrium carrier density, E_g is the band-gap width, ν is the radiation frequency, while h, k_B and e are the Planck constant, the Boltzmann constant and the value of the elementary charge, respectively. The factor ψ, in the equations, represents the ratio between the energy absorbed in the electron-hole generation and the overall energy absorbed by the free carriers too. It has been calculated as shown in section 3.2.1, dedicated to the study of the energy transfer from the radiation to the matter.

The fields T, P and ϕ are bounded by the thermodynamic conditions, by the law of motion and by a constraint condition which is different for a mono-phase ($\phi = 0$ or 1) and a bi-phase ($0 < \phi < 1$) layer. The second equation of TdS implies

$$\rho_0 c_\phi \frac{\partial T}{\partial t} - \rho_0 T\left(\frac{\alpha}{\rho}\right)_\phi \frac{\partial P}{\partial t} + \rho_0 \lambda \frac{\partial \phi}{\partial t} = \frac{\partial}{\partial x}\left(k_{th\phi}\frac{\partial T}{\partial x}\right) + \frac{E-3k_B nT}{\tau_{e-ph}} + \phi w. \tag{3.3}$$

In Eq.3.3, ρ, α, λ, c and k_{th} represents, respectively, density, thermal expansion coefficient, latent heat of fusion, specific heat at constant pressure and lattice thermal conductivity. The subscript 0, here and in the following, indicates the values at room temperature and pressure, while the subscript ϕ, appended to any physical quantity f, means a weighted average between the values of f for the solid and the liquid, that is $f_\phi = (1-\phi)\, f_S + \phi f_L$. The equation of motion of the system is the following

$$\left(\frac{1}{\rho B}\right)_\phi \frac{\partial^2 P}{\partial t^2} - \left(\frac{\alpha}{\rho}\right)_\phi \frac{\partial^2 T}{\partial t^2} + \left(\frac{1}{\rho_S} - \frac{1}{\rho_L}\right)\frac{\partial^2 \phi}{\partial t^2} = \frac{1}{\rho_0^2}\frac{\partial^2 P}{\partial x^2}, \tag{3.4}$$

where B is the bulk modulus. Proofs of Eq.3.3 and 3.4 can be found in subsection 3.2.2. The constrain condition for the mono-phase layers is simply

$$\frac{\partial \phi}{\partial t} = 0; \tag{3.5}$$

while for the bi-phase layers pressure and temperature are bounded by the melting curve, and the differential relation between their derivatives is

$$\left(\frac{dP}{dT}\right)_{\text{melt.}} \times \frac{\partial T}{\partial t} - \frac{\partial P}{\partial t} = 0. \tag{3.6}$$

During silicon melting, since the density of the liquid phase of silicon is higher than that of the solid one, pressure undergoes a dramatic decrease, eventually reaching the triple point conditions. In this state a second phase field taking into account the relative proportion of the vapor phase could be necessary. Nevertheless, the density of the vapor phase is so low, and the volumes involved so small, that the energy balance is not affected by the assumption that the mass fraction of the vapor phase is zero. In this conditions, the equation that rules the evolution of the system is Eq. 3.3, with the constraints

$$\frac{\partial T}{\partial t} = 0 \text{ and } \frac{\partial P}{\partial t} = 0. \tag{3.7}$$

When, in a melting layer at the triple point, all the solid mass is disappeared, then the material follows the vaporization curve. Also in this case, the vapor mass fraction is negligible due to its small extension in volume, and the pressure is so low, compared to that of the solid and liquid heated layers, that the constraints to the Eq. Eq. 3.3 can be assumed to be the following:

$$\frac{\partial \phi}{\partial t} = 0 \text{ and } \frac{\partial P}{\partial t} = 0. \tag{3.8}$$

Layers which lies along the vaporization curve remain on it until the volume of the liquid v, which can be traced by means of the equation of state $\rho(P,T)$, fills the space v_{ext} left void by the surrounding layers. At this point the system begins to move across the liquid area of the phase diagram, eventually reaching the gas phase with a diffuse, over-critical liquid-gas transition. Numerical solutions of Eq.3.1 to Eq.3.8 was found following a backward Euler scheme for the diffusion equations3.1-3.3, and a forward Euler one for the wave equation 3.4. The equations 3.3 to 3.8, which couple the fields P, T and ϕ, require the simultaneous inversion of a system involving the three fields. At each time step, when the state of a given layer changes between a mono-phase and a multi-phase situation, also the structure of the equations has to change accordingly, due to the different constraint (Eq.3.5 to 3.61) imposed to the material. In section 3.3 details about calculations are given. In figure 3.1 a schematics of the tests performed on the state of each layer is drawn.

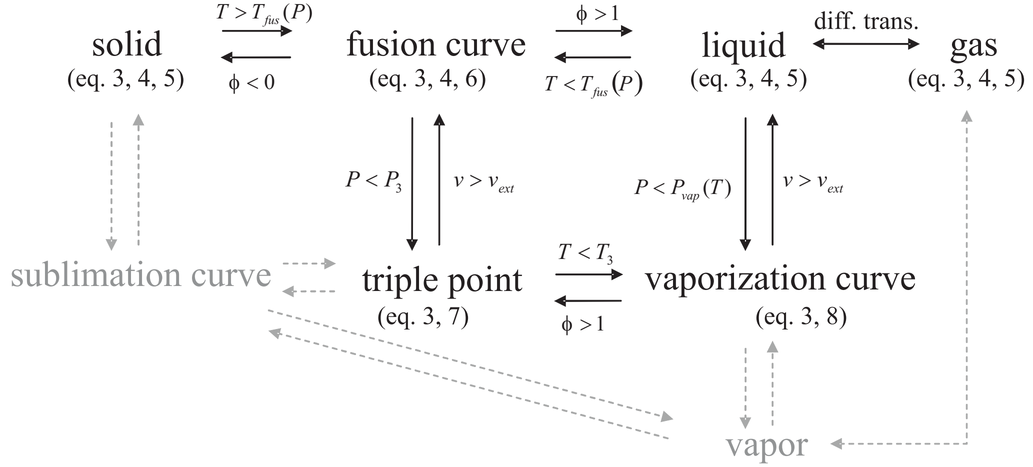

Figure 3.1: Flux diagram of the tests (arrows) which, at each time step, decide the transitions between the various areas, or lines, or points, in the phase diagram. In parentheses an indication of the procedure performed on each layer and at each time step, according to the state in which a given layer is found. In grey, states and transitions which are irrelevant for this work.

3.2.1 Energy transfer to matter

I have performed the calculation of the energy released by the electromagnetic radiation for each one of the N layers of thickness δ_i ($1 \leq i \leq N$), of the finite element calculation grid, taking into account the complex refractive index $\widehat{n}_i \equiv n_i + ik_i$ of each layer. Both the real and the imaginary part of $\widehat{n}$ depends on the "intrinsic" contribution $n_{(0)} + k_{(0)}$, due to atomic ionization, and on the contribution of the free carriers. The latter is taken into account, as in ref.[52], considering that the effective (real) index of refraction n_e and the extinction coefficient k_p of the electron-hole plasma are bounded by

$$n_e{}^2 - k_p^2 = n_{(0)}{}^2 - \left(\frac{\omega_p}{\omega}\right)^2 \quad \text{and} \quad 2n_e k_p = \frac{e}{2}\frac{\omega_p^2}{\omega^3}\left(\frac{1}{\mu_e m_e} + \frac{1}{\mu_h m_h}\right) g, \tag{3.9}$$

where $\omega_p = \sqrt{n\frac{e^2}{\epsilon_0}\left(\frac{1}{m_e} + \frac{1}{m_h}\right)}$ is the plasma pulsation (n is the plasma density), ω is the radiation pulsation, $\mu_{e,h}$ and $m_{e,h}$ are the electron and hole mobility and effective mass, respectively, e and ϵ_0 are the elementary charge and the vacuum dielectric constant, while g is a factor depending on the scattering mechanisms, evaluated as $g \approx 1.13$ for the phonon scattering. The effective extinction coefficient k_e is given, as in ref [52], by the sum of the intrinsic value $k_{(0)}$ and the extinction coefficient k_p of the plasma, but with a weight depending on the proportion of the solid phase: $k_e =$

$k_{(0)} + k_p(1-\phi)$. The values of $n_{(0)}$ and $k_{(0)}$, on their turn, are given by a weighted sum of kind $n_{(0)} = n_{(0)S}(1-\phi)+n_{(0)L}\phi$ and $k_{(0)} = k_{(0)S}(1-\phi)+k_{(0)L}\phi$, where $n_{(0)S,L}$ and $k_{(0)S,L}$ will be specified in section 3.2.3, dedicated to the physical parameters employed in the simulation. On the base of $k_{(0)}$ and k_p, also the proportion ψ of the energy absorbed by ionization respect to the overall energy absorbed by the free carriers too has been calculated as $\psi = k_{(0)}/\left(k_{(0)}+k_p\right)$.

Once given the optical functions of each layer, we can calculate, for a given intensity of the incident radiation, the energy released to each layer. Let the electric field inside the ith layer be given by

$$E_i(x,t) = \overline{E}_i(x)\, e^{-i\omega t} \quad \text{with} \quad \overline{E}_i(x) = E_i^+ e^{i\frac{2\pi}{\lambda_0}\widehat{n}_i(x-x_i)} + E_i^- e^{-i\frac{2\pi}{\lambda_0}\widehat{n}_i(x-x_i)} \tag{3.10}$$

where $E_i^{\pm}$ are complex amplitudes of a progressive and a regressive wave, x_i is the central coordinate of the layer, and λ_0 is the wavelength of the radiation. The field in diamond before the 1st layer is expressed as

$$E_0(x,t) = \overline{E}_0(x)\, e^{-i\omega t} \quad \text{with} \quad \overline{E}_0(x) = E^{\text{inc}} e^{i\frac{2\pi}{\lambda_0}\widehat{n}_0 x} + E^{\text{ref}} e^{-i\frac{2\pi}{\lambda_0}\widehat{n}_0 x}, \tag{3.11}$$

while the electric field in silicon after the Nth layer is

$$E_{N+1}(x,t) = \overline{E}_{N+1}(x)\, e^{-i\omega t} \quad \text{with} \quad \overline{E}_{N+1}(x) = E^{\text{tr}} e^{i\frac{2\pi}{\lambda_0}\widehat{n}_{N+1} x}. \tag{3.12}$$

Continuity both of transverse electric and magnetic fields at the layers interface is assured by continuity of the electric field and of its first derivative, which results in two conditions for each boundary between adjacent elements of the grid. Taking also into account the boundary between the first simulated diamond layer and the diamond layer in front of it (boundary between $i = 0$ and $i = 1$) and between the last simulated silicon layer ($i = N$) and the rest of the material we have $2(N+1)$ conditions. Considering E^{inc} as a known quantity, and $\epsilon_i^{\pm} \equiv E_i^{\pm}/E^{\text{inc}}$ as unknown, as well as $\epsilon^{\text{ref,tr}} \equiv E^{\text{ref,tr}}/E^{\text{inc}}$, we have the following linear system of $2(N+1)$ equations in the $2(N+1)$ unknowns:

$$\begin{aligned}
1+\epsilon^{\text{ref}} &= \epsilon_1^+ e^{-i\frac{\pi}{\lambda_0}(\widehat{n}_1)\delta_1} + \epsilon_1^- e^{i\frac{\pi}{\lambda_0}(\widehat{n}_1)\delta_1}; \\
1-\epsilon^{\text{ref}} &= \widehat{n}_1\left(\epsilon_1^+ e^{-i\frac{\pi}{\lambda_0}(\widehat{n}_1)\delta_1} - \epsilon_1^- e^{i\frac{\pi}{\lambda_0}(\widehat{n}_1)\delta_1}\right); \\
\epsilon_i^+ e^{i\frac{\pi}{\lambda_0}(\widehat{n}_i)\delta_i} + \epsilon_i^- e^{-i\frac{\pi}{\lambda_0}(\widehat{n}_i)\delta_i} &= \epsilon_{i+1}^+ e^{-i\frac{\pi}{\lambda_0}(\widehat{n}_{i+1})\delta_{i+1}} + \epsilon_{i+1}^- e^{i\frac{\pi}{\lambda_0}(\widehat{n}_{i+1})\delta_{i+1}}; \\
\widehat{n}_i\left(\epsilon_i^+ e^{i\frac{\pi}{\lambda_0}\widehat{n}_i\delta_i} - \epsilon_i^- e^{-i\frac{\pi}{\lambda_0}\widehat{n}_i\delta_i}\right) &= \widehat{n}_{i+1}\left(\epsilon_{i+1}^+ e^{-i\frac{\pi}{\lambda_0}\widehat{n}_{i+1}\delta_{i+1}} - \epsilon_{i+1}^- e^{i\frac{\pi}{\lambda_0}\widehat{n}_{i+1}\delta_{i+1}}\right); \\
\epsilon_N^+ e^{i\frac{\pi}{\lambda_0}\widehat{n}_N\delta_N} + \epsilon_N^- e^{-i\frac{\pi}{\lambda_0}\widehat{n}_N\delta_N} &= \epsilon^{\text{tr}} \\
\widehat{n}_N\left(\epsilon_N^+ e^{i\frac{\pi}{\lambda_0}\widehat{n}_N\delta_N} - \epsilon_N^- e^{-i\frac{\pi}{\lambda_0}\widehat{n}_N\delta_N}\right) &= \widehat{n}_{N+1}\epsilon^{\text{tr}}
\end{aligned} \tag{3.13}$$

The sistem has been solved reducing it at the superior triangular form and then calculating the unknowns by consecutive substitutions.

At this point the power w_i released at each layer i has been calculated first considering the Poynting vector at a given position x in the material, whose component along the propagation direction has a value, averaged on the radiation period, given by:

$$\overline{S} = \frac{1}{2}\Re\left(\frac{\vec{E}_i \wedge \vec{B}_i^*}{\mu_0}\right)\cdot \vec{u}_x \quad \text{with} \tag{3.14}$$

$$\vec{E}_i\left(x\right) = \vec{e}\left(E_i^+ e^{i\frac{2\pi\widehat{n}_i}{\lambda_0}x} + E_i^- e^{-i\frac{2\pi\widehat{n}_i}{\lambda_0}x}\right) \quad \text{and}$$

$$\vec{B}_i\left(x\right) = \frac{\widehat{n}_i}{c}\vec{u}_x \wedge \vec{e}\left(E_i^+ e^{i\frac{2\pi\widehat{n}_i}{\lambda_0}x} - E_i^- e^{-i\frac{2\pi\widehat{n}_i}{\lambda_0}x}\right).$$

With these notations, it is easily shown that the average power per unit surface w_i is

$$\begin{aligned} w_i = \quad & \overline{S}\left(x_i - \frac{\delta_i}{2}\right) - \overline{S}\left(x_i + \frac{\delta_i}{2}\right) = \\ & 2\left[\frac{n_i}{n_0}\left(\left|\epsilon_i^+\right|^2 + \left|\epsilon_i^-\right|^2\right)\sinh\left(\frac{2\pi}{\lambda_0}k_i\delta_i\right) + \frac{k_i}{n_0}\left(\epsilon_i^{+*}\epsilon_i^- + \epsilon_i^{-*}\epsilon_i^+\right)\sin\left(\frac{2\pi}{\lambda_0}n_i\delta_i\right)\right] I_0, \end{aligned} \tag{3.15}$$

were $I_0 \equiv \frac{n_0}{2\mu_0 c}\left|E^{\text{inc}}\right|^2$ is the incident power per unit surface. In the same notations, the reflected and the transmitted power densities w_{ref} and w_{tr} are, respectively:

$$w_{\text{ref}} = \left|\epsilon^{\text{ref}}\right|^2 I_0 \quad \text{and} \quad w_{\text{tr}} = \frac{n_{\text{tr}}}{n_0}\left|\epsilon^{\text{tr}}\right|^2 I_0. \tag{3.16}$$

3.2.2 Energy balance and equation of motion

Here we give a proof of the equation of energy balance Eq.3.3 and of the equation of motion Eq.3.4.

Let us first consider, for a unit mass of the material, two states i and f, characterized by the values of the phase field ϕ and $\phi + d\phi$, with pressure P and $P + dP$, and volume V and $V + dV$. We want to evaluate the heat dQ released to the unit mass in the transformation from i to f. The two liquid and solid phases, of masses ϕ and $1 - \phi$ respectively, perform a transformation, exchanging a heat quantity per unit mass given by the second TdS equation:

$$dQ_{S,L} = c_{S,L}dT - T\frac{\beta_{S,L}}{\rho_{S,L}}dP. \tag{3.17}$$

An infinitesimal variation $d\phi$ of the phase field, on the other hand, involves a heat absorption $\lambda d\phi$. Thus, the heat exchanged in the transformation $i - f$ is

$$dQ = c_\phi dT - T\left(\frac{\beta}{\rho}\right)_\phi dP + \lambda d\phi, \tag{3.18}$$

remembering the notation $f_\phi = (1-\phi) f_S + \phi f_L$. From equation 3.18, taking into account the three channels of heat release to the material (heat conduction, direct radiation heating of the liquid phase, plasma heat relaxation), equation 3.3 follows straightforwardly. It has to be noted that in the case of a mono-phase layer, posing $\phi = 0$ or $\phi = 1$ and $d\phi = 0$, Eq.3.18 follows immediately from the TdS equation.

The equation of motion of the system derives from the Newton law applied to the displacement field $r(x)$:

$$\rho_0 \frac{\partial^2 r}{\partial t^2} = -\frac{\partial P}{\partial x}, \tag{3.19}$$

performing a space derivative at both sides of Eq.3.19 and considering that the time derivative of the divergence of the displacement field r equals that of the product $\rho_0 \times v$, where $v = 1/\rho$ is the specific volume of the material at rest at room temperature:

$$\frac{\partial^2 v}{\partial t^2} = -\frac{1}{\rho_0^2}\frac{\partial^2 P}{\partial x^2}. \tag{3.20}$$

Let us consider first a mixed phase state for whom $v = v(P,\phi)$. An infinitesimal variation dv of the specific volume is

$$dv = \left(\frac{\partial v}{\partial P}\right) dP + \left(\frac{\partial v}{\partial \phi}\right) d\phi. \tag{3.21}$$

The partial derivatives of Eq.3.21 are readily calculated taking into account that the specific volume at a given pressure is given by (see also Fig.3.2, left)

$$v(P,\phi) = v_S(P)(1-\phi) + v_L(P)\phi, \tag{3.22}$$

where $v_{S,L}(P)$ is the specific volume of the saturated solid or liquid as function of the pressure. Consequently:

$$\left(\frac{\partial v}{\partial \phi}\right) = v_L - v_S \equiv \frac{1}{\rho_L} - \frac{1}{\rho_S} \quad \text{and} \quad \left(\frac{\partial v}{\partial P}\right) = \left(\frac{dv_S}{dP}\right)(1-\phi) + \left(\frac{dv_L}{dP}\right)\phi. \tag{3.23}$$

Now, the total derivative of $v_{S,L}(P)$ (volume of saturated solid and liquid), can be expressed in term of the equation of state of the solid and the liquid phase $v_{S,L}(P,T)$ in this way (see also Fig.3.2, right):

$$\left(\frac{dv_{S,L}}{dP}\right) = \left(\frac{\partial v_{S,L}}{\partial P}\right)_T + \left(\frac{\partial v_{S,L}}{\partial T}\right)_P \left(\frac{dT}{dP}\right)_{\text{fus.}} = -\frac{1}{\rho_{S,L} B_{S,L}} + \frac{\alpha_{S,L}}{\rho_{S,L}}\left(\frac{dT}{dP}\right)_{\text{fus.}} \tag{3.24}$$

By substitution of Eq.3.23 and 3.24 in Eq.3.21, rememebering the notation $f_\phi = f_S(1-\phi) + f_L\phi$:

$$dv = -\left(\frac{1}{\rho B}\right)_\phi dP + \left(\frac{\alpha}{\rho}\right)_\phi dT + \left(\frac{1}{\rho_L} - \frac{1}{\rho_S}\right) d\phi. \tag{3.25}$$

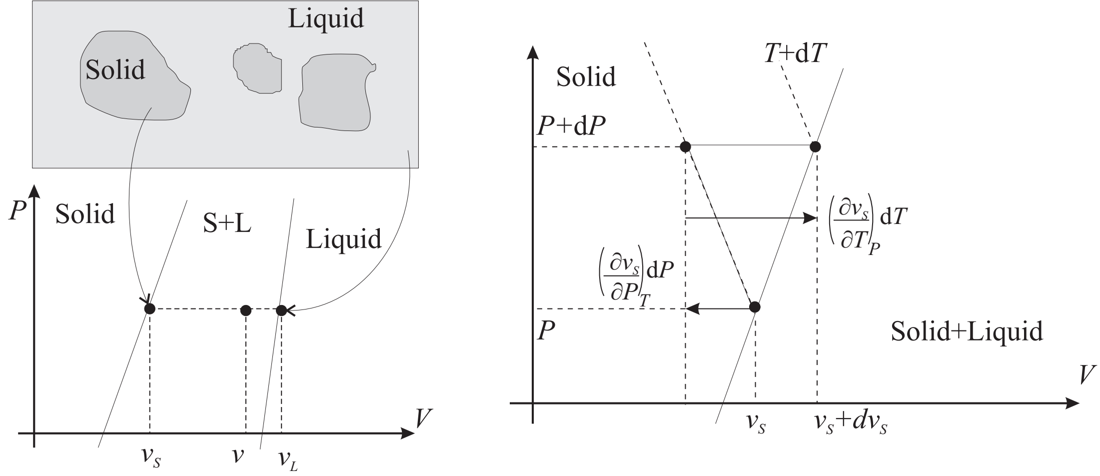

Figure 3.2: (left) Schematics of the volumes involved in a multi-phase layer. (right) Volume variations of the solid phase along the saturated solid curve.

From Eq.3.25, by a further differentiation and substitution in Eq.3.20, if we can neglect the variations of the coefficients of the differentials in Eq.3.25, we obtain Eq.3.4. If the coefficients cannot be neglected we have a more complicated equation wich is not linear in the first time derivatives. Nevertheless, the nonlinear terms do not involve prohibitive complications in the numerical equation (Eq.3.61) that solves the system. Also in this case, as for the energy balance equation, if we pose $\phi = 0$ or $\phi = 1$ and $d\phi = 0$ we obtain from Eq.3.4 an equation which is valid for the mono-phase layers.

3.2.3 Physical parameters

In the following, we report the expressions for the physical parameters which were utilized in the simulations. For the solid phase of silicon we mainly adopted the expressions found in two fundamental works of Lietoila and Gibbons[52] and Agassi[53] and to the references cited in their works. The intrinsic refraction index and extinction coefficient $n_{(0)S}$ and $k_{(0)S}$ of the solid phase of silicon, at different temperatures T and wavelengths λ, are interpolated by the results in ref.[54], by the functions

$$n_{(0)S} = a_\lambda (T - 273) + b_\lambda \quad \text{and} \quad k_{(0)S} = c_\lambda (T - 273)^2 + d_\lambda (T - 273) + e_\lambda; \quad (3.26)$$

The values of the constants, are given in Tab.3.1 for the wavelengths under consideration. The optical constants $n_{(0)L}$ and $k_{(0)L}$ of the liquid phase has been extracted from ref.[55], which gives, at the wavelengths of 355 and 532 nm, the values also reported in Tab.3.1.

Table 3.1: Values of the coefficients in Eqs. 3.26, and optical constants for liquid silicon, at the wavelengths under consideration (Kelvin degree unit for temperature)

λ	c_λ	a_λ / d_λ	b_λ / e_λ	$n_{(0)L}$ / $k_{(0)L}$
355 nm		-8.6×10^{-4}	5.62	2.13
	6.8×10^{-7}	-5.61×10^{-4}	2.97	4.31
532 nm		-5.18×10^{-4}	4.13	2.92
	2.41×10^{-7}	8.31×10^{-5}	0.085	4.99

Table 3.2: Values of the coefficients in Eqs. 3.35, 3.37, 3.40, in cgs units for mechanical and calorimetric units, kelvin degrees for temperature.

	ρ_0 / B_0	r	α_0 / α_1	T^*	a_1 / a_2 / a_3	θ_1 / θ_2
Diamond	3.51	3.5	-10^{-6}	450	1.796×10^7	1238
	4.415×10^{12}		1.8×10^{-5}		5.42×10^6	3390
					0	
Liquid carbon	3.04	2	-10^{-6}	450	2.424×10^7	1400
	3.378×10^{12}		2.4×10^{-5}		0	
					0	
Solid silicon	2.32	3	1.63×10^{-6}	212	6.22×10^6	630
	9.9×10^{11}		1.18×10^{-5}		2.73×10^6	166
					5.77×10^{-5}	
Liquid silicon	2.64	2	-8.35×10^{-6}	1300	1.07×10^7	100
	3.7×10^{11}		5.84×10^{-5}		0	
					0	

The ambipolar diffusivity depends both on lattice and plasma temperatures. We follow ref.[53] and write:

$$D_a(T,\theta) = 2k_B\theta\mu_a \quad \text{with}$$
$$\mu_a = \frac{\mu_n(T)\,\mu_p(T)}{\mu_n(T)+\mu_p(T)} \quad \text{and} \quad \theta = \frac{E}{3nk_B}. \tag{3.27}$$

Here, μ_n and μ_p are electron and hole mobility, respectively, which depends on lattice temperature as reported in ref[52]:

$$\mu_n = 1350\,(T/300)^{-2.4} \quad \mu_p = 480\,(T/300)^{-2.5} \quad \text{in units} \quad \mathrm{cm}^2/(\mathrm{Vs}). \tag{3.28}$$

For the band-gap width we adopted the expression proposed by O'Donnell and

Chen[56]:

$$E_g\left(T\right) = E_g\left(0\right) + E_{ph} S \left(\coth \frac{E_{ph}}{k_B T} - 1\right), \tag{3.29}$$

were E_{ph} is an average phonon energy (25.5 meV for silicon and 94 meV for diamond), and S is a coupling constant chosen in such way to fit experimental profiles (1.49 for silicon and 2.31 for diamond). The equilibrium plasma density in silicon, n_0, is[53]

$$n_0\left(T, \theta\right) = 5 \times 10^{15} \left(\frac{\theta}{\mathrm{K}}\right)^{1.5} \exp\left(-\frac{E_g\left(T\right)}{2 k_B \theta}\right) \mathrm{cm}^{-3}. \tag{3.30}$$

The Auger recombination time, for plasma densities not exceeding about 6.5×10^{20} cm^{-3} is given by[53, 52]

$$\tau_A = \frac{2.5 \times 10^{30}}{n^2} \mathrm{cm}^{-6}\mathrm{s}, \tag{3.31}$$

exceeding this value of charge density, screening effects limits it to not less than 6 ps. The electron-phonon relaxation time τ_{e-ph} has been assumed to be [50]

$$\tau_{e-ph} = 240 \times \left(1 + \left(\frac{n}{6 \times 10^{20} \mathrm{cm}^{-3}}\right)^2\right) \mathrm{fs}. \tag{3.32}$$

The temperature dependence of thermal conductivity of solid silicon and diamond was fitted to the data of ref.[57] and ref.[58], respectively, with an expression of the type

$$k_{th} / \left(\mathrm{Wcm}^{-1}\mathrm{K}^{-1}\right) = \exp\left(\sum_n k_n \ln^n \left(T/\mathrm{K}\right)\right), \tag{3.33}$$

for which the values of the coefficients are reported in Tab.3.4. For liquid silicon we adopted the value $k = 0.9$ $\mathrm{Wcm}^{-1}\mathrm{K}^{-1}$ as reported by ref.[59] Plasma thermal conductivity, following ref.[53], is

$$k_e = \left[-5.55 \times 10^{-3} + 7.75 \times 10^{-5} \left(\theta/\mathrm{K}\right)\right] \mathrm{cm}^2\mathrm{s}^{-1}. \tag{3.34}$$

Bulk modulus, expansion coefficient, specific and latent fusion heats at a generic pressure and temperature, are bounded by the equation of state and the thermodynamic functions of silicon and diamond. These quantities are comprehensively taken into account in the following subsection.

3.2.4 Equations of state and thermodynamic functions

Since both materials, diamond and silicon, are stressed to condition of pressure and temperature very far from ordinary ones, simple analytical expressions for the

equations of state for silicon (liquid and solid) and for diamond are requested, extrapolating the data available only for limited areas of the temperature-pressure domain. These expressions will be also useful in the determination of the thermodynamic functions of the material, in order to determine fusion curves and latent heats. For the equations of state and the thermodynamic functions of carbon the model of Fried and Howard[60] has been adopted. For silicon, I adopted the same or similar expressions, fitting the experimental data in refs.[61, 59, 62, 63].

The dependence of the density of the materials involved, both in solid and liquid phases, on temperature and pressure is expressed as

$$\rho = \rho_0 \times \eta (P,T) \quad \text{with} \quad \eta (P,T) = \left(r\frac{P}{B_0} + f(T) \right)^{1/r} \quad \text{and} \quad f(T) = e^{-r(g(T)-g(T_0))}; \tag{3.35}$$

where B_0 and ρ_0 are the bulk modulus and the density at standard temperature (T_0) and pressure (P_0), r is a constant dependent on the phase under consideration (see Tab. 3.2), and $g(T)$ is a function chosen in such way to reproduce the thermal expansion of the material at standard pressure. The expression of the thermal expansion coefficient, from expression 3.35, is found to be

$$\alpha \equiv -\frac{1}{\rho}\left(\frac{\partial \rho}{\partial T}\right)_P = g'(T)\frac{f(T)}{r\frac{P}{B_0} + f(T)}. \tag{3.36}$$

If $P << B_0$ the fraction multiplying $g'(T)$ approaches the unit value, thus it will be sufficient, at standard pressure, to adopt an expression for $g'(T)$fitting the thermal expansion coefficient. This can be done by means of an expression of kind

$$g'(T) = \alpha_0 + \alpha_1 \left(1 - e^{-T/T^*}\right)^2 \quad \text{that is} \tag{3.37}$$

$$g(T) = \alpha_0 T + \alpha_1 \left[T - \frac{T^*}{2}\left(e^{-T/T^*} - 2\right)^2 \right]. \tag{3.38}$$

The values of the parameters T^*, α_0 and α_1 for diamond phases has been found in [60], for solid and liquid silicon I have fitted, with expression 3.37, the data of ref.[35, 62]. All these parameters are reported in Tab.3.2. The equation of state serves also to calculate the bulk modulus B as

$$B = \frac{\rho}{\left(\frac{\partial \rho}{\partial P}\right)_T} = rP + B_0 f(T). \tag{3.39}$$

The thermodynamical function can be evaluated on the basis both of the equation of state, and of the specific heat at constant (and standard) pressure C_p^0, evaluated as a sum of two Einstein oscillators and a linear term:

$$C_p^0 = a_1 E(\theta_1/T) + a_2 E(\theta_2/T) + a_3 T \quad \text{with}$$
$$E(x) = x^2 e^x / (e^x - 1)^2. \tag{3.40}$$

For the carbon phases the values of a_i and θ_i was taken by ref.[60], while for solid silicon they was evaluated by fitting the data of ref.[61]. The value of C_p^0 adopted for liquid silicon was constant and equal to 1.1 J/(g×K), as reported in ref.[59]. Now, the Gibbs free energy $G(P,T)$ per unit mass can be written as

$$\begin{aligned} G(P,T) = \quad & G(P_0,T) + \int_{P_0}^{P} \frac{dP}{\rho} = \\ & G(P_0,T) + \frac{B_0}{\rho_0 (r-1)} \left(\eta (P,T)^{r-1} - \eta (P_0,T)^{r-1} \right), \end{aligned} \tag{3.41}$$

due to the fact that, at constant temperature, the differential of G is given by $dG = vdP = dP/\rho$. The Gibbs free energy at the pressure P_0 is given by $G(P_0,T) = H(P_0,T) - TS(P_0,T)$, with

$$\begin{aligned} H(P_0,T) = \quad & H(P_0,T_0) + \int_{T_0}^{T} C_p^0(T)\, dT = \\ & H(P_0,T_0) + \sum_{i=1}^{2} a_i \theta_i \left[\frac{1}{e^{\frac{\theta_i}{T}} - 1} \right]_{T_0}^{T} + a_3 \left(T^2 - T_0^2 \right)/2 \quad \text{and} \end{aligned} \tag{3.42}$$

$$\begin{aligned} S(P_0,T) = \quad & S(P_0,T_0) + \int_{T_0}^{T} \frac{C_p^0(T)}{T} dT = \\ & S(P_0,T_0) + \sum_{i=1}^{2} a_i \left[\frac{x}{e^{\frac{\theta_i}{T}} - 1} - \ln \left(1 - e^{\frac{\theta_i}{T}} \right) \right]_{T_0}^{T} + a_3 (T - T_0). \end{aligned} \tag{3.43}$$

Once determined the Gibbs free energy, the specific heat C_p is simpy evaluated by

$$\begin{aligned} C_p(P,T) = \quad & -T \left(\frac{\partial^2 G}{\partial T^2} \right)_P = \\ & C_p^0(T) + \frac{B_0 T f'(T)^2}{\rho_0 r^2} \left(\eta (P,T)^{-r-1} - \eta (P_0,T)^{-r-1} \right) - \\ & \frac{B_0 T f''(T)^2}{\rho_0 r} \left(\eta (P,T)^{-1} - \eta (P_0,T)^{-1} \right) \end{aligned} \tag{3.44}$$

The analytical expressions for the Gibbs free energy of each phase previously obtained allows the determination of the fusion curves, along which the Gibbs functions of the liquid and the solid phase have a same value. I considered the equilibrium between diamond and liquid carbon phases as the limit over which, for the very fast transitions which we are interested in, graphitization occurs. For slower transitions, within hundreds seconds as order of magnitude, graphitization can hold also at relatively lower temperatures, beginning with seeds corresponding to free surfaces or other structural defects. In a pulsed laser experiment the situation is very different,

Table 3.3: Values of the coefficients in Eq. 3.45, in cgs units for mechanical and calorimetric units, kelvin degrees for temperature.

	T_0	a	T_1	P_0
Carbon	4250	1.83×10^{-9}	15700	3.79×10^{12}
Silicon	1680	9.07×10^{-9}	293	5.77×10^{10}

Table 3.4: Values of the coefficients in Eq. 3.33, in cgs units for mechanical and calorimetric units, kelvin degrees for temperature.

	k_0	k_1	k_2	k_3
Diamond $T < 1200$	84.3	-35.8	5.35	-0.274
Diamond $T \geq 1200$	10.8	-1.32		
Solid Si	14.1	-3.15	0.138	

because graphitization has to occur in a few picoseconds. In this case, I consider that graphitization doesn't occur until diamond "would" loose its structural stability in favor of the liquid phase; at that point it ends up with finding a structural equilibrium with a Gibbs free energy lower than both diamond and liquid carbon, so that it graphitizes over the whole volume over which the threshold has been passed. Since graphite has, at atmospheric pressure, a much lower density than diamond, it can be argued that a huge increase in pressure holds at this point, transferring the system in the proximity of the diamond-graphite-liquid triple point. At this point, every further heat release to the system results in carbon fusion and (presumably) carbon-silicon interdiffusion. It was found that, both for carbon and silicon, the equilibrium line between solid and liquid phase is well fitted by the sum of a linear and an exponential function, giving

$$T = T_0 - aP + T_1 \left(1 - \exp\left(-P/P_0\right)\right), \tag{3.45}$$

with the values of the parameters given in Tab.3.3. Particularly, the parameters of the state equation of silicon has been chosen in a way that the fusion curve fits the experimental points in ref.[63]. Finally, the fusion curve and the equation of state allow, via the Clapeyron equation, the determination of the latent heat of fusion:

$$\lambda = T \left(\frac{1}{\rho_L(P)} - \frac{1}{\rho_S(P)} \right) / \frac{dT}{dP} \tag{3.46}$$

3.3 Numerical implementation

A one-dimensional finite-element algorithm was employed with a spatio-temporal grid $\{(x_i, t_j)\}_{0 \leq i \leq N+1, 0 \leq j}$. Temporal integration step was $\tau = t_{j+1} - t_j$, and the

spatial matching $\delta_i = x_{i+1} - x_i$ was choosen in a way to describe in more detail the regions where the fields have highest gradients (tipically, near silicon-diamond interface). The values taken in every position x_i at the time t_j by each field $X(x,t)$ are represented by the components of the vector X^j, in a way that $X(x_i,t_j) = (X^j)_i$. The equations which rule the system have to be solved taking into account boundaries between solid, liquid and muli-phase zones. We define four diagonal matrices $\chi^{(1)}$, $\chi^{(2)}$, $\chi^{(3)}$ and $\chi^{(4)}$ whose elements are 1 if the corresponding i−th layer is in a mono-phase state, or it is on the melting curve, or at the triple point, or on the vapor curve, respectively, and 0 otherwise. With these notations, equations 3.3 to 3.8 can be translated in a finite difference formulation for which the diffusion equation Eq.3.3 follows a backwards Euler scheme, while the wave equation Eq.3.4 is solved with a forward Euler one. Since temporal derivatives of the fields T, P and ϕ are coupled by Eqs. 3.3 to 3.8, these equations have to be integrated simultaneously. According to this scheme, the fields at the time t_{j+1} are calculated as functions of those at time t_j and t_{j-1} inverting the following system:

$$\begin{pmatrix} \left(\mathbf{1}-\chi^{(3)}\right)\boldsymbol{A}+\mathbf{1} & \left(\chi^{(1)}+\chi^{(2)}\right)\boldsymbol{a} & \chi^{(2)}\boldsymbol{b} \\ \left(\chi^{(1)}+\chi^{(2)}\right)\boldsymbol{c} & \mathbf{1} & \chi^{(2)}\boldsymbol{d} \\ \chi^{(2)}\boldsymbol{e} & \chi^{(2)}\boldsymbol{f} & \mathbf{1}-\chi^{(2)} \end{pmatrix} \times \begin{pmatrix} T^{j+1} \\ P^{j+1} \\ \phi^{j+1} \end{pmatrix} = \begin{pmatrix} C_T^j \\ C_P^j \\ C_\phi^j \end{pmatrix}$$
$$(\mathbf{1}+\boldsymbol{C})\,n^{j+1} = C_n^j \quad \text{and} \quad (\mathbf{1}+\boldsymbol{D})\,E^{j+1} = C_E^j \qquad (3.47)$$

Where the column vectors C_X^j depends on the fields at the times t_j and t_{j-1} in the following way:

$$\begin{aligned} C_T^j = \;& T^j + \left(\mathbf{1}-\chi^{(3)}\right)\left(\boldsymbol{g}E^j + A_T^0 + W_T\right) + \left(\chi^{(1)}-\chi^{(2)}\right)\boldsymbol{a}P^j + \chi^{(2)}\boldsymbol{b}\phi^j, \\ C_P^j = \;& \left(\chi^{(1)}+\chi^{(2)}\right)\left[2\left(\boldsymbol{c}T^j + P^j + \chi^{(2)}\boldsymbol{d}\phi^j\right) - \left(\boldsymbol{c}T^{j-1} + P^{j-1} + \chi^{(2)}\boldsymbol{d}\phi^{j-1}\right)\right] + \\ & \left(\chi^{(1)}+\chi^{(2)}\right)\left[-\boldsymbol{B}P^j - B_P^0\right] + \left(\chi^{(3)}+\chi^{(4)}\right)P^j, \\ C_\phi^j = \;& \left(\mathbf{1}-\chi^{(2)}\right)\phi^j + \chi^{(2)}\left(\boldsymbol{e}T^j + \boldsymbol{f}P^j\right) + \chi^{(3)}\boldsymbol{b}^{-1}\left(\boldsymbol{g}E^j - \boldsymbol{A}T^j - A_T^0 + W_T\right), \\ C_n^j = \;& n^j + W_n \quad \text{and} \quad C_E^j = E^j + \boldsymbol{E}N^j + W_E + \boldsymbol{h}E_{gap}^j + \boldsymbol{l}E_{gap}^{j-1} \end{aligned} \qquad (3.48)$$

In Eq.3.48, lower case bold letters represent diagonal $N \times N$ matrices whose non-null components are:

$$\begin{aligned} & a_{ii} = -\left(\frac{\alpha}{\rho}\right)_\phi \frac{T_i}{c_\phi}, b_{ii} = \frac{\lambda}{c_\phi}, c_{ii} = -\frac{\left(\frac{\alpha}{rho}\right)_\phi}{\left(\frac{1}{\rho B}\right)_\phi}, d_{ii} = -\frac{\frac{1}{\rho_S} - \frac{1}{\rho_L}}{\left(\frac{1}{\rho B}\right)_\phi}, \\ & e_{ii} = \frac{1}{B_\phi}\left(\frac{dP}{dT}\right)_{fus.}, f_{ii} = -\frac{1}{B_\phi}, h_{ii} = -(1-\phi)\,\psi\frac{w}{h\nu}\tau + (n-n_0)\,q\left(\frac{\tau}{\tau_A}\right) - n, \\ & g_{ii} = \frac{a_{ii}}{3nK_B}, \qquad l_{ii} = n; \text{with} \quad q(x) = (1-\exp(-x)). \end{aligned} \qquad (3.49)$$

In Eq.3.49 functions and physical parameters calculated at time t_j in the point x_i. The factor $\frac{1}{B_\phi}$, where necessary, was introduced only for dimensional coherence. Higher case letters represent tri-diagonal matrices in the form

$$\boldsymbol{X} = \begin{pmatrix} x_1^0 & -x_1^+ & 0 & ... \\ -x_2^- & x_2^0 & -x_2^+ & ... \\ 0 & -x_3^- & x_3^0 & ... \\ ... & ... & ... & ... \end{pmatrix} \tag{3.50}$$

with

$$\begin{aligned} a_i^\pm &= \frac{\tau}{2}\left[\rho_{0i}c_{\phi i}\delta_i\left(\frac{\delta_i}{k_{\phi i}} + \frac{\delta_{i\pm1}}{k_{\phi i\pm1}}\right)\right]^{-1} \\ \text{and} \quad a_i^0 &= a_i^- + a_i^+ + \frac{3n_iK_B}{\rho_{0i}c_{\phi i}}q\left(\frac{\tau}{\tau_{el-ph}}\right); \end{aligned} \tag{3.51}$$

$$\begin{aligned} b_i^\pm &= \frac{\tau^2}{2}\left[\rho_{0i}^2\delta_i\left(\left(\frac{1}{\rho B}\right)_{\phi i}\delta_i + \left(\frac{1}{\rho B}\right)_{\phi i\pm1}\delta_{i\pm1}\right)\right]^{-1} \\ \text{and} \quad b_i^0 &= b_i^- + b_i^+; \end{aligned} \tag{3.52}$$

$$\begin{aligned} c_i^\pm &= \frac{\tau^2}{2}\left[\delta_i\left(\frac{\delta_i}{D_{ai}} + \frac{\delta_{i\pm1}}{D_{ai\pm1}}\right)\right]^{-1}, \\ \text{and} \quad c_i^0 &= c_i^- + c_i^+ + q\left(\frac{\tau}{\tau_A}\right); \end{aligned} \tag{3.53}$$

$$\begin{aligned} d_i^\pm &= \frac{\tau}{\frac{\delta_i}{2}\left(\frac{\delta_i}{k_{ei}} + \frac{\delta_{i\pm1}}{k_{ei\pm1}}\right)}\frac{1}{3k_Bn_{i\pm1}} \\ d_i^0 &= \frac{1}{3k_Bn_i}\sum_{l=\pm1}\frac{\tau}{\frac{\delta_i}{2}\left(\frac{\delta_i}{k_{ei}} + \frac{\delta_{i+l}}{k_{ei+l}}\right)} + q\left(\frac{\tau}{\tau_{el-ph}}\right) \end{aligned} \tag{3.54}$$

$$e_i^\pm = \frac{\tau}{\frac{\delta_i}{2}\left(\frac{\delta_i n^i}{D_{ai}E^i} + \frac{\delta_{i\pm1}n^{i\pm1}}{D_{ai\pm1}E^{i\pm1}}\right)} \quad \text{and} \quad e_i^0 = e_i^- + e_i^+ \tag{3.55}$$

The column vectors A_T^0 and B_P^0, in Eq.3.48, represent vectors whose components are all zero except the first one, respectively $a_0^- T_{room}$ and $b_0^- P_{external}$, and the last,

respectively $a_N^+ T_{room}$ and $b_N^+ P_{external}$. Each component of the column vectors W_X, finally, depends on the fields at each position x_i and time t_j in the following way:

$$W_{Ti} = \phi w, \quad W_{ni} = \psi \left(1 - \phi\right) \frac{w}{h\nu} \tau,$$
$$W_{Ei} = 3k_B n T q \left(\frac{\tau}{\tau_{el-ph}}\right) + \left(1 - \phi\right) w\tau. \tag{3.56}$$

The solution of the system 3.47, involving the inversion of a general $3N \times 3N$-matrix, can be reduced to the inversion of a tri-diagonal $N \times N$-matrix and to three cascade-substitutions involving only products and sums of $N \times N$-matrices. This substantial simplification is allowed by the application of a sort of Gauss triangulation method applied to the 3×3-matrix of system 3.47, whose elements are nine $N \times N$ matrices, eight of which are diagonal, and one tri-diagonal. If we adopt the convention to indicate with the capital Greek letter Λ the tri-diagonal matrix, and with small Greek letters the diagonal matrices, system 3.47 can be written in the most handy form

$$\begin{pmatrix} \Lambda & \alpha & \beta \\ \chi & 1 & \delta \\ \epsilon & \phi & \gamma \end{pmatrix} \times \begin{pmatrix} T^{j+1} \\ P^{j+1} \\ \phi^{j+1} \end{pmatrix} = \begin{pmatrix} C_T^j \\ C_P^j \\ C_\phi^j \end{pmatrix}. \tag{3.57}$$

In order to apply the triangulation method, the pivot element has to be invertible. Noting that $\beta + \gamma$ is an invertible diagonal matrix, it is convenient to sum the first and the third arrow and to reorder the therms of the system, obtaining:

$$\begin{pmatrix} \gamma + \beta & \phi + \alpha & \epsilon + \Lambda \\ \delta & 1 & \chi \\ \gamma & \phi & \epsilon \end{pmatrix} \times \begin{pmatrix} \phi^{j+1} \\ P^{j+1} \\ T^{j+1} \end{pmatrix} = \begin{pmatrix} C_\phi^j + C_T^j \\ C_P^j \\ C_\phi^j \end{pmatrix}. \tag{3.58}$$

At this point, multiplying the first row of the system by $-\delta$ and the second by $\gamma + \beta$, and then summing the results, we can eliminate the unknown ϕ^{j+1} in the second row. With an analogous procedure applied to the first and the third row, we obtain the subsystem involving only the two unknowns P^{j+1} and T^{j+1}:

$$\begin{pmatrix} (\gamma + \beta) - \delta\left(\phi + \alpha\right) & (\gamma + \beta)\chi - \delta\left(\epsilon + \Lambda\right) \\ \beta\phi - \alpha\gamma & (\gamma + \beta)\epsilon - \gamma\left(\epsilon + \Lambda\right) \end{pmatrix} \times \begin{pmatrix} P^{j+1} \\ T^{j+1} \end{pmatrix} = \tag{3.59}$$
$$\begin{pmatrix} (\gamma + \beta) C_P^j - \delta\left(C_\phi^j + C_T^j\right) \\ \beta C_\phi^j - \gamma C_T^j \end{pmatrix}.$$

We note that $(\gamma + \beta) - \delta\left(\phi + \alpha\right)$ is a diagonal invertible matrix, so that if we multiply the first row by $-\left(\beta\phi - \alpha\gamma\right)\left[(\gamma + \beta) - \delta\left(\phi + \alpha\right)\right]^{-1}$, and we sum the results to the

second row, we obtain the equation involving only the unknown T^{j+1}:

$$\begin{aligned}&\{[(\gamma+\beta)\,\epsilon-\gamma\,(\epsilon+\Lambda)]-(\beta\phi-\alpha\gamma)\,[(\gamma+\beta)-\delta\,(\phi+\alpha)]^{-1}\times\\&[(\gamma+\beta)\,\chi-\delta\,(\epsilon+\Lambda)]\}T^{j+1}=\\&\beta C_\phi^j-\gamma C_T^j-(\beta\phi-\alpha\gamma)\,[(\gamma+\beta)-\delta\,(\phi+\alpha)]^{-1}\left[(\gamma+\beta)\,C_P^j-\delta\left(C_\phi^j+C_T^j\right)\right].\end{aligned} \tag{3.60}$$

The matrix which multiplies T^{j+1} in Eq.3.61 is in a tri-diagonal form, its inversion permits to calculate T^{j+1}, and the successive substitutions in Eq.3.60 and in Eq.3.58, by inversion of the simple diagonal invertible matrices $(\gamma+\beta)-\delta\,(\phi+\alpha)$ and $\gamma+\beta$, allow the calculation of P^{j+1} and ϕ^{j+1}.

3.4 Results of calculations

The main issues addressed by our simulations were the determination of the energy density threshold for Silicon-Diamond adhesion as well as the thickness of the silicon layer damaged by the process, related to the maximum depth of the melting front. Both these quantities show a definite dependence on the laser wavelength and on the pulse width, parameters whose influence has to be investigated in order to optimize the bonding process. In our simulations we employed wavelengths of 533 and 355 nm, corresponding to the second harmonic and to the frequency mixing of the second and the third harmonic of a Nd:YAG laser, with pulse durations ranging from the typical picoseconds of the mode-locked to the nanoseconds of the Q-switched lasers. In order to obtain the dependence on time of quantities which could be important in the on-line monitoring of the process, also the reflectivity of the Silicon-Diamond interface was calculated during and after the pulse duration.

In figure 3.3 (left) typical temperature profiles are shown corresponding to the threshold of the fusion temperature of silicon and of carbon at the interface, for a pulse width of about 18 ps, at the wavelengths of 355 and 533nm. Due to the different penetration lengths, the energy densities necessary to reach the melting conditions are higher for the 533 nm radiation. For longer pulse widths the temperature profile is much wider due to heat diffusion (see the inset of Fig.3.3), and the penetration length of the radiation has a progressively minor role, such that the difference between energy thresholds at different wavelengths tends to vanish for very long pulse widths.

In figure 3.3 (right) the energy density thresholds for the melting of silicon and carbon at the silicon-diamond interface are shown, as functions of the pulse width, at the two wavelengths under consideration. Analytical fits of the numerically calculated points are also drawn, pointing out a diffusive behavior ($E \approx k \times \tau^{0.5}$) for very long pulse durations. At the wavelength of 355 nm, for instance, the energy

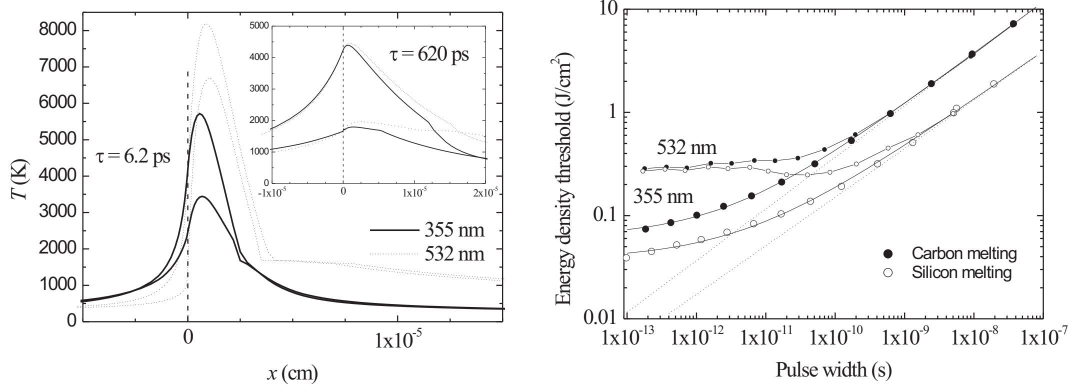

Figure 3.3: (Left) Temperature profiles correspondent to the reaching of the melting temperature either of carbon or of silicon at the silicon-diamond interface. Solid lines correspond to the wavelength of 355 nm, dotted ones to 533 nm. In the main panel, pulses of about 18 ps are considered, in the inset, profiles correspondent at pulses of about 640 ps are shown. (Right) Energy density thresholds for the melting of carbon (full circles) and of silicon (void circles) as functions of the pulse width at wavelengths of 355 nm (big circles) and 532 nm (small circles). Asymptotic behaviors for very long pulse durations are reported as dotted lines.

thresholds Q_{Si} and Q_{D} as functions of the pulse width τ are very well fitted by the expressions

$$Q_{\mathrm{Si}} = \left(0.037 + 7700 \times \left(\frac{\tau}{\mathrm{s}}\right)^{0.47}\right) \frac{\mathrm{J}}{\mathrm{cm}^2}$$
$$Q_{\mathrm{D}} = \left(0.062 + 38000 \times \left(\frac{\tau}{\mathrm{s}}\right)^{0.50}\right) \frac{\mathrm{J}}{\mathrm{cm}^2} \quad (3.61)$$

This point deserves a more careful consideration. If we suppose to release a certain amount of energy at a constant rate to an infinitely thin layer at the interface between two materials in close contact, it is a mere analytical exercise to verify that the energy necessary to reach a given temperature is proportional to the square root of the pulse duration. This is obviously a very poor approximation of the real system, but the exponent very close to 0.5 in the expressions 3.61 indicate that these expressions catch the physical essence of the phenomena involved, being the constants added to the diffusive terms due to the near-interface effects related altogether to radiation penetration, plasma diffusion and material melting. The behavior of the threshold values at 532 nm, for short pulse widths, is more complicated, as seen in Fig. 3.4, due to a sharper decrement of the penetration length during melting, which decreases

of a factor about 60.

In section 3.5, I shows that all the bonding experiments that we performed up to now are compatible with the thresholds found for the melting of carbon.

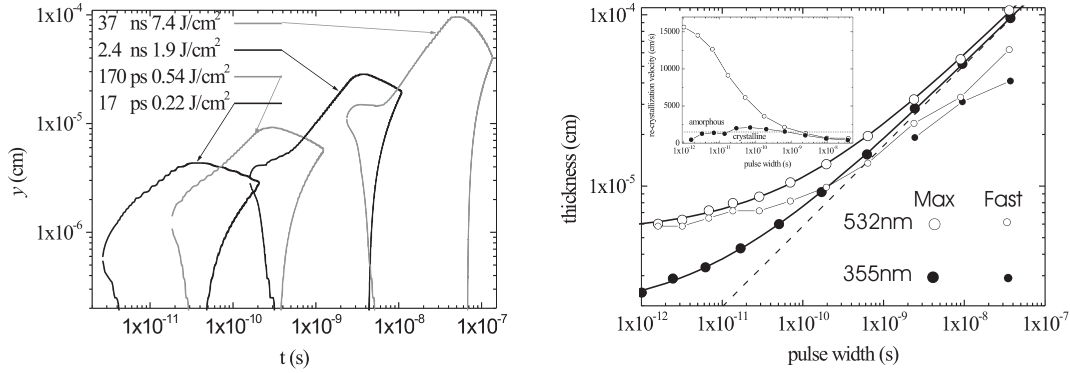

Figure 3.4: (Left) Diagrams of the motion of the melting-recrystallization fronts in silicon for several pulse widths, at the wavelength of 355nm and at the energies which are just enough to obtain carbon fusion. The arrows indicate the instants of the pulse-end. (Right) Thickness of the damaged layer as function of the pulse width, at the energy threshold for the carbon fusion. Full circles: 355 nm wavelength, empty circles: 532 nm. Big circles: maximum penetration depth of the melting front, small circles: maximum penetration of the fast re-crystallization front. Inset: velocity of the slow re-crystallization front, the boundary between amorphous and crystalline re-crystallization is evidenced.

Figure 3.4 (left) gives information about another issue addressed by our simulations: the positions of the boundaries between melted and solid phase in silicon during and after the pulse duration, taken as the depths z for which the phase field ϕ has the value $\phi(z) = 0.5$. The melting front positions are shown for different pulse widths, at 355 nm wavelength and energy densities which are just enough to reach the melting conditions of carbon. Note that after the pulse two opposite-propagating re-crystallization fronts are present: a fast one from diamond and a slow one from the silicon bulk. The maximum penetration depth of the melting front (e.g. point A in Fig.3.4 (left)), for each pulse width, gives the correspondent minimum thickness of the layer damaged by the process. In fact, during the cooling of melted silicon we can assume that re-crystallization takes place in an amorphous form, as confirmed by the detection in the bonded SOD samples of an amorphous silicon layer of the order of 100 nm [45]. As a matter of fact, for re-crystallization speeds below about 15 m/s, solidification in mono-crystalline form is assessed[44], that is, if the

re-crystallization front from the silicon side propagates slowly enough, the thickness of the damaged layer could be limited to the maximum propagation length of the fast front from the diamond side (e.g. point B in Fig.3.4 (left)). We verified that, as shown in the inset of Fig. 3.4 (right), such a slow propagation velocity, requiring low thermal gradients, is quite common at all pulse durations for the 532 nm wavelength, but holds only for the longest pulse widths at 355nm wavelengths. Figure 3.4 (right) shows the maximum penetration depth of the melting front at different pulse widths (at the energy threshold for the carbon fusion), for both the wavelengths under consideration, and also the maximum penetration depth of the fast-recrystallization front, for the pulse widths for which the re-crystallization speed does not exceed about 15 m/s.

In Figure 3.4 (right), the minimum thickness of the damaged layer as a function of the pulse width is reported for the two wavelengths under consideration. Also in this case, a diffusive law as in Eqs.3.61 seems to take place, namely:

$$\begin{aligned} w_{355\ \mathrm{nm}} &= \left(18 + 3 \times 10^6 \times \left(\frac{\tau}{\mathrm{s}}\right)^{0.47}\right) \mathrm{nm} \\ w_{532\ \mathrm{nm}} &= \left(54 + 3.5 \times 10^6 \times \left(\frac{\tau}{\mathrm{s}}\right)^{0.48}\right) \mathrm{nm}.. \end{aligned} \tag{3.62}$$

In order to optimize the bonding process, the constants lengths (18 and 54 nm for 355 and 533 nm of wavelength, respectively) are of great significance: they are the minimum thickness which can be achieved for the damaged layer at a specific wavelength, with the shortest pulse widths, and are somehow related to the average penetration length of the radiation during the whole pulse duration.

The model can give predictions not only about off-line measurable quantities like energy thresholds and damaged layer thicknesses, but also about some parameters which can suitably monitor the bonding process on-line. For example, the reflectivity of the interface layer can be experimentally followed by means of a pump-and-probe scheme exploiting part of the pulse power in a delay stage[64]. Thus, we traced the reflectivity of the interface at the same wavelength of the heating pulse during and after the process until it reaches its equilibrium value. In doing so, we assumed that the optical characteristics of the re-solidification layer are the same of the mono-crystal, this is only a rough approximation, a more realistic simulation should require a thorough optical characterization of the amorphized layer left by the re-solidification process. Figure 3.5 shows the reflectivity profiles for a pulse duration of about 18 ps at the two wavelengths of interest, for pulses having just the power sufficient for the melting of carbon. The shape of the reflectivity pulses during the heating phase depends both on plasma effects (particularly the minimum before silicon melting) and on a refraction index variation due to the melting itself. During cooling, the propagation of the re-crystallization fronts determine also an

interference pattern which could be particularly evident for very long pulse widths (see the inset of Fig. 3.5).

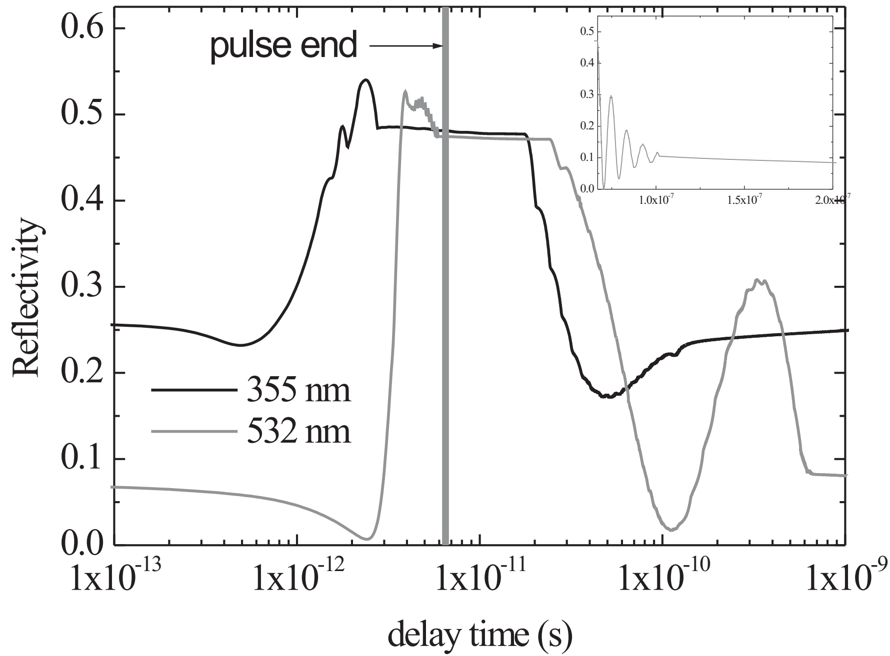

Figure 3.5: Reflectivity profiles for 6.5 ps pulses with energies at the carbon-melting thresholds, during and after the pulse duration. In the inset: the tail of the 36 ns-pulse reflectivity profile at 532 nm, showing a clear interference pattern due to the propagation of the re-crystallization front

3.5 Comparison with experiments

The principal feature for which a comparison is attainable between experimental data and simulation results is the energy density threshold for carbon, related to the effectiveness of post processing adhesion. As seen in chapter 2, the maximum $\mathscr{E}_M$ and the minimum energy density per pulse $\mathscr{E}_m$ which impinges on the silicon-diamond interface can be simply calculated by the overall energy per pulse E_0, by the reduction factor ρ of the optics and by the pitch R of the irradiation matrix by

means of the relations:

$$\mathcal{E}_M = \frac{E_0}{2\pi\rho^2\sigma_x\sigma_y\int_0^\infty e^{-z^\alpha}dz} \quad \text{and} \quad \mathcal{E}_m = \mathcal{E}_M e^{-\left[R^2\left(\frac{1}{8\rho^2\sigma_x^2}+\frac{1}{8\rho^2\sigma_y^2}\right)\right]^\alpha} \tag{3.63}$$

with $\sigma_x = 2.3$ mm, $\sigma_y = 2.0$ mm, $\alpha = 1.51$ and $\int_0^\infty e^{-z^\alpha}dz = 0.902$. So we can have three different situations, depending on the position of the threshold $\mathcal{E}_{thr.}$ with respect to the interval $[\mathcal{E}_m, \mathcal{E}_M]$. If $\mathcal{E}_{thr.} < \mathcal{E}_m < \mathcal{E}_M$, the two materials should adhere on the entire surface extension, if $\mathcal{E}_m < \mathcal{E}_{thr.} < \mathcal{E}_M$, we have adhesion only on the central part of each spot, while if $\mathcal{E}_m < \mathcal{E}_M < \mathcal{E}_{thr.}$ lack of adhesion is expected everywhere on the sample surface. In figure 3.6 a survey of the positions of the intervals $[\mathcal{E}_m, \mathcal{E}_M]$ is given with respect to the energy threshold, along with the indication of the outcome of the related bonding experiment in term of partial/total/null adhesion. Some images of the diamond-silicon interface taken by the diamond side are shown too. The totality of the experiments support the theoretical predictions, confirming the well-foundness of our analysis of the phenomena involved in silicon-diamond laser bonding.

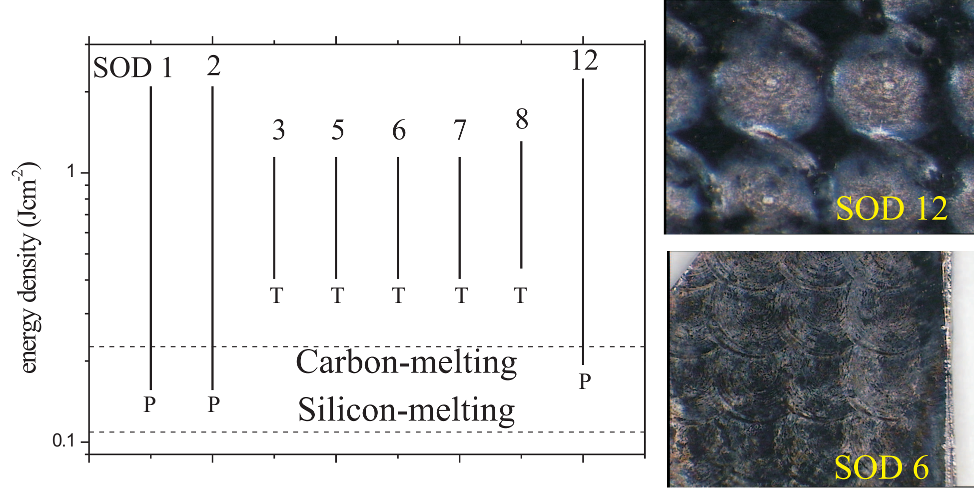

Figure 3.6: (left) Position of the calculated thresholds for carbon and silicon melting, compared with the ranges of energy density obtained in the experiments from SOD1 to SOD12, along with the indication of the partial (P) or total (T) adhesion obtained. (right) details of the SOD6 and SOD12 interfaces, observed from the diamond side.

The other parameter on which our model can make predictions is the minimum thickness of the damaged layer in silicon, exactly correspondent to the carbon melting-threshold. Since the model doesn't make predictions for energy densities

much above the threshold and for the laser pulses following the first ones, it is only expectable that this value is lower than all the measured interface layer thicknesses. For comparison, the model gives a minimum thickness of about 50 nm, while all measurements obtained with TEM analysis, Raman and FTIR spectroscopy give results mainly between 85 and 150 nm, fairly in agreement with the analysis.

Although shorter pulse durations and wavelengths would be desirable in order to obtain thinner diamond-silicon interfaces, the analysis shows that it is possible to fully exploit the potentialities of the present laser source by lowering the overall pulse energy E_0 and decreasing the pitch R between welded points, in order to get near the energy density threshold and to reduce the spread in energy density. To this aim, a fully automated irradiation system is presently under production, which should allow to irradiate the surface almost continuously with a micrometric resolution. In this way, we expect to greatly increase the uniformity of the interface thickness and to reduce it, on the average, of a factor two.

Chapter 4

Pre-bonding silicon-diamond elastic contact

In chapter 2 we observed that, in silicon-on-diamond prepared by pulsed laser irradiation, the quality of the interface can deteriorate for several reasons: the adherence of silicon and diamond can be defective on surfaces several tens or hundreds microns wide, but also in macroscopically adherent samples lenticular voids of some tens of nanometers in diameter have been evidenced by transmission electron microscopy. In chapter 3 I showed how the irradiation conditions strongly influences the post-processing adhesion on the lengthscale of the beam-intensity variations. Uni-axial pre-bonding compression is also important to define conditions of adhesion of the two materials for several reasons. In order to obtain adhesion it is not enough to reach a sufficient temperature of the melted silicon, because it is also essential that diamond could be heated by contact with the fused phase of silicon. This is the only way for melting carbon and forming a silicon-carbon interface. As a consequence, a close contact between melted silicon and diamond surface before irradiation has to be assured.

Now, it is well known that the effective contact even between well polished surfaces is limited, in absence of a strong compressive stress of the two surfaces, only to a very small area. Uni-axial compression can assist post-irradiation adhesion of silicon and diamond in two ways.

First, the rough diamond surface can be plunged in the melted layer in a way to put the whole surface of diamond in contact with liquid silicon. As a matter of fact, laser assisted direct imprint technique [65] allows in this way to emboss a transparent mould into an eccimer laser-melted silicon layer, in order to obtain direct imprinting of nanostructures in silicon. This technique requires that silicon remains in the melted phase for the whole time necessary for the “plunging” of the

diamond profile. This can be evaluated as the time necessary to relax the stress of a layer which is compressed of an amount that equals about the surfaces roughness. This time is of the order of the layer thickness divided by the velocity of sound. Now, if diamond peak-valley roughness is about 20 nm, and the uni-axial stress about 100 MPa, the layer thickness to be relaxed in silicon is about 20 μm (bulk modulus is about 100 GPa) thus the time required for plunging is more than 2 ns (sound velocity in silicon is about 8400 m/s), one order of magnitude exceeding the expected silicon-melting time with a tipical picosecond laser pulse (see chapter 3).

There is another way for uni-axial compression to enhance post process adhesion, that is to put in contact before laser irradiation as much of the surfaces as possible, by elastic deformation of the solid silicon and diamond profiles.

Pre-bonding compression of silicon and diamond samples can be related also to the formation of the nanometric lenticular voids in the silicon-diamond interface observed by TEM. Since the lifetime of the melted layer is too short to plunge the diamond profile in the silicon melt, it is very likely that the voids existing between silicon and diamond before irradiation remains substantially unchanged in volume during the bonding process. Thus the observed voids in the interface are possibly related, at least in principle, with pre-bonding compression.

From the considerations above, the study of the pre-bonding adhesion cannot set aside the detailed observation of the surfaces profile. Obviously, contact between two rough solid surfaces with a given profile can be defined only in dependence on the resolution with which the profile has been observed. An apparently smooth surface in the micrometric range could be very rough at the atomic scale, so that the effective atomic rate of contact is quite small. For the observation of the diamond and silicon samples at our disposition, we employed a white-light interferometric profilometer operating with a phase shift method, which is able to draw two-dimensional maps with a sub-micrometric lateral and a nanometric vertical resolution. For the application to whom we are interested in, which involve, at least in a first stage of the research, a not too small integration scale of the electronics, this resolution seems to be sufficient.

For our bonding experiments, we dispose of three different batches of diamond samples, on which I performed a theoretical analysis of the deformation of the surfaces under a given uni-axial pressure. By this analysis, an answer to the following kind of questions can be obtained:

- for given surfaces profiles, how much do we have to press together a diamond and a silicon sample in order to obtain, at the sub-micrometric scale, pre-bonding adhesionon on, say, 95% of the *area* of the whole surface?
- for given surface profiles and at a given pressure, which is the overall *volume*

of the voids remaining between silicon and diamond?

The problem of determining the rate of effective contact between two rough surfaces under uni-axial stress is addressed in contact mechanics, with important implications in many fields (contact resistivity, heat transfer and slide friction between solids in close contact), depend on the answear to the questions mentioned above, which has also a major influence on the adhesive force between two solid blocks in direct contact. The problem was treated first by Hertz in 1882[66] for two curved surfaces of different radius. The names of Bowden and Tabor [67] and Archard [68] are linked to the problem of contact between rough surfaces and to the first clarification of the Coulomb empiric law of the proportionality between normal stress and sliding friction forces, at the middle of XX century. The field has been in constant development till the last decade, with the fundamental works of Persson [36, 69, 70], facing the problem of how the true contact surface in rough materials is generally proportional to the normal force, while the parameters of individual micro-contacts (i.e. pressure, size of the micro-contact) are only weakly dependent upon the load. Persson's theory, at present the most advanced theoretical investigation in the field, aspires to describe contact conditions under the whole range of uni-axial stresses, from zero to infinity. Nevertheless, letting apart what I find somewhat ambiguous in its mathematical framework (see appendix A), the theory limits itself, for its very nature, to a statistical description of the contact mechanics between rough surfaces. On the contrary, I developed a theory of contact between two surfaces with a given profile which has a more limited field of application, being valid only in the high pressures, almost-complete contact limit, but gives detailed information about where and how large are the non-contact areas.

In order to compare the predictions of the model with the experiments, we are implementing a set-up for the measurement of the shift of the silicon raman line at 521 cm^{-1} due to the distortion of the crystal lattice at the silicon-diamond contact points. At the moment, preliminary results are available which are comparable with the answer to another question addressable by the model:

- for given surface profiles and at a given pressure, which is the *local pressure* applied, point by point, on silicon at the interface?

In section 4.1 data collection on the sample profilometry is presented. In section 4.2 a theory of the elastic deformation of rough solids in close contact is developed for the almost-complete contact case we are interested in. In section 4.3 predictions are made on the basis of the experimental profiles about contact ratios, overall void volume and local stress at the silicon-diamond interface, for the three batches of samples under consideration. In section 4.4 the Raman measurement of the local stress is described and the available preliminary results are presented and

compared with the theory. Finally, in appendix A, a detailed description of Persson's contact theory is reported, pointing out what I find to be some ambiguous and weak aspects of the theory, with some suggestions on how overcome the difficulties of the theory itself. A comparison with the results of the theory presented in section 4.2 is also presented.

4.1 Experimental diamond and silicon profiles

Diamond Detectors LTD, the producer of the diamond samples employed in the context of the RAPSODIA experiment, provided us with three batches of diamond samples. The first one was composed by diamond declared as "detector grade", for which no information about roughness was provided by the producer. The second, also declared as detector grade, was guaranteed with a roughness (average absolute deviation from the mean height) not exceeding 5 nm. The third was optical grade and was declared with a roughness less than 2 nm and furnished with detailed two-dimensional maps obtained with an optical profilometer VEECO NT9100. To the aim of studying the deformation of the surfaces under uniaxial stress, the information on the roughness alone is not of much significance, because, as it shall be proved in the next sections, not only the depth or the height of the asperities, but also their distribution in the plane is essential to define the rate of adherence of the two surfaces. For this reason, since the beginning, we have employed a two-dimensional optical profilometer in order to study and compare the surfaces at our disposition. We employed a Zygo New View 6000 Vigo white light interferometer operating on the basis of the phase-shift principle. A broad-band radiation is split in a way that the light diffused by the sample can interfere with that reflected by a reference mirror with an approximately equal optical path difference. The relative position of the sample is varied with a piezoelectric actuator at a constant rate. The intensity, recorded for each pixel by a CCD camera, varies with time, following a system of interference fringes modulated by an envelope function depending on the coherence distance of the light source (see Fig.4.1). The maximum of the envelope function, detected by simple filtering techniques, corresponds to the instant when the optical path difference between the two interfering radiations is zero. For each pixel, such maximum is reached at different times t_{max}, depending on the height of the diffusing point. Comparing the map $t_{max}(x, y)$ with those of same reference surfaces the instrument can be calibrated in a way that a vertical resolution of the order of one nanometer or better can be achieved.

For the present study, we compared 640×480 pixel images of samples obtained with the same field of observation of 351×264 μm^2, corresponding to a horizontal resolution of about 0.5 μm, while the vertical resolution is evaluated to be about

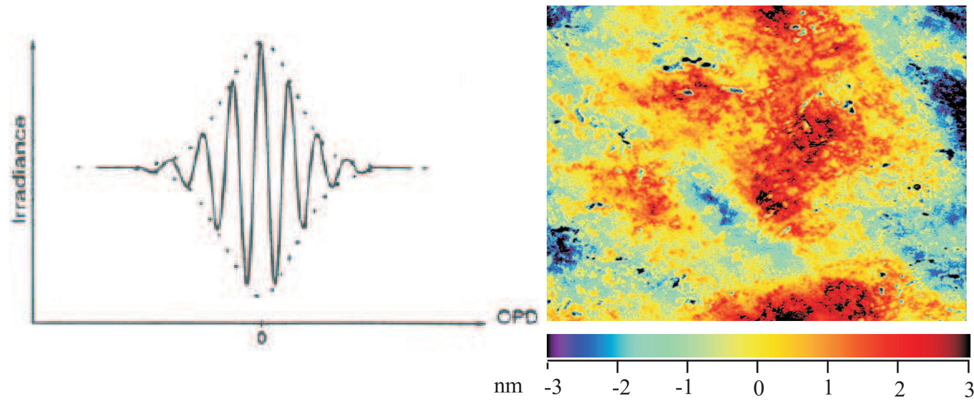

Figure 4.1: (left) interference fringes in white light, the maximum contrast is reached when the difference between the optical path of the diffused light and of the reference beam are equal. (right) profilometry of a typical silicon sample for electronic applications, used in our bonding experiments. The field is 696 ×523 μm^2 wide.

0.6 nm. Six typical images from the three batches of diamond samples are shown in figure 4.2, from both sides of the diamond plate. The two sides are not equivalent, because during diamond growth a selective growth of the grains takes place, in a way that the size of the grains on the growth side is always larger than that on the substrate size. While a marked improvement in smoothness is evident passing from the first to the second batch of the "detector" grade samples, the "optical grade" one, although declared with a roughness not exceeding 2 nm, does not seem to be better than the first one. It is evident that a study of the deformation of the surfaces under given uni-axial stress cannot be based only on roughness measurements, but has to be founded on a detailed knowledge of the samples profilometry.

Also the silicon surface profile was considered in this study: figure 4.1 shows a typical 351×264 μm^{2}image of a detector grade silicon sample. The different vertical scale of Fig. 4.1 and 4.2 puts in evidence how the major role is played by diamond profilometry, as far as prevision on silicon-diamond contact is concerned.

4.2 Contact mechanics at high pressure

We want to study the contact between a diamond and a silicon surface under uni-axial external pressure. Since the elastic constants of diamond are about one order of magnitude higher than those of silicon, while the inverse relation holds between the height of the asperities of the two materials (see figs. 4.1 and 4.2), it seems quite reasonable to study the contact between a perfectly rigid, rough surface and

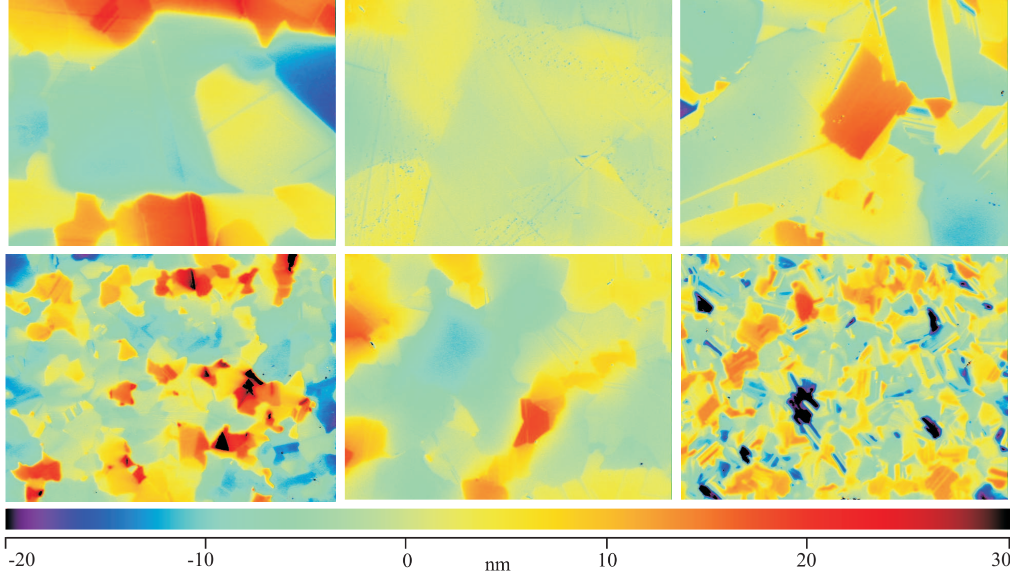

Figure 4.2: Images of the two sides (up: growth side, down: substrate side) of three samples from the three batches furnished by Diamond Detectors.

an elastic flat one. In this we are confirmed by the generally adopted approximation of contact theory (see ref. [69]), that is, if two rough surfaces, whose profiles are $h_1(x, y)$ and $h_2(x, y)$, with elastic moduli J_1 and J_2, are put in close contact, the problem is studied as one of a rigid surface with a profile $h = h_2 - h_1$ in close contact with a plane elastic surfaces whose elastic modulus is $J = 1/(1/J_1 + 1/J_2)$.

We will find the solution to the following problem (see also figure 4.3 for explanation):

- A perfectly rigid surface with a given profile $h\,(x, y)$ is pressed onto a cubic crystal layer with thickness $L \to \infty$ and elastic constants C_{11}, C_{12} and C_{44}. We want to calculate the pressure which is necessary for the attainment of a complete adherence and the local stress at the interface between the two surfaces.

The problem is indetermined until we fix some condition on the forces between the adherent points of the two surfaces. In practice, two cases can be treated in detail with a reasonable mathematic effort:

1. No friction: on the whole surface, the stress in the x and y direction is zero.
2. Vertical displacement: on the whole surface, the lateral displacement of each point is zero.

Once solved the problem in case of full contact between the two surfaces, we will suppose to slight diminish the uni-axial superimposed stress and we will determine which parts of the two surfaces will lose their contact.

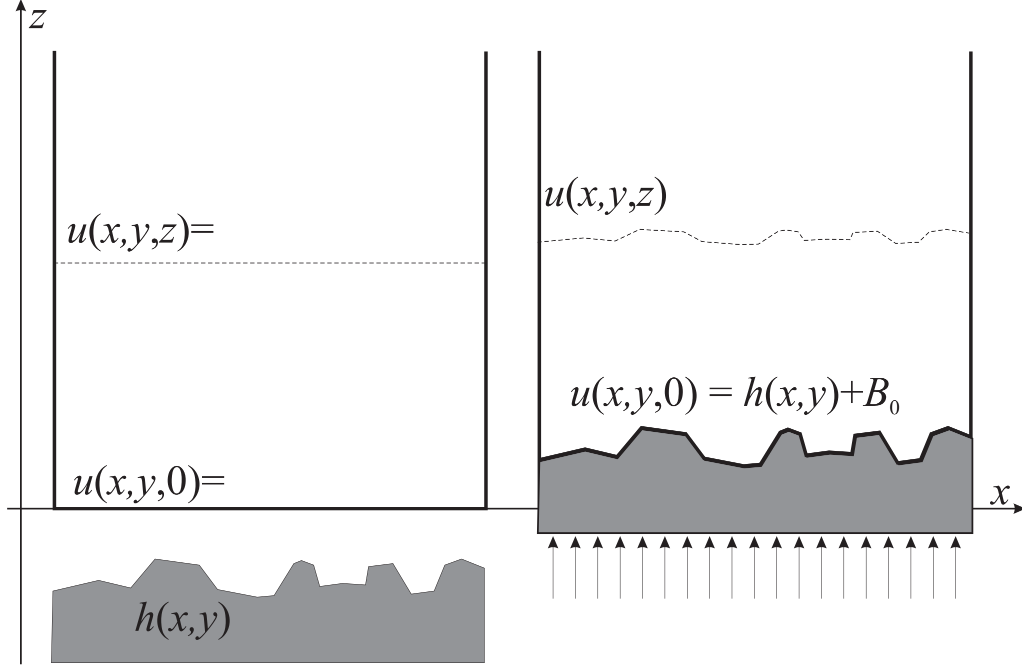

Figure 4.3: Scheme of the general problem of the adhesion of two materials, the first is elastic, infinitely extended in the z direction, with a flat boundary at $z = 0$, the second is perfectly rigid, with a profile described by a function $h(x, y)$, and is pressed onto the flat surface of the elastic media.

First we solve the simplified problem of a sinusoidal profile $h\left(x, y\right) = \Re\left(h_0 \exp\left(ikx\right)\right)$, then we extend the solution to the general case by fourier transformation. Let be v, w and u the three components of the displacement vector in the x, y and z direction, respectively. Since the system has a solution independent of the coordinate y and with a null component in the y direction, it is described by the two equations:

$$\begin{aligned} C_{11}u_{zz} + C_{44}u_{xx} + \left(C_{12} + C_{44}\right) v_{xz} = 0, \\ C_{11}v_{zz} + C_{44}v_{xx} + \left(C_{12} + C_{44}\right) u_{xz} = 0. \end{aligned} \tag{4.1}$$

Let be $u = \Re\widehat{u}$ and $v = \Re\widehat{v}$, with

$$\widehat{u}\left(x, z\right) = U \exp\left(ikx - \rho z\right) + B_0 + bz, \quad \text{and} \quad \widehat{v}\left(x, z\right) = V \exp\left(ikx - \rho z\right). \tag{4.2}$$

In these hypotheses, equations 4.1 imply:

$$\begin{aligned} \left(\rho^2 C_{11} - k^2 C_{44}\right) U - ik\rho\left(C_{12} + C_{44}\right) V = 0, \\ -ik\rho\left(C_{12} + C_{44}\right) U + \left(\rho^2 C_{44} - k^2 C_{11}\right) V = 0. \end{aligned} \tag{4.3}$$

The system 4.3 admits non-trivial solutions only if

$$\rho^4 + 2\left(\frac{C_{12}}{C_{11}} + \frac{C_{12}^2 - C_{11}^2}{2C_{11}C_{44}}\right)k^2\rho^2 + k^4 = 0. \tag{4.4}$$

Equation 4.4 has four solutions, two of which have negative real part and have no physical significance, implying divergent displacements for $z \to \infty$. The two other solutions have the form $\rho = \rho_{1,2} = k\alpha_{1,2}$, with

$$\alpha_{1,2} = \sqrt{\frac{C_{12}}{C_{11}} + \frac{C_{12}^2 - C_{11}^2}{2C_{11}C_{44}} \pm \sqrt{\left(\frac{C_{12}}{C_{11}} + \frac{C_{12}^2 - C_{11}^2}{2C_{11}C_{44}}\right)^2 - 1}}. \tag{4.5}$$

The most general forms of the functions $\widehat{u}$ and $\widehat{v}$ are then

$$\begin{aligned} \widehat{u} &= \left(U_1 e^{-\rho_1 z} + U_2 e^{-\rho_2 z}\right) e^{ikz} + B_0 + bz, \\ \widehat{v} &= \left(V_1 e^{-\rho_1 z} + V_2 e^{-\rho_2 z}\right) e^{ikz}, \end{aligned} \tag{4.6}$$

with $V_i = A_i U_i \equiv \frac{\rho_i^2 C_{11} - k^2 C_{44}}{ik\rho_i(C_{12}+C_{44})} U_i$.

A complete adherence of the rigid and the elastic media is attained if the elastic surface follows exactly the profile of the rigid one, as in

$$\widehat{u}\,(x,0) = (U_1 + U_2)\exp{(ikx)} + B_0 = h_0 \exp{(ikx)} + B_0, \tag{4.7}$$

where the term B_0 summed to $h(x)$ takes into account the vertical displacement necessary to adequately compress the elastic media. Condition 4.7 is not sufficient to determine the solution of the problem, it is also necessary to fix a condition on the horizontal displacement $\widehat{v}(x,0)$. As mentioned above, the two alternatives of zero horizontal displacement or zero horizontal stress have particularly simple mathematical expressions. The first is simply

$$V_1 + V_2 = 0, \quad \text{that is} \quad A_1 U_1 + A_2 U_2 = 0, \tag{4.8}$$

the second implies vanishing of the term $C_{44}\left(\frac{\partial \widehat{v}}{\partial z}(x,0) + \frac{\partial \widehat{u}}{\partial z}(x,0)\right)$, that means

$$\rho_1 V_1 + \rho_2 V_2 - ikU_1 - ikU_2 = 0, \quad \text{that is} \quad (\rho_1 A_1 - ik)\,U_1 + (\rho_2 A_2 - ik)\,U_2 = 0. \tag{4.9}$$

The real case, due to the static friction forces between the two surfaces, is probably an itermediate solution between the two extreme cases.

The solutions in case of vertical displacement are easily found:

$$\begin{aligned} \widehat{u} &= h_0 \left(\frac{A_2}{A_2 - A_1} e^{-\rho_1 z} - \frac{A_1}{A_2 - A_1} e^{-\rho_2 z}\right) e^{ikx} + B_0 + bz, \\ \widehat{v} &= h_0 \frac{A_1 A_2}{A_2 - A_1}\left(e^{-\rho_1 z} - e^{-\rho_2 z}\right) e^{ikx}. \end{aligned} \tag{4.10}$$

The proportionality constant b is found observing that the vertical stress at very long distances from the surface ($z \to \infty$) equals the superimposed external pressure P_∞, thus

$$P(x,\infty) = -C_{11}\frac{\partial u}{\partial z}(x,\infty) - C_{12}\frac{\partial v}{\partial z}(x,\infty) = -C_{11}b = P_\infty. \quad \text{that is} \quad b = -\frac{P_\infty}{C_{11}}. \tag{4.11}$$

At the interface between the two media, we have

$$P(x,0) = -C_{11}\frac{\partial u}{\partial z}(x,0) - C_{12}\frac{\partial v}{\partial z}(x,0) = \Re\left[C_{11}h_0\frac{\rho_1 A_2 - \rho_2 A_1}{A_2 - A_1}e^{ikx}\right] + P_\infty. \tag{4.12}$$

If we can neglect any possible attractive or repulsive force between the two surfaces, a complete adherence will imply a non negative value of $P(x,0)$ everywere, that is $P_\infty \geq P_0$, with (see also Eq.4.5)

$$P_0 = C_{11}|h_0|\left|\frac{\rho_1 A_2 - \rho_2 A_1}{A_2 - A_1}\right| = |h_0||k|\frac{\alpha_1+\alpha_2}{1+\alpha_1\alpha_2\frac{C_{11}}{C_{44}}} \equiv |h_0||k|J_{\text{vert. disp.}}. \tag{4.13}$$

Now, it easily verified that $\alpha_1\alpha_2 = 1$ and $\alpha_1 + \alpha_2 = \sqrt{2\left(\frac{C_{11}^2 - C_{12}^2}{2C_{11}C_{44}} - \frac{C_{12}}{C_{11}} + 1\right)}$, thus

$$J_{\text{vert. disp.}} = \frac{C_{11}C_{44}}{C_{11}+C_{44}}\sqrt{2\left(\frac{C_{11}^2 - C_{12}^2}{2C_{11}C_{44}} - \frac{C_{12}}{C_{11}} + 1\right)}. \tag{4.14}$$

In the case of silicon, $J_{\text{vert. disp.}}$ is about 93 GPa, while for diamond its value is 713 GPa. As anticipated in chapter 2, the simple dimensional relation 2.3, $P \approx J\frac{h}{l}$, where h is the typical height and l the typical distance between the peaks of the distribution, catches the essence of the physics involved in the phenomenon.

If we assume no friction and no horizontal stress occurring, a similar, even if more involuted algebra, gives a result analogous to Eq. 4.14, but with a modulus $J_{\text{no fric.}}$ which equals

$$J_{\text{no fric.}} = \frac{\frac{C_{11}^2 - C_{12}^2}{C_{11}}}{\sqrt{2\left(\frac{C_{11}^2 - C_{12}^2}{2C_{11}C_{44}} - \frac{C_{12}}{C_{11}} + 1\right)}}, \tag{4.15}$$

that equals 82 and 559 GPa for silicon and diamond, respectively.

Now, it is possible to solve the general problem, with a generic shape $H(x,y)$ of the rigid surface. Developing $H(x,y)$ in its Fourier components, we have

$$H(x,y) = \frac{1}{4\pi^2}\int_0^{2\pi} d\phi \int_0^\infty kdkh(k,\phi)\exp\left(ik\vec{u}_\phi \cdot \vec{r}\right), \tag{4.16}$$

with $\vec{r} = x\vec{u}_x + y\vec{u}_y$, $r = \sqrt{x^2 + y^2}$ and $\vec{u}_\phi = \vec{u}_x \cos\phi + \vec{u} \sin\phi$. The reality of H implies $h(r, \phi) = h^*(r, \phi + \pi)$. If we suppose, for the displacement field $\vec{s}(x, y, z)$, a solution of type

$$\vec{s}\,(x, y, z) = \frac{1}{4\pi^2} \int_0^{2\pi} d\phi \int_0^\infty kdk \left[u_{k,\phi}\,(z)\,\vec{u}_z + v_{k,\phi}\,(z)\,\vec{u}_\phi\right] \exp\left(ik\vec{u}_\phi \cdot \vec{r}\right) + \left(B_0 + bz\right)\vec{u}_z, \tag{4.17}$$

we find $u_{k,\phi}(z)e^{ik\vec{u}_\phi\cdot\vec{r}}$ and $v_{k,\phi}(z)e^{ik\vec{u}_\phi\cdot\vec{r}}$ to be bounded to $h(k, \phi)$, for every direction and spatial frequency, in the same way that $\widehat{u}$ and $\widehat{v}$ were bounded to h_0 in the simple sinusoidal case. In this case, the vertical stress at the height $z = 0$ depends on the applied external pressure P_∞ in the following way:

$$\begin{aligned} P\,(x, y, 0) = &\quad \pi\,(x, y)\,J + P_\infty \quad \text{with} \\ \pi\,(x, y) = &\quad \frac{1}{4\pi^2} \int_0^{2\pi} d\phi \int_0^\infty kdk \cdot h\,(k, \phi)\,e^{ik\vec{u}_\phi\cdot\vec{r}} \\ = &\quad 2\pi \iint_{-\infty}^{\infty} d\mu d\nu \sqrt{\mu^2 + \nu^2}\, h\,(\mu, \nu)\, e^{2\pi i(\mu x + \nu y)}, \end{aligned} \tag{4.18}$$

where J can be read $J_{\text{vert. disp.}}$ or $J_{\text{no fric.}}$ according to the boundary conditions on the plane $z = 0$. If π_m is the minimum of the function $\pi(x, y)$, a complete adherence is guaranteed if $P_\infty \geq -\pi_m J$.

If the externally superimposed pressure is not enough to obtain complete adherence, one can evaluate the detaching area as the area A_Ω of the region Ω over which $\pi(x, y)J + P_\infty < 0$. Obviously, since $\pi(x, y)$ assumes both negative and positive values (and has, on the average, a null value) this evaluation is exceedingly rough as $P_\infty \to 0$. In fact, in this case $\pi(x, y)J + P_\infty < 0$ for $A_\Omega \approx 0.5A_{\text{overall}}$, while the real rate of contact should tend to zero as $P_\infty \to 0$. Nevertheless, for $P_\infty \lessapprox -\pi_m J$, the ratio $A_\Omega/A_{\text{overall}}$ should approximate the effective detaching ratio, which in no case should exceed the double of $A_\Omega/A_{\text{overall}}$.

Having solved the problem of the determination of the pressure at the interface and of the detaching ratio for a given external pressure, we can face the determination of the overall volume of the voids between the two surfaces. We consider the particular case of the contact between a plane and an indented smooth surface. If a sufficient pressure P_∞ is applied, adhesion is complete and the pressure at the bottom of the dent is positive or null. If the pressure is too small, the elastic media come up until it reach a height h_{P_∞}. Now, if the profile of the surface were h_{P_∞}, the pressure on the bottom of the dent, with a pressure P_∞, would be zero, so that the difference $h_{P_\infty} - h$ is likely to be proportional to the difference $P_\infty + \pi(x, y)J$ between the applied pressure and the minimum pressure necessary to the adhesion, so that

$$\frac{\pi\,(x, y)\,J + P_\infty}{\pi\,(x, y)\,J} = \frac{h_{P_\infty}\,(x, y) - h\,(x, y)}{h\,(x, y)}. \tag{4.19}$$

In the practical cases the difference $h_{P_\infty}(x,y) - h(x,y)$ should not be compared with the absolute value $h(x,y)$, but to the heigh referred to a mean value around the indentation. This can be done by Fourier-transforming the function $h(x,y)$, applying a filter which smooths the shape of the indentation and finally anti-transforming, to obtain h_{smooth}. At this point the depth of the voids left between the two surfaces before irradiation, at every point (x,y), is given by:

$$\begin{aligned}\Delta h(x,y) = \quad & \chi_\Omega(x,y)\left[h_{P_\infty}(x,y) - h(x,y)\right] = \\ & \chi_\Omega(x,y)\left[h_{\text{smooth}}(x,y) - h(x,y)\right]\frac{\pi(x,y)J + P_\infty}{\pi(x,y)J},\end{aligned} \tag{4.20}$$

where χ_Ω is the characteristic function of the set Ω which, as just said above, is the region over which $P_\infty + \pi(x,y)J$ is negative.

In conclusion, the three problems of the calculation of the pressure at the interface of the two surfaces, of the detaching area and of the voids depth is reduced to the calculation of the function $\pi(x,y)$ in Eq.4.18, given the experimental profile of the surface $h(x,y)$.

In our case, we dispose of matrices $\Delta h \times H_{ij}$, with $1 \le i \le N$ and $1 \le j \le M$, representing a sampling of the surface on the two-dimensional lattice with elementary rectangular cells of dimensions L_x/N and L_y/M.

Now, if $h_{rs} = \sum_{i=0}^{N-1}\sum_{j=0}^{M-1} H_{ij}\exp\left[-2\pi\hat{i}\left(\frac{ir}{N} + \frac{js}{M}\right)\right]$, is the discrete Fourier transform of the matrix H_{ij}, it follows:

$$\begin{aligned}\pi(x,y) &= \pi(iL_x/N, jL_y/N) = 2\pi\frac{1}{NM}\frac{\Delta h}{\sqrt{L_xL_y}}\eta_{ij} \quad \text{with} \\ \eta_{ij} &= \sum_{r=0}^{N-1}\sum_{s=0}^{M-1}\sqrt{\frac{r^2}{L_x/L_y} + \frac{s^2}{L_y/L_x}}\,h_{rs}\exp\left[-2\pi\hat{i}\left(\frac{ir}{N} + \frac{js}{M}\right)\right].\end{aligned} \tag{4.21}$$

Equation 4.21 permits to calculate the value of the function $\pi(x,y)$ with the horizontal resolution characteristic of the profilometer.

4.3 Contact mechanics of the diamond and silicon samples

The three batches of diamond samples which were purchased for our bonding experiments were characterized with the method which has been described in the previous section.

In figure 4.4 the map of a sample of the first batch is shown, along with three maps where the non contact areas of the sample are drawn in black, identified as those giving a negative pressure $P(x, y, 0)$ in Eq. 4.18, for three values of the external uni-axial stress P_∞: 80, 160 and 240 MPa (in our experiments we have applied 80 MPa). The value adopted for the modulus J was $J = 1/(\frac{1}{J_{\text{diamond}}} + \frac{1}{J_{\text{silicon}}})$, with $J_{\text{silicon,diamond}}$ taken as in the vertical displacement case. For each sample of the three batches, the non-contact rate was calculated for different values of the pressure. In figure 4.5 (left) the detachment rate of six samples of the third batch is shown as a function of pressure (in unit J), both for the front and for the back side of the sample. The better behavior of the growth side of each sample is evident. In figure 4.5 (right) it is also shown the mean value of the detachment rate for the three batches as a function of pressure. It result that, in spite of its nominally lower roughness index, the third batch has a performance comparable with the first one. Moreover, a feature, not discernable from the simple knowledge of the roughness index, clearly emerges from inspection of the figure: even if at relatively low pressures the roughest first batch performs quite badly, its adhesion to silicon is comparatively better than that of the second one at high pressures, because polishing creates scratches with a high depth-to-width ratio, which enhance the high spatial frequency components of the Fourier transform of $h(x, y)$ and, consequently, the values of $\pi(x, y)$.

In order to calculate the depth of the possible voids left in the interface as an effect of a non perfect pre-adhesion of the two surfaces, I evaluated, for a sample of each of the three batches under consideration, the function $\Delta(x, y)$ and its distribution $\Phi(d)$, defined as

$$\Phi(d) = \frac{1}{A} \int_A \delta(\Delta(x, y) - d)\, dxdy. \tag{4.22}$$

In figure 4.6 the three distributions are shown. It is quite evident that only a very small fraction of the overall area exhibits a voids depth greater than 1 or 2 nm, that is, the voids ubiquitously found in all the TEM images, extending to a depth of several nanometers, are certainly due to other causes than lack of pre-bonding contact.

The last issue addressed by the theory is the local stress distribution at the silicon-diamond interface. Since the local stress is described by the function $P(x, y, 0) = J\pi(x, y) + P_\infty$ of equation 4.18, it is very convenient to plot the distribution $\Phi(p)$ of the function $\pi(x, y)$, defined as in equation 4.22, but with the function $\pi(x, y)$ instead of $\Delta(x, y)$. The distribution of the local stresses, for values of the uni-axial pressure sufficiently high, is obtained, in unit of the modulus J, simply by translation on the right of the distribution, of an amount P_∞/J. In figure 4.7 the map of the function $\pi(x, y)$ is drawn, for the same sample of figure 4.4. On the right, the plot of the distribution $\Phi(p)$ is given.

4.4 Measurement of the local pressure

It is known from measurements on silicon crystals under uni-axial tension that the silicon Raman peak at 521 cm^{-1} is subject to a shift toward lower or higher wavenumbers, according to the positive or negative sign of the stress tensor component, of an amount proportional to the stress with a proportionality constant of 0.0023 cm^{-1}(MPa)$^{-1}$ [71, 72].

This fact suggests a method to measure the local stress of the silicon plate when pressed onto the diamond sample and the quartz window. If a high-spatial and spectral resolution micro-Raman measurement is performed through the quartz window and the diamond, it should be possible to measure the local uni-axial stress and, within the spectral resolution, to detect the non contact areas. A set up for a micrometric, computer assisted xy movement of the samples and a new irradiation chamber with possibility of pneumatic application of high pressures without risk of horizontal displacement are presently under study. Once such an apparatus will be implemented, the Raman apparatus available within our collaboration will allow us both to perform local stress measurements point by point as function of the uni-axial stress, and to draw maps of the local stress with a resolution of a few micrometers. At present, we have performed a preliminary study to assess the feasibility of the measurement. We employed a sample of the second batch, and we measured the position of the silicon Raman line in 14 points of the sample before and after the compression. Unfortunately, during the compression of the spring it was impossible to avoid a slight rotation of the irradiation chamber, which made it impossible to measure the stress exactly in the same points (within a 3-5 μm of resolution) after the compression, so that the two distributions has to be considered as independent.

The results of the measurements are represented if figure 4.8 (left), both before and after compression. Two features of the local pressure distribution are comparable with the theory: the average value is equal to the external superimposed uni-axial compression, while the standard deviation, if the non-contact area is relatively low, should be equal to the standard deviation of the distribution $\Phi(p)$ (see section 4.3) times the value of the modulus J. The distribution $\Phi(p)$ has been evaluated by the analysis of four different images of the sample under consideration, in different regions of the sample. The resulting mean distribution of the local pressure is shown in figure 4.8 (right). It has a standard deviation of 0.0010, which corresponds, with a value of J conventionally assumed to be $J \equiv \sqrt{1/\left(1/J^{\mathrm{Si}}_{\mathrm{vert.\ disp.}} + 1/\mathrm{vert.\ disp.}^{\mathrm{D}}\right) 1/\left(1/J^{\mathrm{Si}}_{\mathrm{no\ fric.}} + 1/\mathrm{no\ fric.}^{\mathrm{D}}\right)} = 77$ GPa, to about 77 MPa.

Now it is possible to compare the information from the Raman measurement with that deduced from the profilometry. The difference in the mean position of

the Raman line after and before compression, divided by the constant k =0.0023 cm^{-1}(MPa)$^{-1}$, gives a pressure of 112 MPa, with a standard error s_p evaluated by the standard deviations s_1 and s_2 of the two distributions $s_p = k\sqrt{\frac{s_1^2+s_2^2}{N-1}}$=35 MPa. This value is compatible with the known value of the external uni-axial stress of about 80 MPa. If one considers the distribution of the peak positions after the compression as a convolution of the original one (before compression) and of the local pressure distribution, it results that the standard deviation of the local pressure distribution can be evaluated as $\epsilon_p = k\sqrt{s_2^2 - s_1^2}$=112 MPa, the standard error on this value, this time, is given by $s_\epsilon = k\sqrt{\frac{s_2^4+s_1^4}{(N-1)(s_2^2-s_1^2)}}$=36 MPa. Also this value is fairly compatible with the calculated one of about 77 MPa.

Although it is worth to perform further experiments to assess the foundation of the theory, the present results suggest that its employment in the evaluation of the diamond profiles and in the choice of the uni-axial pressure to be exerted is well motivated at least at a preliminary level. The instruments offered by the theory could be particularly useful whenever a scale-up of the experimental set-up will impose stringent limits to the exerted local pressure. In this case, an acceptable contact ratio will be reached only if the surface profile of the diamond samples will be sufficiently smooth, and in this case the numerical analysis of the surfaces will be of crucial importance.

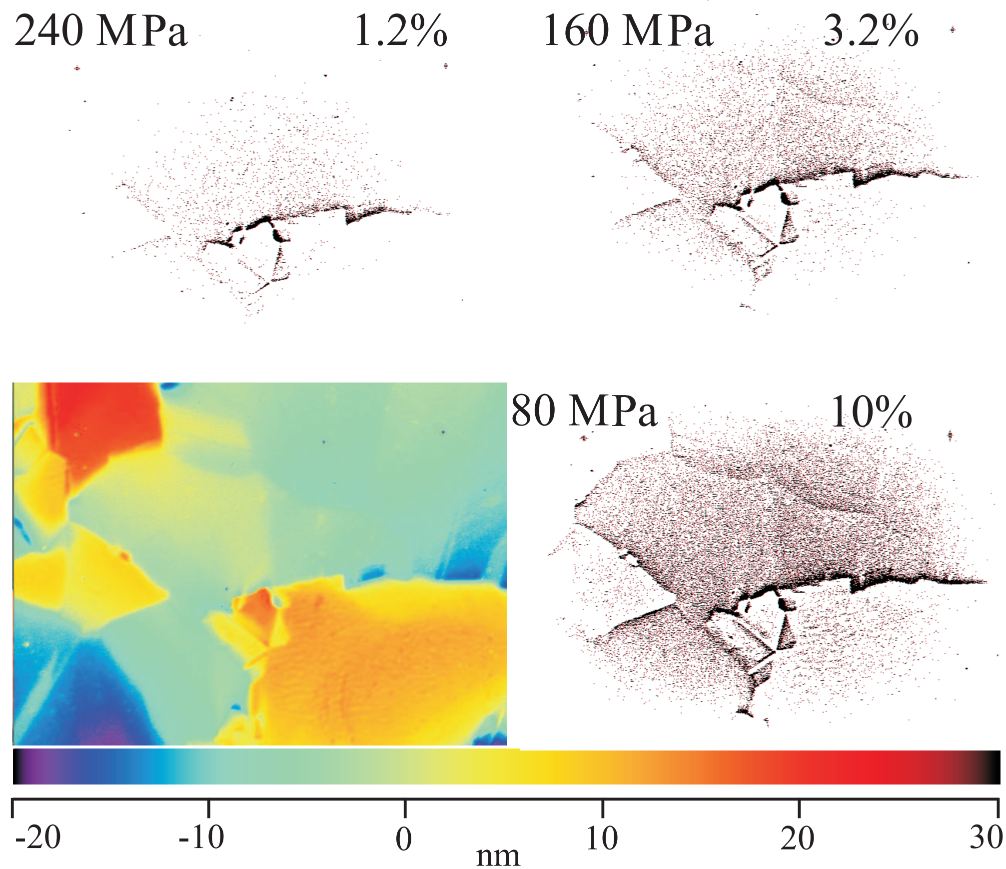

Figure 4.4: Profilometry of a sample of the first batch (field sizes 351×264 μm^2) along with the detachment areas for several values of the uniaxial pressure P_∞. The Fourier analysis of the surface has been performed by multiplying the height map by the square of a normalized sinc function, in order to minimize spurious effects on the boundaries. In this way, the detachment areas result overestimated at the center and undersestimated in the external frame of the image. The detachment ratio at each pressure is indicated in percent.

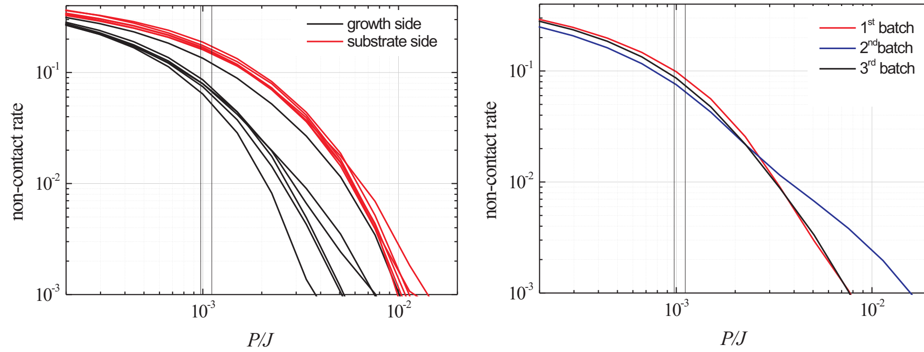

Figure 4.5: (left) Non-contact rate as a function of uni-axial stress (in unit of the modulus J) for six samples of the third batch, both for the growth side (in black) and for the substrate side (in red). (right) Average non-contact rate for the three batches employed in the bonding experiments.

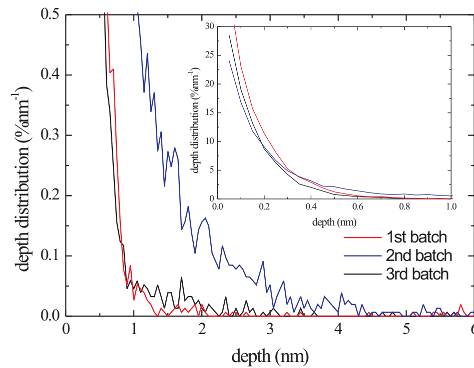

Figure 4.6: Distribution of the voids depth for three samples of the three batches at our disposition. In the inset, the same distribution on a larger scale.

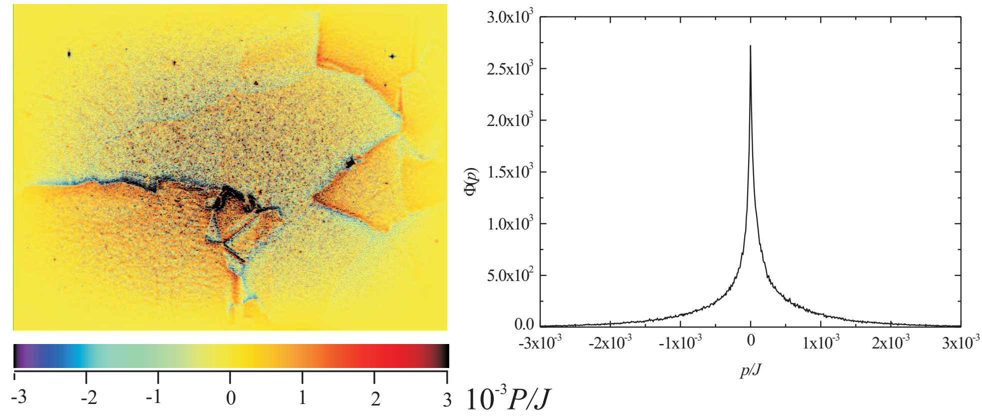

Figure 4.7: (left) Map of the function $\pi(x, y)$ for the sample whose profilometry is shown in figure 4.4. (right) Distribution of the values of $\pi(x, y)$.

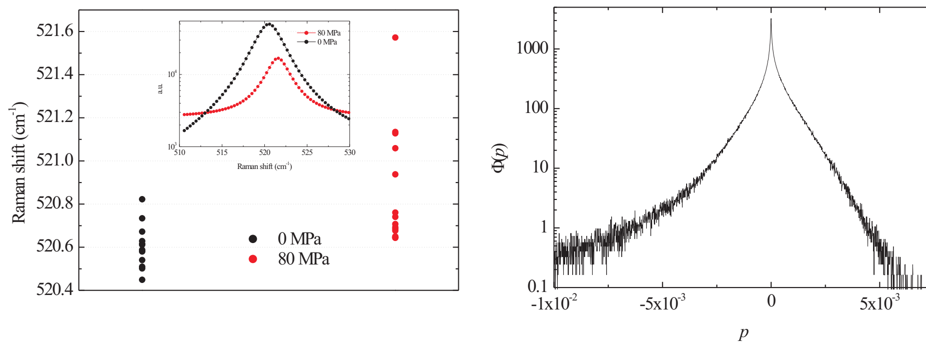

Figure 4.8: (left) The distributions of the measured Raman shift before and after compression. In the inset, two Raman profiles for 0 and 80 MPa of uni-axial stress, respectively. (right) Distribution of the values of $\pi(x, y)$ for the diamond sample used in the experiment. The asymmetry in the distribution is due to the presence of scratches with high depth-to-width ratio.

Part II

Ion implantation in diamond for monolithic photonic devices

Chapter 5

Why diamond as a photonic devices substrate

The last two decades have seen increasing effort in the attempt to control and manipulate the interaction of atomic systems at the quantum level, to the aim of disclosing a viable way toward quantum computation. Several solutions for storage, transport and elaboration of quantum information has been proposed: atoms in an ion trap[73], or atom-like systems like point-defects in solids can perform pretty well, in principle, for storing and computing quantum information, but in order to ensure transport without degradation photons are a better choice, since photon-matter and (even more) photon-photon interaction can be easily kept under a reasonable threshold. For the same reason, photons perform very well in storage of quantum information, but conventional optical non-linear mediums don't assure a photon-photon coupling strong enough for quantum elaboration purposes. Miniaturization and scalability are other requirements that should be satisfied in future quantum-computer architectures, which seems to limit the "optical breadboard"-approach to photon technology[74, 75], as well as the conventional quantum cavity[76] experiments, to no more than the proof of concept stage of the research. Even if other substrates are currently under study, like superconducting media[77] and optical lattices [78], and even if efforts are made to conceive integration techniques avoiding obstacle toward scalability in systems which can be manipulated at the quantum level at the small scale, e.g. for ion-trap architectures[79], the envision of *some* kind of solid state quantum computer seems highly motivated. These could employ point-like centers as quantum dots[80, 81] or lattice defects[82] in semiconductors.

In this context, the concept of quantum computation by interaction of photons and point-like defect in diamond is attracting a growing interest[83, 84], for a number of reasons: The null nuclear spin of the C^{12} isotope makes very long the coherence time of the spin state of several among the many tens of its color centers, even at

room temperature[85, 86]. That is, quantum information can be stored for relatively long times in defect centers in diamond, in the form of quantum superposition of spin states. Some of the defect centers in diamond exhibit a very high dipole momentum, ensuring a strong coupling with photons and ultimately fast reading-writing and commuting times[87, 88, 89, 90]. Last, but not least, high refractive index and broad transparency of diamond makes it operative in photonic transport from far infrared to deep ultraviolet, and currently available micro-fabrication techniques makes reachable the integration of photonic devices into diamond[91, 92, 93, 94, 95, 96, 97, 98].

The experimental effort of our group was addressed toward the modification of the optical property of diamond by means of micro-beam ion implantation and the fabrication of buried micro-written waveguides. This chapter is intended to explain how diamond can fulfill the demands for a solid state substrate for quantum computation and how our research can represent a significant step toward the engineering of diamond bulk for photonic applications. In the first section, some of the main concepts of quantum computation are resumed. My principal reference in this section is the classical text of Nielsen and Chuang[99]. In the second section, physical implementation of quantum gates for a Λ atomic system in a quantum cavity is discussed, with a focus on the employment strategies of diamond in practical communication and elaboration protocols. The third section is devoted to underline the demand of a reliable refraction index modulation technique, in order to dispose of a tool for the tailoring of photonic devices.

5.1 Quantum information and quantum computation

Quantum information and quantum computation differ very basically from the correspondent "classical" concepts. Classical information can be ultimately encoded in the form of a string of bits, that is a finite, ordered set of two-valued variables. Quite differently, one "bit" of quantum information (quantum bit, qubit) is a normalized vector of a two-dimensional Hilbert space on the complex field of kind

$$|q\rangle = a_0|0\rangle + a_1|1\rangle = \sum_{k=0}^{1} a_k|k\rangle, \tag{5.1}$$

where the pair $\{|0\rangle, |1\rangle\}$ is usually referred to as the "computational basis". Moreover a string of N qubits "lives" in a 2^N-dimensional Hilbert space given by the tensor product of the N 2-dimensional spaces, and cannot be generally factorized in

the form $|q_1\rangle|q_2\rangle \dots |q_N\rangle$, being representable as

$$|\psi\rangle = \sum_{k_1 \dots k_N = 0}^{1} \psi_{k_1 \dots k_N} |k_1\rangle \dots |k_N\rangle. \tag{5.2}$$

where $\{|k_1\rangle \dots |k_N\rangle\}_{k_1,\dots,k_N=0,1}$ is the computational basis in the 2^N Hilbert space. Also quantum computation rests on principles very different from classical ones. Classical computation, applied to a string of bits, can be reduced to the application of a suitable truth-table to the input string, in order to obtain the desired output. Quantum computation operates on the input vector performing a unitary transformation, which corresponds to the dynamics determined by some kind of hamiltonian interaction between the qubits themselves or between them and rest of the computer. As a very noticeable example of unitary transformation, employed as a sort of "subroutine" in many important quantum algorithms, I mention here the quantum Fourier transform, which performs the discrete Fourier transform of the coefficients of a given input vector along the computational basis $|0\dots00\rangle$, $|0\dots01\rangle$, $|0\dots10\rangle$ ... $|1\dots11\rangle$. If we indicate with $k \equiv k_1 \dots k_N$ (with $k_i = 0$ or 1)the number $k_1 2^{N-1} + \dots + k_N 2^0$, the quantum Fourier transform operates in this way:

$$\sum_{j=0}^{2^N-1} x_j |j\rangle \overset{QFT}{\longrightarrow} \sum_{k=0}^{2^N-1} y_k |k\rangle \quad \text{with} \quad y_k \equiv \frac{1}{\sqrt{2^N}} \sum_{j=0}^{2^N-1} x_j e^{\frac{2\pi \hat{i} jk}{2^N}}. \tag{5.3}$$

One of the most striking differences between classical an quantum computation is that even if the input vector is prepared as a product of $|0\rangle$ and $|1\rangle$ kets of kind $|k_1^I\rangle \dots |k_N^I\rangle$, a measurement on the output vector can give generally different strings of kind $k_1^O k_2^O \dots k_N^O$ ($k_i^O = 0$ or 1), with a probability $|\psi_{k_1^O \dots k_N^O}|^2$ (see Eq.5.2) depending on the unitary transformation performed. For instance, the application of the quantum Fourier transform doesn't allow direct evaluation of the discrete Fourier transform itself; at most, with a high number of calculation iterations, one can hope to measure the square modulus of its elements, which is the probabilities of occurrence of any given $k_1^O k_2^O \dots k_N^O$. Practical employment of a quantistic algorithm requires one to be more subtle. The art of quantum computing is to build a unitary operation which performs, at least on a specific subset of possible base vectors, a transformation, in a way that for any allowed input of kind $|k_1^I\rangle \dots |k_N^I\rangle$, all the probabilities $|\psi_{k_1^O \dots k_N^O}|^2$ are zero except one, so that the measurement output is strictly deterministic.

The fascination of quantum computing depend on the fact that some problems whose solution is considerably demanding, in terms of computing time, in classical computation, would be exponentially faster with a quantum computer. If the unitary operator resolving one of this problems is implemented by subsequent application

of operations involving only one or two qubits, the number of the operations grows only polynomially with the length of the input string, while the number of logic mono or binary operations of a classical computer to perform the same task would grow exponentially.

The next three subsections shows how it is possible to build the quantum Fourier transform with 1 and 2 qubit gates, and to employ it to perform a task of considerable importance: the factorization of an integer number, a problem of great practical relevance which is known to be of exponential complexity for the best known classical algorithm.

5.1.1 Quantum Fourier Transform

It is possible to perform the quantum Fourier Transform (QFT) of a given state vector disposing of two kind of unitary transformations operating only on 1 and 2 qubits respectively: the *Hadamard* gate, which act over a 1-qubit state in the following way:

$$H = \frac{1}{\sqrt{2}} \left(|0\rangle\langle 0| + |0\rangle\langle 1| + |1\rangle\langle 0| - |1\rangle\langle 1| \right), \tag{5.4}$$

and a controlled-R_k phase shift, which acts over a 2-qubits state according to

$$cR_k = |0\rangle\langle 0| \otimes I + |1\rangle\langle 1| \otimes \left(|0\rangle\langle 0| + e^{\frac{2\pi \hat{i}}{2^k}} |1\rangle\langle 1| \right). \tag{5.5}$$

Eq.5.5 is an example of controlled-U operator, which acts over the tensor product of a 1-bit and an N-bit space, in a way to leave unaltered the vector of the N-bit space if the first qubit is $|0\rangle$, and to apply U if it is $|1\rangle$:

$$cU = |0\rangle\langle 0| \otimes I + |1\rangle\langle 1| \otimes U. \tag{5.6}$$

A useful graphical representation of the H and cU gates is found in figure 5.1, where horizontal lines represent the flux of quantum information, each line labeling a specific q-bit of the computational basis. Figure 5.2 represents the diagram of

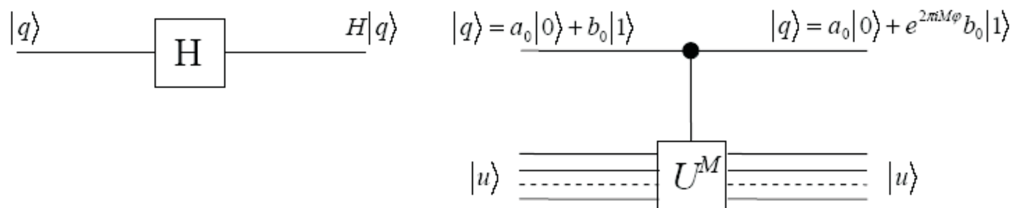

Figure 5.1: Graphical representation of the Hadamard gate and of the cU^N gate.

an operator which is able to perform a QFT. In the diagram, we assume to have an input given by the tensor product of single qubit states, $|j_1\rangle|j_2\rangle\ldots|j_N\rangle$, being the general case obtained with a linear combination of such a kind of vectors. The swap-block perform a simple inverse re-ordering of the indexes. Each H gate, applied to the nth bit, transforms it according to

$$|j_n\rangle \longrightarrow \frac{1}{\sqrt{2}}\left(|0\rangle + e^{\pi j_n \hat{i}}|1\rangle\right), \tag{5.7}$$

while the succession of controlled transformations gives a final result:

$$\begin{aligned} &cR_{N-n}\left(\ldots cR_3\left(cR_2\left(H|j_n\rangle\right)|j_{n+1}\rangle\right)\ldots|j_N\rangle\right) = \\ &\frac{1}{\sqrt{2}}\left(|0\rangle + e^{2\pi\hat{i}0.j_n j_{n+1}\ldots j_N}|1\rangle\right)|j_{n+1}\rangle\ldots|j_N\rangle, \end{aligned} \tag{5.8}$$

where we have defined $0.j_1 j_2\ldots j_k \equiv j_1\times 2^{-1} + j_2\times 2^{-2} + \cdots + j_k\times 2^{-k}$. Thus, the overall result of the transformation is

$$\frac{1}{\sqrt{2^N}}\left(|0\rangle + e^{2\pi\hat{i}0.j_N}|1\rangle\right)\left(|0\rangle + e^{2\pi\hat{i}0.j_{N-1}j_N}|1\rangle\right)\ldots\left(|0\rangle + e^{2\pi\hat{i}0.j_1 j_2\ldots j_N}|1\rangle\right) \tag{5.9}$$

This is proved to be the QFT of the initial state vector by the following chain of equalities:

$$\begin{aligned} &\frac{1}{\sqrt{2^N}}\prod_{l=1}^{N}\left(|0\rangle + e^{2\pi\hat{i}j2^{-l}}|1\rangle\right) = \frac{1}{\sqrt{2^N}}\prod_{l=1}^{N}\sum_{k_l=0}^{1} e^{2\pi\hat{i}j2^{-l}k_l}|k_l\rangle = \\ &\frac{1}{\sqrt{2^N}}\sum_{k_1 k_2\ldots k_N=0}^{1} e^{2\pi\hat{i}j\sum_{l=1}^{N}2^{-l}k_l}\prod_{l=1}^{N}|k_l\rangle = \frac{1}{\sqrt{2^N}}\sum_{k=0}^{2^N-1} e^{\frac{2\pi\hat{i}jk}{2^N}}|k\rangle \end{aligned} \tag{5.10}$$

The necessary time for an algorithm to be performed is usually estimated by counting the number of logical gates involved in the algorithm itself, by this assuming each gate to require a finite time to accomplish its task. Noticeably, the number of gates which are necessary to perform the quantum Fourier transform is $n(n+1)/2$, that is, an $O(n^2)$. In contrast, the fastest classical algorithms for computing the discrete Fourier transform on 2^n elements, like the fast Fourier transform algorithm, compute it by means of an $O(n2^n)$ classical gates. As just mentioned, it is not possible to use the QFT algorithm to compute directly the Fourier transform of a classical function, because no measurement process can give the amplitudes of the QFT components. Nevertheless, it is possible to use the QFT to efficiently perform tasks which could be much hardly fronted by any classical algorithm. A typical example of such a task is the factorization of an integer number, whose best, presently known, solving algorithm takes a time proportional to $O\left(\exp\left(\left(\frac{64}{9}n\right)^{1/3}(\log n)^{2/3}\right)\right)$

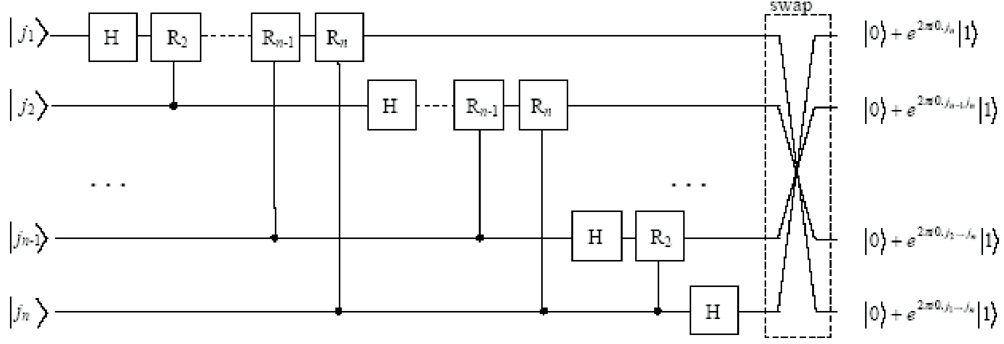

Figure 5.2: Graphical representation of a circuit performing quantum Fourier Transform.

[100], where n is the number of digits of the number to be factorized. This problem is solved, in quantum computation, with a number of ports growing whith a power of n, by performing of three steps: phase estimation, order finding, and the factorization itself. The next two subsections are devoted to this problem .

5.1.2 Phase estimation

The first step in the solution of the factorization problem is the determination of the eigenvalue $e^{2\pi i\phi}$ of a given unitary transformation U relative to the eigenvector $|u\rangle$. It is possible to determine the phase ϕ with the desired precision (i.e. with the desired number N of binary digits) disposing of a physical model of the eigenvector $|u\rangle$ and of two kind of operators, an Hadamard gate and a *controlled-*U^N operator.

Consider the unitary operator whose graphical representation is illustrated in Fig. 5.3. Given an input vector of type $|0\rangle_1 \dots |0\rangle_N |u\rangle$, the state vector at the end of the operation is $|\psi\rangle|u\rangle$, where

$$\begin{aligned}|\psi\rangle = \quad & \frac{1}{2^{N/2}}\left(|0\rangle + e^{2\pi\hat{i}2^{N-1}\phi}|1\rangle\right)\left(|0\rangle + e^{2\pi\hat{i}2^{N-2}\phi}|1\rangle\right)\dots\left(|0\rangle + e^{2\pi\hat{i}2^{0}\phi}|1\rangle\right) = \\ & \frac{1}{2^{N/2}}\prod_{i=1}^{N}\sum_{k_i=0}^{1} e^{2\pi\hat{i}2^{N-i}\phi k_i}|k_i\rangle = \frac{1}{2^{N/2}}\sum_{k_1\dots k_N=0}^{1} e^{2\pi\hat{i}\phi\sum_{i=1}^{N}2^{N-i}k_i}\prod_{i=1}^{n}|k_i\rangle = \\ & \frac{1}{2^{N/2}}\sum_{k=0}^{2^N-1} e^{2\pi\hat{i}\phi k}|k\rangle \end{aligned} \tag{5.11}$$

If the phase ϕ has exactly N binary digits $\phi = 0.\phi_1\phi_2\dots\phi_N$, by comparison of Eq.5.7 we realize that $|\psi\rangle$ is the quantum Fourier transform of the vector $|\phi_1\phi_2\dots\phi_N\rangle$. Consequently, the inverse quantum Fourier transform QFT^+ gives as an output

$|\phi_1\phi_2 \dots \phi_N\rangle$, and a projective measurement performed on the state vector at this point gives, for each qubit, the results $|0\rangle$ if $\phi_i = 0$ and $|1\rangle$ if $\phi_i = 1$.

If we cannot dispose of the physical realization of a specific eigenvector $|u\rangle$, it is yet possible to measure the phase of the U eigenvalues giving whatever an input pure vector state $|\chi\rangle$, which is decomposable in term of eigenvectors of U as $|\chi\rangle = \sum_s c_s|u_s\rangle$. In this case, the output will be the phase ϕ_s of one of the eigenvalues with a probability $|c_s|^2$.

In any physical situation, phases can be defined with a number of significant digits greater than the size N of the output binary string, but it is possible to prove that the procedure gives accurately the first n phase digits with a failure probability lesser than $\epsilon = \frac{1}{2(2^{N-n}-2)}$.

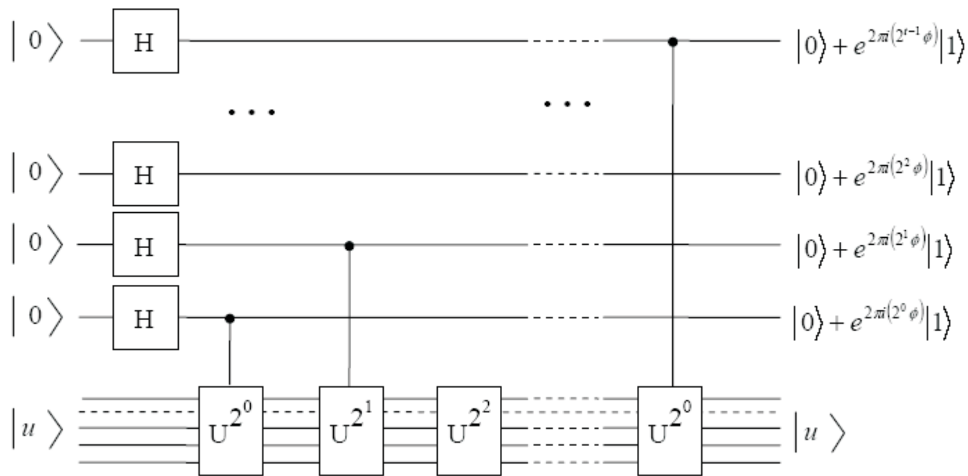

Figure 5.3: Graphical representation of a circuit performing phase estimation.

5.1.3 Order-finding and factoring

An important step in the determination of a nontrivial factor for a given number is the solution of the order-finding problem. If $x < N$ are integer numbers with no common factors, the *order* of x modulo N is the least positive integer r such that $x^r \bmod N = 1$. An order finding algorithm can be employed in the factorization of number N thanks to the theorem which states that if z is a not trivial solution of the equation $z^2 \bmod N = 1$ (that is, with $z \bmod N \neq \pm 1$) then $z - 1$ or $z + 1$ and N have a common nontrivial factor.

As a consequence, given a random number $1 < x < N - 1$, having no other

common divisors whith N than 1 (i.e. *co-prime* to N), if the order r of x modulo N is even and $x^{r/2}$ mod $N \neq -1$, then at least one of the numbers $x^{r/2} \pm 1$ has a common nontrivial factor with N, that is, the factorization reduces to the calculation of the greater common divisor between $x^{r/2} \pm 1$ and N (a task easily performed by means of a classical algorithm).

Unfortunately, the order finding problem is a difficult classical computational problem, with exponential complexity, but the phase estimation quantum algorithm allows its solution if one can perform the unitary operation controlled-U_x, with U_x defined by

$$U_x|y\rangle \equiv \begin{cases} |xy \text{ mod } N\rangle & \text{if} \quad y \leq N-1 \\ |y\rangle & \text{if} \quad y \geq N \end{cases} \tag{5.12}$$

Now, a simple calculation shows that the eigenvectors of U_x, with eigenvalues $e^{\frac{2\pi \hat{i} s}{r}}$, are

$$|u_s\rangle = \frac{1}{\sqrt{r}} \sum_{k=0}^{r-1} e^{-\frac{2\pi isk}{r}} |x^k \text{ mod } N\rangle, \tag{5.13}$$

and more importantly that the trivially obtainable vector $|1\rangle = |0\rangle_1 |0\ldots\rangle_{L-1} |1\rangle_L$ is given by

$$|1\rangle = \frac{1}{\sqrt{r}} \sum_{k=0}^{r-1} |u_s\rangle. \tag{5.14}$$

The application of the phase estimation algorithm to the vector $|1\rangle$ gives, with equal probability, the first L digits of the binary fractional expression of $\frac{s}{r}$, with $0 \leq s \leq r-1$. At this point, a classical algorithm serves to the calculation of the integer r.

5.1.4 Universal quantum gates

In classical computation, any truth table can be obtained assembling a limited set of logic gates acting on one or two bits only. A similar result is valid also for quantum computation. It can be proved [99] that every unitary operator on a set of N qubits can be obtained to the desired degree of approximation by means of two on-qubit gates and one two-qubit gate. Moreover, the approximation can be performed efficiently, in the sense that the required number of elementary gates grows with the accuracy $\epsilon = \sup |(U - U_{\text{approx.}})|\psi\rangle|$ of the approximation only as an $O(-\log \epsilon)$.

As well as for classical circuits, several choices are possible as elementary sets of quantum gates. One is given by two gates acting over one qubit, and one gate

which makes interact two qubits. The 1-qubit gates are the Hadamard and the T gate, the latter being defined by:

$$T = |0\rangle\langle 0| + e^{\hat{i}\frac{\pi}{4}}|1\rangle\langle 1| = e^{\hat{i}\frac{\pi}{8}}\left(e^{-\hat{i}\frac{\pi}{8}}|0\rangle\langle 0| + e^{\hat{i}\frac{\pi}{8}}|1\rangle\langle 1|\right), \tag{5.15}$$

The 2-qubit gate is the controlled-NOT gate, defined by

$$cNOT = |0\rangle\langle 0| \otimes I + |1\rangle\langle 1| \otimes (|1\rangle\langle 0| + |0\rangle\langle 1|). \tag{5.16}$$

For instance, the controlled-R_k gate employed in the QFT algorithm is given by the product $\left(I \otimes R_{k+1}^{+}\right) cNOT \left(I \otimes R_k\right) cNOT \left(I \otimes R_{k+1}^{+}\right)$ (see also figure 5.4) with

$$R_k = e^{\frac{2\pi\hat{i}}{2^k}}|0\rangle\langle 0| + |1\rangle\langle 1|. \tag{5.17}$$

On the other hand, any 1-bit operator, including R_k itself, can be represented in term of products of rotations around two non-parallel given axis. Now, it is easy to see that the operators $(TH)^2$ and $(HT)^2$ represent rotations around the directions $(\cos\frac{\pi}{8}, \pm\sin\frac{\pi}{8}, \cos\frac{\pi}{8})$ of an angle $\theta = 2\cos^{-1}\left(\cos^2\frac{\pi}{8}\right)$, an irrational multiple of π whose multiples can approximate, modulo 2π, whatever given angle. As a consequence, R_k as well as any other 1-qubit operator, up to a global phase, can be approximated in term of suitable products of $(TH)^2$ and $(HT)^2$.

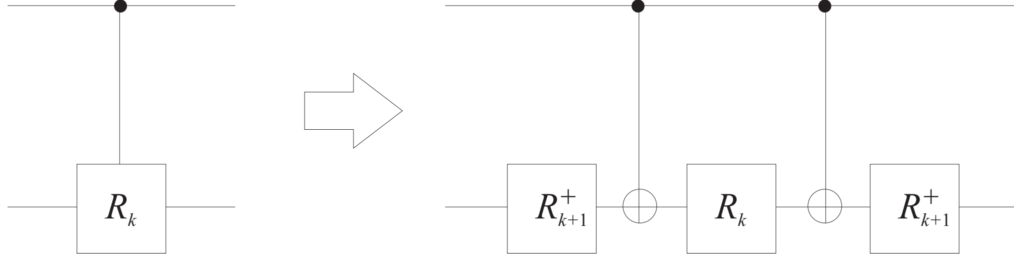

Figure 5.4: Realization of a controlled-R_k gate employing one R_k and two R_k^{+} one-qubit gates, and two $cNOT$ 2-qubit gates.

5.2 Physical implementation of quantum gates

In principle, any ensemble of two-level, distinguishable and interacting quantum systems is a candidate for the realization of a quantum device for computing applications. But since we are interested to the implementation of quantum gates in diamond solid-state devices, we will focus on the interaction between one or two

photons in a micro-cavity and a point defect whose relevant level structure is of Λ type, strictly analogue to that of the negative nitrogen-vacancy center (NV^-) which is the most studied color center for quantum computation applications, due to its favorable characteristics of phase-stability of the two lower levels ($|a\rangle$ and $|b\rangle$ in Fig.5.3) separated by about 2.9 GHz, and to the high dipole moment of the transition to the excited state $|e\rangle$, at 637 nm wavelength. Information can be encoded by photons in several different ways. Two orthogonally polarized modes p_a and p_b at the same frequency can serve as the two possible states of a same qubit, in this case $|0\rangle = |1_a 0_b\rangle$ and $|1\rangle = |0_a 1_b\rangle$. On the other hand, the 0 and the 1 population level of each mode can serve as well, in a way that the two modes can support two qubits. In the latter case the four computational base states are $|0_a 0_b\rangle$, $|0_a 1_b\rangle$, $|1_a 0_b\rangle$ and $|1_a 1_b\rangle$. It is also possible to pass from one coding to another arranging suitably cavities and defect centers, in a way to make them communicate by means of photons whose propagation directions have definite orientations respect to the defect axes.

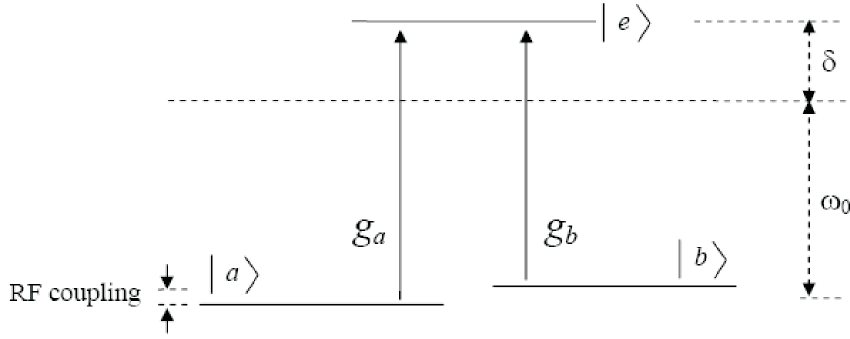

Figure 5.5: Cavity-atom interaction scheme for a Λ atomic system. The ground state is splitted in two states $|a\rangle$ and $|b\rangle$, separed by a RF energy much less than the cavity resonance frequency ω_0, which is de-tuned from the transition energy of an amount δ. g_a and g_b are the coupling constant between two ortogonal modes of the cavity and the two transitios $a - e$ and $b - e$, respectively.

We will study the interaction between a Λ point defect and a system of one or two differently polarized photons p_a and p_b, each one inducing a different transition, $|a\rangle \to |e\rangle$ or $|b\rangle \to |e\rangle$. We will assume that the ground state level can be prepared, with radio-frequency stimulation, in the mixed state $|\theta\rangle = \cos\theta|a\rangle + \sin\theta|b\rangle$. The Jaynes-Cummings Hamiltonian of the interaction H_{JC}, in the base given by $|0_a 0_b \theta\rangle$, $|1_a 0_b \theta\rangle$, $|0_a 1_b \theta\rangle$, $|0_a 0_b e\rangle$, $|0_a 1_b e\rangle$, $|1_a 0_b e\rangle$, $|1_a 1_b \theta\rangle$, has a block diagonal form of kind

$$H_{JC} = \left(\begin{array}{c|c|c} H_1^{1\times1} & \mathbf{0}^{1\times3} & \mathbf{0}^{1\times3} \\ \hline \mathbf{0}^{3\times1} & H_+^{3\times3} & \mathbf{0}^{3\times3} \\ \hline \mathbf{0}^{3\times1} & \mathbf{0}^{3\times3} & H_-^{3\times3} \end{array} \right); \tag{5.18}$$

whose significant blocks are the following ones:

$$H_1^{1\times 1} = -\delta; H_\pm^{3\times 3} = \begin{pmatrix} \mp\delta & 0 & g_a\cos\theta \\ 0 & \mp\delta & g_b \sin\theta \\ g_a\cos\theta & g_b\cos\theta & \pm\delta \end{pmatrix}; \tag{5.19}$$

where δ is the de-tuning and $g_{a,b}$ are the photon-atom coupling constants. The evolution operator of the system, directly obtained by exponentiation of $-iH_{JC}t$, can be also decomposed in block diagonal form, resulting $U_1^{1\times 1} = e^{i\delta t}$ and

$$U_\pm^{3\times 3} = \tag{5.20}$$

$$\begin{pmatrix} \alpha^2\left(\cos\Omega t \pm \widehat{i}\frac{\delta}{\Omega}\sin\Omega t\right) + \beta^2 e^{\pm\widehat{i}\delta t} & \alpha\beta\left(\left(\cos\Omega t \pm \widehat{i}\frac{\delta}{\Omega}\sin\Omega t\right) - e^{\pm\widehat{i}\delta t}\right) & -\widehat{i}\frac{g_a\cos\theta}{\Omega}\sin\Omega t \\ \alpha\beta\left(\left(\cos\Omega t \pm \widehat{i}\frac{\delta}{\Omega}\sin\Omega t\right) - e^{\pm\widehat{i}\delta t}\right) & \beta^2\left(\cos\Omega t \pm \widehat{i}\frac{\delta}{\Omega}\sin\Omega t\right) + \alpha^2 e^{\pm\widehat{i}\delta t} & -\widehat{i}\frac{g_b\sin\theta}{\Omega}\sin\Omega t \\ -\widehat{i}\frac{g_a\cos\theta}{\Omega}\sin\Omega t & -\widehat{i}\frac{g_b\sin\theta}{\Omega}\sin\Omega t & \cos\Omega t \mp \widehat{i}\frac{\delta}{\Omega}\sin\Omega t \end{pmatrix};$$

where $\alpha = \frac{g_a^2\cos^2\theta}{g_a^2\cos^2\theta + g_b^2\sin^2\theta}$, $\beta = \frac{g_b^2\sin^2\theta}{g_a^2\cos^2\theta + g_b^2\sin^2\theta}$ and $\Omega = \sqrt{g_a^2\cos^2\theta + g_b^2\sin^2\theta + \delta^2}$.

The evolution operator U, by suitable choice of the parameters, can perform the fundamental transformations both on one-qubit and on two-qubits states. If we consider the states $|10\theta\rangle$ and $|01\theta\rangle$ as the one-qubit states $|0\rangle$ and $|1\rangle$ relative to orthogonal polarizations of a same photon, we realize by inspection of the mathematical transformation U that the block $U_+^{3\times 3}$ acts on the subspace generated by $|10\theta\rangle$, $|01\theta\rangle$ and $|01e\rangle$. But if the product between Rabi frequency and time is chosen in such way that $\Omega t = k\pi$, U is closed respect to the space spanned by the 1-qubit state, having the expression (with, say, k even)

$$U_{1\text{ qubit}}(\alpha,\beta,\delta t) = \begin{pmatrix} \alpha^2 + \beta^2 e^{\widehat{i}\delta t} & \alpha\beta\left(1 - e^{\widehat{i}\delta t}\right) \\ \alpha\beta\left(1 - e^{\widehat{i}\delta t}\right) & \beta^2 + \alpha^2 e^{\widehat{i}\delta t} \end{pmatrix}; \tag{5.21}$$

It is easy to verify that $U_{1\text{ qubit}}\left(0, 1, \frac{\pi}{4}\right) = T$ and $U_{1\text{ qubit}}\left(\sin\left(\frac{3}{8}\pi\right), \cos\left(\frac{3}{8}\pi\right), \pi\right) = H$. Thus, it is possible to build the fundamental 1bit quantum gates (among many others) by suitable preparation of the atomic state (via the angle θ) and the product between detuning frequency and sampling time.

On the other hand, the presence or the absence of a photon in each of the two possible polarization states can be seen as values of a 2-qubits registers. In this case, the states $|00\theta\rangle$, $|01\theta\rangle$, $|10\theta\rangle$, $|11\theta\rangle$ constitutes the computational basis of the 2-qubits gate. In general, $U_1^{1\times 1}$ and $U_\pm^{3\times 3}$ mix these states with the others of the representation, but if $\Omega t = k\pi$, the space spanned by the computational basis is

closed respect to the evolution operator, whose expression on this basis is:

$$U_{2\text{ qubit}}(\alpha,\beta,\delta t,k)=\begin{pmatrix} e^{i\delta t} & 0 & 0 & 0 \\ 0 & \alpha^2+\beta^2 e^{i\delta t} & \alpha\beta\left(1-e^{i\delta t}\right) & 0 \\ 0 & \alpha\beta\left(1-e^{i\delta t}\right) & \beta^2+\alpha^2 e^{i\delta t} & 0 \\ 0 & 0 & 0 & (-1)^k \end{pmatrix}. \tag{5.22}$$

Now, if k is odd, we have that $U_{2\text{ qubit}}(0,1,2l\pi,2n+1)$ is a controlled-Z operator, where $Z=|0\rangle\langle 0|-|1\rangle\langle 1|$, by which a *cNOT* operator can be easily obtained composing with two Hadamard gates in this way $cNOT=(I\otimes H)cZ(I\otimes H)$. It is conclusively proved that a Λ-type atomic system in a 1-2 photons cavity can perform any fundamental quantum logic operation if parameters are suitably controlled.

5.3 Diamond and quantum computation

I have just proved that an atomic system in a one-two photons cavity can perform the fundamental logical operations on quantum bits. Now I'll show why color centers in diamond, particularly the negative nitrogen-vacancy complex NV^-, is so actractive for the implementation of a quantum gate.

It has been shown that the minimum switching time for a logical operation to be performed is of the order of Ω^{-1}, where the Rabi frequency Ω is, in energy units, substantially equal to the coupling strenght g between the field and the atom. In SI units, and for a cubic cavity, we would have: $g=e\langle r\rangle\sqrt{\frac{\hbar\omega_0}{2\epsilon V}}$, where $e\langle r\rangle$ is the dipole moment of the transition, ω_0 is the cavity pulsation, V is the cavity volume and ϵ is the dielectric constant. In order to the operation to be performed, the switching time has to be much shorter than the mean lifetime of the photons in the cavity, which is of order Q/ω_0, where Q is the quality factor of the cavity. By comparison, it is found that the inequality

$$\frac{Q}{V^{1/2}}\gg\frac{\sqrt{2\epsilon\hbar\omega_0}}{q\langle r\rangle}, \tag{5.23}$$

has to hold. Equally important, the coherence time of the atomic states has to be much higher of the photon mean lifetime too, since the operation to be performed is specified by a precise determination of the superposition of the atomic states.

Now, the NV^- center, arguably the most studied color center in diamond for quantum computing application, fits both these requirements remarkably well, for the following reasons:

- The ground state is a triplet, which means that, otherwise from other color centers in solid, the coherence time is not limited by the lifetime of the elec-

tronic level. Moreover, the null magnetic moment of the most abundant carbon isotope makes the coherence time of the m=0 and $m = \pm 1$ sublevels as long as milliseconds at room temperature [85, 86, 101].

- From the dipole moment of the transition at $\lambda_0 = 637$ nm [87], $\langle r \rangle$ can be estimated to about 2.3×10^{-8} cm, which is very long. The NV$^-$ centers share this property with other very intense luminescent centers like Nickel complexes[88], chromium [89] and silicon [90]. Taking into account a cavity volume $V \approx (\lambda_0/n)^3 = 1.85 \times 10^{-14}$ cm^3, such a high dipole moment limits the minimum quality factor to about 8700. It is a quite reasonable limit, considering that theoretical calculations with photonic crystal slab cavities give from $Q = 10^6$ to $Q = 10^7$ [102] and that experiments performed on nanocrystalline diamond slabs (highly absorbent) give values of Q as high as 585[103].

The valididty of the NV$^-$ centers as candidates for quantum computing applications has been recently demonstrated by an impressive series of results obtained in proof-of-principle experiments performed in bulk single crystal with dispersed color centers [104, 105, 106, 107], and a significant effort is being devoted to optimize the fabrication of optical structures to integrate single color centers in scalable devices. Different architectures are under development with this scope, ranging from the fabrication of all-diamond structures in monocrystalline [108, 92, 93, 94, 95, 96], polycrystalline [97] or nanocrystalline [103, 98] substrates, to the interfacing of diamond color centers to hybrid devices [109, 110, 111].

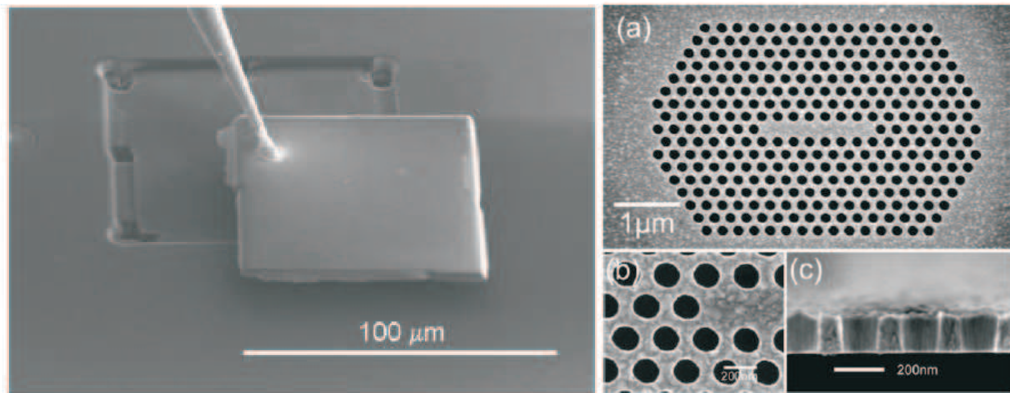

Figure 5.6: (left) SEM image of a diamond membrane obtained by ion beam graphitization of a buried layer, followed by focused ion beam cutting and graphite etching[108]. (right) (a) A SEM image of a suspended photonic crystal cavity in nanocrystalline diamond. (b) An enlarged picture of air holes. (c) A cross sectional image of the air holes. The thickness of the membrane is about 160 nm.[103]

On the other hand, pointlike defect manipulation presents difficulties, only some of whom are avoidable in principle. For the creation of highly localized single NV centers in diamond two methodologies are available. The first rely on the creation of vacancies by ion or MeV electron implantation in a relatively nitrogen-rich diamond, followed by annealing with subsequent diffusion of the vacancies which eventually bind themselves to pre-existing substitutional nitrogen centers. 30 KeV gallium focused beams have been employed in Ib-diamond, obtaining 15 nm-deep, single NV centers with a lateral resolution of about 180 nm. Another technique is based on direct implantation of nitrogen ions,at a very low implantation rate, in almost nitrogen free diamond, followed by annealing in order to make the vacancies created in the implantation process diffuse and finally bind themselves to the implanted nitrogen. With this method, single NV centers were created, about 1 μm under the surface of diamond, with a lateral resolution of about 0.3 μm[112] and with an efficiency ratio color-centers to implanted nitrogen approaching one. Optimally annealing can be performed to maximize the total Yield of NV^-[113].

Even if the creation of single color centers in a specific position into a diamond resonant cavity seems to be feasible, the NV center itself can have four different orientations in space. Hence, any architecture based on this color centers must incorporate defect-tolerant manifacturing approaches, having to cope with a maximum yield of specifically oriented NV centers of 1/4.

An interesting architectural strategy is illustrated by Tomljenovic in ref.[102]. Here I report the principle in some detail, because it makes clear how a precise modulation of diamond refractive index can serve to the design of diamond based photonic modules. A photonic crystal slab (PCS), with a photonic band-gap modulated in a way to include the 637 nm zero-phonon line of the NV^- luminescence, presents two defect lines (see Fig.5.7, left) : the first one (Bus line) is designed for distributing photons and effecting nonlocal cavity-cavity coupling, in the second one single NV centers are implanted in specific locations. After determination of the centers which have the desired orientation respect to the PCS axes, a resonant cavity is realized around them by ion implantation of two areas at the two opposite sides of the center (see Fig.5.7, top right), in a way that the refractive index of the irradiated diamond is lowered respect to pristine diamond. The assumption that refractive index lowers after implantation, at least in some range of fluence, is critical for the feasibility of the device, and will have to be throughly discussed in the following chapter.

The cavity realized in this way works according to the following principle: the two low-refractive index slides provides lateral confinement and propagation of light along the z direction ((see Fig.5.7, right)), the photonic crystal structure, on the other hand, prevents propagation in the z direction and makes the light to reflect forth and back on the “wall” of the cavity. In figure 5.7, bottom right, the major

electric field component, E_x, in the middle of the slab.

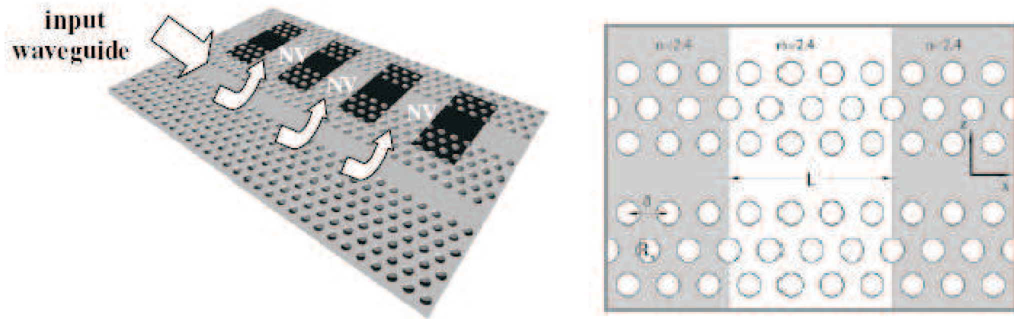

Figure 5.7: (left) Concept for heterostructure cavity array coupled to a common control line[102]. (right) Schematic of the PCS considered here with a step-index profile. The undamaged region in the centre has the largest refractive index, whilst damage reduces the refractive index in the surrounding regions, defining the cavity.

The quality factors obtained with this kind of structures ranges from the order of 10^6, with step index profiles, to 10^7, with graded index profiles obtainable either trough masking or with a suitably adjusted raster scanning of the irradiation area. These conclusions are affected by a considerable uncertainty due to absorption. In fact, even if most of the field in confined in the undamaged region (see Fig.5.7, bottom right), the part extending in the modified diamond can suffer attenuation if ion damage affects the extinction coefficient of diamond. In figure 5.8 the degradation of the quality factor with increasing extinction coefficients is shown for a step index profile, from which is clearly apparent the necessity of a good control of this essential parameter. Only a few works were dedicated to the study of diamond optical properties modifications induced by ion implantation [114, 115]. These studies were performed with carbon ions in the range 0.02-1.5 MeV, with a dependence of the results on the ion energy not clearly distinguishable. The requirement of damage uniformity along the implantation direction, for this kind of device, suggest the employment of much lighter ions, as hydrogen or helium, for whom no data is available in literature. Part of the work of our collaboration was addressed to the clarification of this essential point, as will be seen in the following chapter.

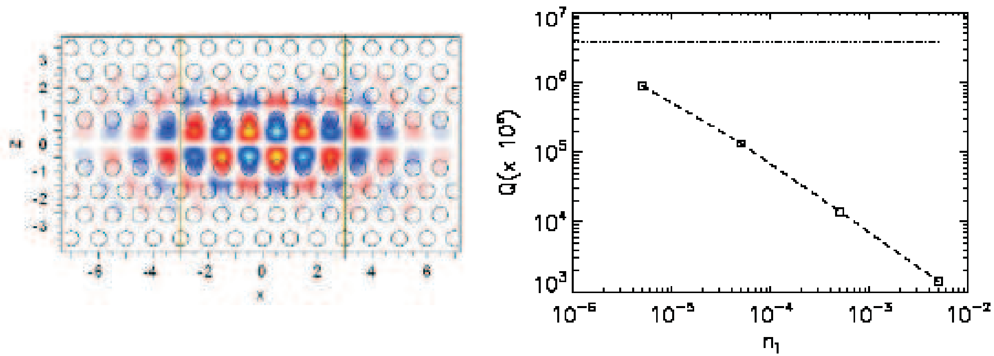

Figure 5.8: (left) The major electric field component, E_x, in the middle of the slab. (right) Total Q as a function of the imaginary part of the refractive index for the step-profile.

Chapter 6

Optical properties of proton damaged diamond

The attracting properties of some very intense color centers in diamond for application in photonic devices has been extensively dealt with in the previous chapter. With the aim of exploiting these features, several diamond micro-fabrication methods are currently under study [92, 93, 103, 108, 98]. These methods promise to offer a viable path towards the integration of monolithic photonic devices while exploiting the broad-band transparency and high refractive index of this material. Such methods are often based on the employment of ion-beam microfabrication strategies[92, 103, 108] therefore uncontrolled variations of the refractive index due to structural damage during the device fabrication process must be avoided (or predicted) with the highest accuracy. Moreover, in order to fabricate photonic devices in bulk diamond, the low-contrast refractive index modulation, induced by ion implantation, instead of merely being a side effect, could play an active role in the design of the device. Particularly, there is a strong interest for the investigation of the optical properties of diamond at very low implantation fluences: if the slight decrease in refractive index at low damage levels, found in C-implanted diamond[115], could be confirmed for lighter and more penetrating ions, an useful tool in the fabrication of ultra high-Q photonic crystal cavities would be disposable[102]. In any case, a suitable control of the optical properties of damaged-diamond is demanded also in a broad range of more conventional micro optics applications, such as high-power laser windows and lenses, optical MEMS, optical data storage, etc.[91, 116, 117, 118] The effect of ion-beam induced structural damage on the refractive index in diamond has been observed since the 60's[114] and qualitatively reported in the following literature[119]. In spite of this, remarkably, only few works were devoted to the systematic investigation of the optical effects of ion damage[115]. One example is reported in ref.[119], where carbon ions of different energies (50 keV 1.5 MeV)

were successively implanted in the same area, in order to produce a homogeneous damage profile over a depth of 1 μm; the refractive index was then measured on the as-implanted samples as a function of the implantation fluence, by means of reflectometric methods. In ref.[120] an ellipsometric study is reported in which the refractive index is measured from heavily damaged buried graphitic layers produced in diamond with 350 keV He^+ ion irradiation. Monoenergetic implantations with MeV light ions, such as hydrogen or helium, create damage profiles that are significantly different from those reported in the previous example, because they induce the formation of modified regions lying deeper under the diamond surface, whose characterization with reflectometric methods is much more difficult, due to the micrometric thickness of the overlying material. Nonetheless, the employment of MeV light ions can be an extremely versatile tool to locally modify the optical properties of materials with micrometric spatial resolution both in the lateral and depth directions, thanks respectively to the above-mentioned peculiar damage profile and to the possibility of focusing MeV ion beams at the micrometer scale with electromagnetic lenses. The strong potential of MeV ion microbeam implantation for direct writing optical structures has already been demonstrated in previous works in other materials of technological interest[121, 122], In our study, IIa monocrystalline diamonds grown by Chemical Vapor Deposition (CVD) were implanted with a scanning microbeam of 2 and 3 MeV protons[123], at fluences in the 10^{15} - 10^{17} cm^{-2} range. The damaged regions lie respectively 24 μm and 48 μm below the diamond surface and extend for a few (i.e. 2-4) microns. The resulting range of the damage levels induced in diamond, in term of vacancy density (6×10^{19}-3.5×10^{21} cm^{-3}), includes the densities of about 7×10^{20} cm^{-3} which are supposed to be related to a negative variation of the refractive index[115]. In order to measure the damage-induced variations of refractive index and absorption coefficient, an interferometric optical transmission microscopy technique and a space-resolved transmission spectroscopic setup were employed. The probe light wavelength was 632.8 nm, conveniently close to the zero-phonon-line emission of the NV center (637 nm), arguably the most widely investigated color center in diamond for applications in quantum optics. In order to obtain estimations of the variation of the real and imaginary parts of the refractive index as functions of the damage density, I developed a phenomenological model for the interpretation of the measurement of the optical path difference (OPD) and of the difference in absorption length (absorption length differences, ALD) between implanted and unimplanted regions. The model is based on the damage depth profile obtained with Monte Carlo SRIM simulations[124], and adopts an optical-geometric approximation, not taking into account the sharp variations in refractive index occuring into the damaged layers. In order to validate this approximation, the results of the model has been compared *a posteriori* with the predictions of a full multilayer numerical model of light propagation.

The employed samples are described in section 6.1.1, while section 6.1.2 is devoted to the description of the ion implantation process. In section 6.1.3 the measurement methods for the determination of the OPD and ALD are outlined, together with the measurement of the surface deformation (swelling) due to the expansion of the damaged regions[125, 126]. In section 6.2 the data analysis is presented, along with the description of the interpretation model, and the final results are presented in term of the dependence of the complex refractive index on the damage level, i.e. the density of vacancies produced by ion irradiation.

6.1 Experimental

6.1.1 Samples

This study was carried out on two 3.0×3.0×0.5 mm^3 single-crystal diamonds grown with Chemical Vapour Deposition (CVD) technique by ElementSix . The crystals consist of a single {100} growth sector and are classified as type IIa, with concentrations of nitrogen and boron impurities below 0.1 ppm and 0.05 ppm, respectively. The crystals are cut along the <100> axes and the two opposite faces of the samples are optically polished.

6.1.2 Ion implantation

The diamond samples were implanted at the external scanning microbeam facility of the LABEC laboratory in Firenze[127, 123], (Fig. 6.1). The diamond to be implanted mounted ouside the vacuum line, thus allowing its easy handling, positioning and monitoring [128]. Before hitting the target, the beam passes through a thin silicon nitride (Si_3N_4) membrane, 100 nm thick and 1×1 mm^2 wide (inset of Fig. 6.1), sealing the final part of the vacuum line, and 2 mm of unenclosed helium atmosphere. The extreme thinness of the Si_3N_4 window and the short external path in helium allow to minimize beam widening and energy straggling; as a result, a 10-20 μm spot size on sample is obtained, with 10 keV of energy straggling for MeV protons.

By means of a magnetic beam-scanning system, the position of the beam impact point on the sample can be controlled within a 1×1 mm^2 area, corresponding to the exit window aperture. Moreover, a multi-axis linear motorized stage of a 25 mm range provides high resolution translation of the sample on the x-y plane (normal to beam axis) under fixed beam, with a position reproducibility better than 1 μm. In the present work, proton beams were focused on the polished side of the

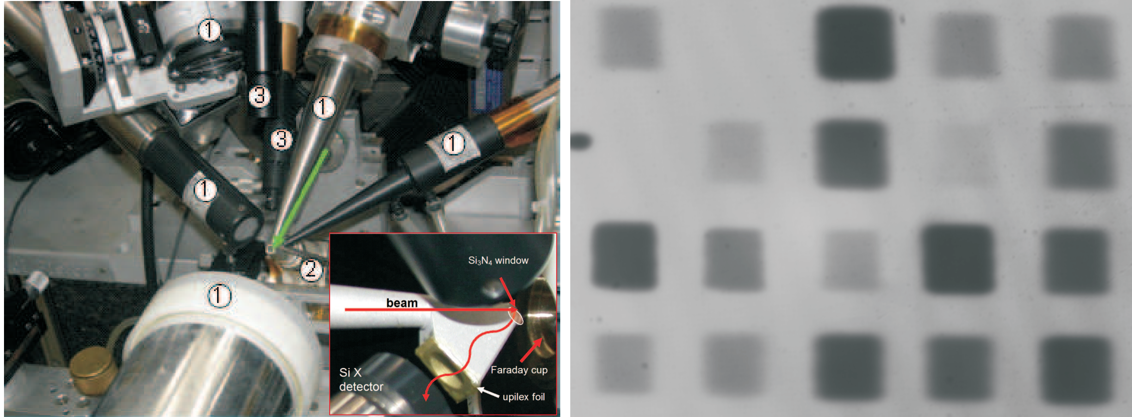

Figure 6.1: (left) End of the ion microbeam line: (1) detectors for Ion Beam Analysis (not used in this application) (2) X-ray detector for beam charge measurement, (3) vista camera and micro camera; the arrow indicates the ion beam direction. Inset: System for beam charge measurement. (right) Transmission optical image of several 125×125 μm^2 implanted areas. Progressive darkening of the implantation regions, along with fading of luminescence, allow a qualitative control of the implantation progress

samples on a spot of 10 μm (3 MeV) and 20 μm (2 MeV). Different regions of the samples were implanted at fluences ranging from 10^{15} cm^{-2} to 10^{17} cm^{-2}. For each implantation, the ion beam was magnetically scanned exploiting the same raster frame of 125×125 μm^2, much wider than the beam spot dimensions, in order to deliver a homogeneous fluence in the central region. During the implantations, fluences were determined by measuring the implanted charge (1) and setting the size of the irradiated area (2), as described hereafter.

1. Implanted charge: we used the beam charge measuring system installed at the LABEC microbeam, which exploits the yield of Si X-rays produced by the beam in the exit window[128]. The total charge implanted into the sample can be expressed as $Q_i = k \times A_{\text{X-Si}}$, k being a proportionality factor and $A_{\text{X-Si}}$ the number of Si X-rays counted by a dedicated detector, as reported in detail in ref.[128]. The calibration factor k was determined by measuring the ratio of the integrated charge (Q_i), collected with a Faraday cup surrounding the exit nozzle (Fig. 6.1(left)), to the Si X-ray yield ($A_{\text{X-Si}}$). In the whole explored range of beam currents (0.2 - 1.5 nA), k remained constant within 1%. As a result, the overall precision on the implanted charge determination is ≈1%, being the statistical error related to the Si X-rays counting typically well below 1%. Possible systematic errors in the charge determination, can amout to a 10% variation, commont to all the experimental points.

2. On-line setting of irradiated area: In order to implant the ions in areas with controlled dimensions, we calibrated the magnetic displacement of the beam on the sample surface by exploiting a standard TEM Cu grid. The uncertainty on the scanned area, which is basically due to the calibration procedure, is ≈5%. After ion implantation, the size of the irradiated area was measured on the OPD maps as described in Section III, thus improving the precision on the area determination up to ≈2% .

The visual aspect of the sample after the process is shown in figure 6.1(right). It is apparent the darkening due to ion damage of the implanted areas.

6.1.3 Optical characterization

In order to evaluate the variation of the refractive index due to ion-induced damage, the phase shift of a laser beam crossing the damaged diamond layer was determined using a commercial laser interferometric microscope (Maxim 3D, Zygo Corporation, Middlefield, CT, USA) with a 20× micro-Fizeau objective: the main characteristics of the system are reported in Fig.6.2, along with the scheme of the instrumental setup.

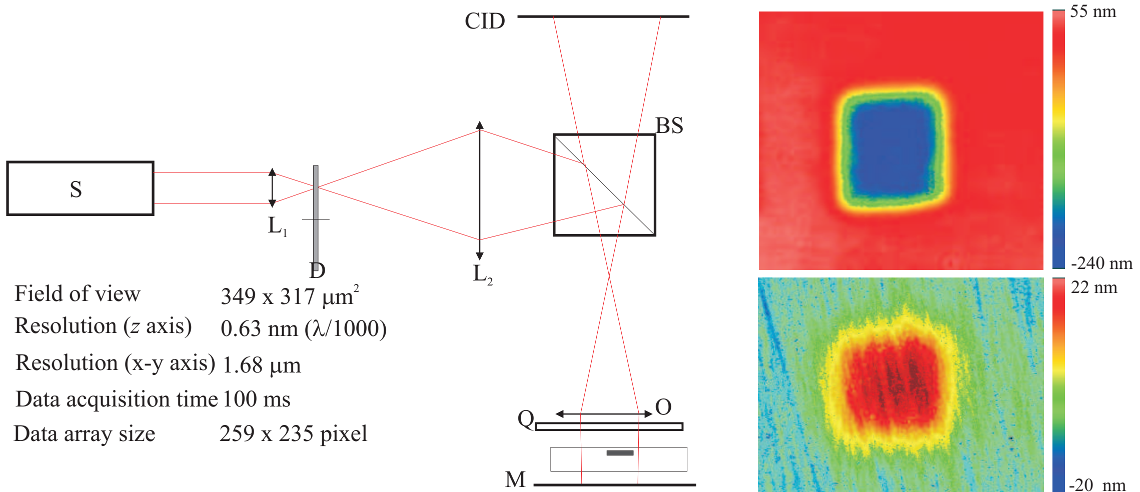

Figure 6.2: (Left) Scheme of the principle of measurement of the micro-interferometer Maxim 3D Zigo interferometer (see text for the explanation). (right top) Map of the OPD profile of an area implanted with 3 MeV protons at a fluence of 9×10^{16} cm^{-2} (right down) Map of the swelling profile of the same implantation.

The s-polarized light produced by a He-Ne laser source (S in figure 6.2) is focused by the lens L_1 on a diffuser disk (D), generating a spatially incoherent radiation

which is focused by L_2 on the back focus of the microscope objective O. After collimation, the radiation passes through the quarter-wave plate Q, whose last surface reflects back about 10% of the incident beam intensity. After double passage across the quarter-wave plate, the p-polarized reference-beam radiation passes through the polarizing beam splitter and illuminates the CID camera sensors. The test beam, after the double passage across the sample and the reflection on a high quality mirror M, produces an interference pattern on the plane of the sensors. The diamond is slightly tilted to avoid undesired internal reflections between the two opposite surfaces of the sample. A piezoelectric micro-actuator is able to displace the system of a distance $\lambda_{\text{He-Ne}}/8$ during 5 consecutive intensity measurements on the CID, so that a computerized system is able to reconstruct variation in the phase of the test beam in each pixel with an accuracy of about $2\pi/1000$ rad. The contributions of the beam splitter and the high-quality mirror is accounted for and removed.

Measuring the diamond in correspondence of an ion beam damaged layer it is possible to extract a microscopic map of the relative optical path difference (OPD) (Fig.6.2, right top). The measured OPD is caused mainly by the refractive index change of the damaged diamond with respect to the undamaged surroundings. There is also a smaller contribution (about 15% of the OPD (see fig 6.2 right) due to the expansion (swelling) of the highly damaged layer [126]. the latter was measured with a white light interferometric profilometer (Zygo NewView, see chapter 4 for further details). The swelling contribution to the OPD signal has been calculated and properly deconvoluted from the contribution arising from the variation of the sole refractive index, as reported in Section 6.2.1. Observing the maps of figure 6.2, the swelling and the OPD profiles have opposite signs: this is because swelling gives a shorter optical path in reflection, while damage produces a higher optical path in transmission measurements. The optical absorption at the irradiated zones was estimated by directly measuring their transmittance with a home-made set up for measurements with enhanced spatial resolution (see Fig.6.3 left). The light of a Xe-source is guided by a 5 μm optical fiber, forming a spot zone on the sample surface of $\approx$50 μm, which determines the spatial resolution of the system. Subsequently, the transmitted light is focused on a second optical fiber, connected to an Ocean Optics spectrometer SQ2000 with a spectral resolution of 0.8 nm and spectral range of 400-1200 nm. The finite spot size of the incident beam may obscure narrow spectral features if the transmittance varies very rapidly across the sample surface. However, from the OPD measurements, the implanted region results to be uniform within an area much wider than the beam spot, so that a spectral resolution of at least 1 nm is guaranteed, provided that the spectra is acquired in the minimum transmittance position, near the center of the implantation. A detailed description of the set up can be found elsewhere[129]. In the present work the absorption values were estimated at the same wavelength employed in the OPD measurement (λ_{laser} = 632.8nm).

Some full-spectrum transmission profiles of the irradiated samples are shown in Fig. 6.3, right.

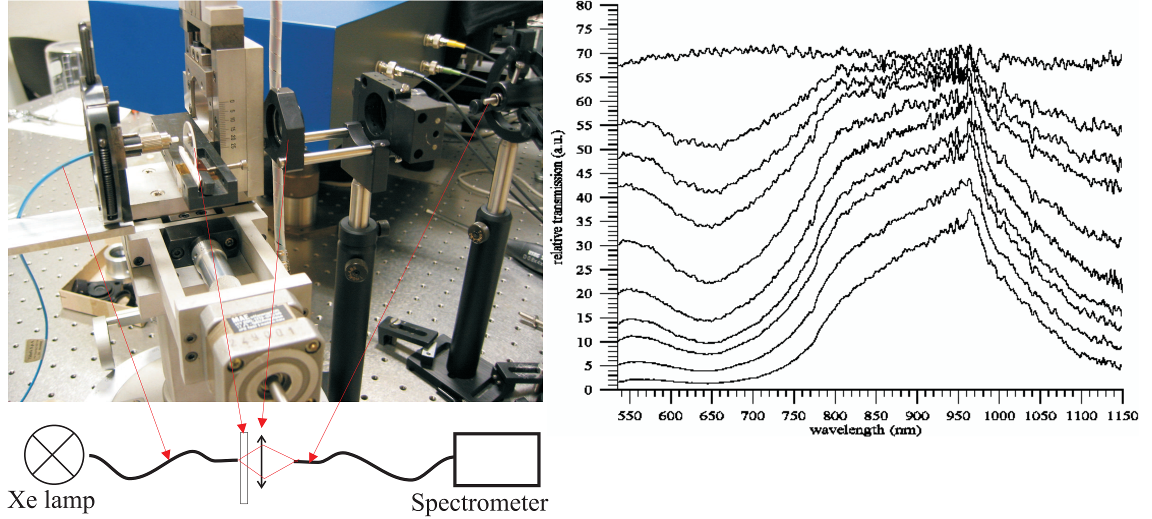

Figure 6.3: (Left) Scheme of the principle of measurement of the optical absorption. (right) some full-spectrum transmission profiles of the irradiated samples.

6.2 Data analysis

6.2.1 Dependence on fluence of the OPD and the ALD

The optical path difference between the center of the implanted area and the surrounding unimplanted region is estimated by the difference between the OPD mean value both in a central square region and in a frame region located respectively well inside and outside the irradiated area. The uncertainty of the OPD measurement, evaluated by the fluctuations of the phase inside and outside each region, is between 3 and 10 nm, which is predictably of the same order of magnitude of the roughness of the diamond surface (≈2 nm) multiplied by the refractive index difference between diamond and air at the probed wavelength ($\Delta n = 1.41$). The absorption length difference was evaluated, for each implantation, by the ratio between the transmittance T_0 of the un-implanted substrate, i.e. of the pristine diamond, and the value T measured at a chosen damaged area:

$$ALD = \frac{\lambda_{\text{He-Ne}}}{4\pi} \ln\left(\frac{T_0}{T}\right). \tag{6.1}$$

Both the OPD and the ALD measurements are affected by swelling, i.e., the expansion of the implanted material, which determines both a further phase shift of the probe laser beam and an additional absorption contribution. Nevertheless, since the gradient of the displacement of each layer in diamond $\frac{dz'}{dz}$, and the relative variation of refractive index $\frac{\Delta n}{n}$, are both small with respect to unity, it can be shown (see appendix B.1) that the values of OPD and ALD due to the variation of the refractive index alone can be obtained by the measured ones (OPD_m, ALD_m), by the simple equations:

$$\begin{aligned} OPD &= OPD_m - (n_0 - 1)\, h, \\ ALD &= ALD_m - k_0 h. \end{aligned} \tag{6.2}$$

were n_0 and k_0 are the refractive index and the extinction coefficient of undamaged pristine diamond and h is the swelling height. In our measurements, the product kh is exceedingly small (well below 0.1%) and its contribution has been neglected, but the product $(n_0 - 1)h$ amounts to about 15% of the measured OPD, and it has been properly subtracted. The fluence in the central region of each implantation has been calculated simply by the ratio of the deposited charge Q to the area A_Ω of the raster scanning area. In appendix B.2 I prove this approximation to be justified if the scanning is uniform and the dimensions L of the scanned area is much wider than the beam width l (in our case, L = 125 μm $\gg l$ = 10-20 μm). The charge Q is evaluated by means of the procedure outlined in section 6.1.2 with an accuracy of the order of 1%, while A_Ω is measured directly on the OPD maps by evaluating the number of pixels whose OPD is above the average value between the OPD inside and outside the implanted area. In this way, we verified the repeatability of the area setting to be much better than the calibration uncertainty obtained with the TEM Cu grid, allowing to keep the overall fluence uncertainty as low as about 3% . The variation of the optical depth and of the absorption length differences, extracted by the experimental data as illustrated before, reveals a clear correlation with the implantation fluence and ion energies, as shown in Fig.6.4.

6.2.2 Simulation of the ion damage

In order to extract, from the fluence dependence of the OPD and ALD, the refractive index variations with the ion-induced damage, we need a model which, for any given ion-energy and fluence, gives a physical quantity expressing the entity of damage at a given depth into the diamond. We assumed this quantity to be the induced vacancy density $\nu\,(z)$, admitting this parameter to bring all the essential information about the damage processes of a specific ion species and energy. We evaluated $\nu\,(z)$ numerically with the aid of Monte Carlo SRIM simulations[124] , averaged on ensembles of 50,000 ions, by setting the atomic displacement energy to 50 eV[130].

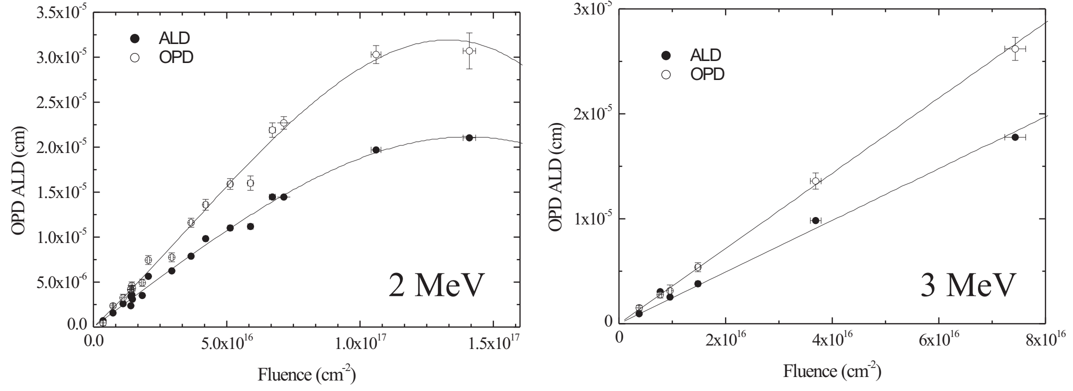

Figure 6.4: Experimental OPD and ALD as functions of the fluence, along with the best polynomial fit at 2 MeV (left) and 3 MeV (right).

The simulations give, for an ion of energy E, the number of vacances per unit length at a depth z as $p^E(z)$ (see Fig.6.5). Then, we calculated the induced vacancy density at a given fluence ϕ and energy E to be $\nu(z) = \phi \times p^E(z)$, under the assumption that non linear processes such as self-annealing, ballistic annealing and defect interaction could be disregarded. In fact, it has been shown that at damage densities that do not exceed the graphitization threshold (i.e. 10^{22} vacancies cm^{-3} for shallow implantations[131] and $6 - 9 \times 10^{22}$ vacancies cm^{-3} for deep implantations [132, 133], such an approach provides an adequate description of the ion-induced damage process in diamond in many respects[134].

6.2.3 Phenomenological model

We assume now the complex refractive index $\widehat{n} = n + ik$ to be directly determined by the vacancy density $\nu(z)$; under this assumption, we can consider the general polynomial expansions:

$$\widehat{n}(z) = \widehat{n}_0 + \sum_{m=1}^{\infty} c_m \times [\nu(z)]^m . \tag{6.3}$$

We make the assumption that the complex optical path difference $COPD$ between the irradiated and unimplanted areas is exclusively determined by the refractive index as follows:

$$COPD = \int_0^{\infty} [\widehat{n}(z) - \widehat{n}_0] \, dz, \tag{6.4}$$

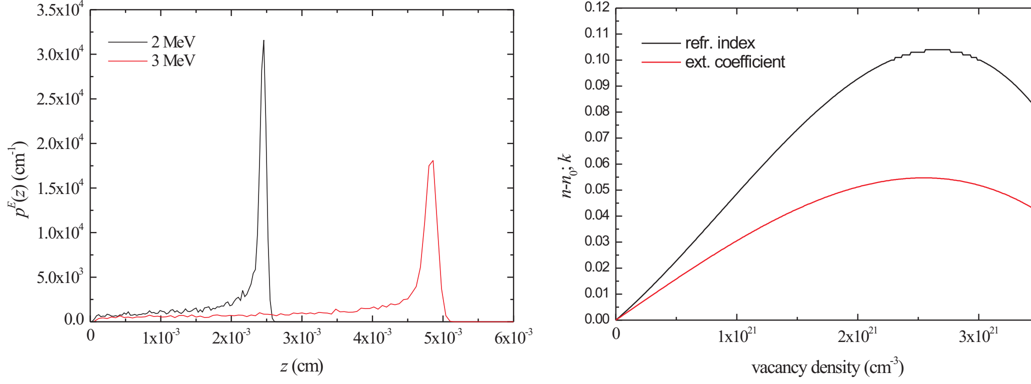

Figure 6.5: (right) Vacancy production per unit length, as a function of the penetration depth, for hydrogen ions at 2 and 3 MeV. (left) Variation of the real and the imaginary part of the refractive index as a function of the vacancy density

Table 6.1: Values of I_m^E coefficients for implantation of protons with energies of 2 and 3 MeV and m=1, 2, 3, as calculated by means of SRIM Monte Carlo simulations based on 50,000 events.

I_m^E (cm^{2m+1})	$E = 2$ MeV	$E = 3$ MeV
$m = 1$	7.06	8.62
$m = 2$	9.18×10^4	6.18×10^4
$m = 3$	2.24×10^9	8.59×10^8

thus neglecting internal reflections between adjacent differently damaged layers in diamond, and in general the interplay between the processes of refraction and absorption of the probe laser beam. This hypothesis will be validated a posteriori by means of a full multi-layer optical calculation, as described in the following section. From Eqs. 6.3 and 6.4 the complex optical path difference is given by :

$$COPD^E(\phi) = \sum_{m=1}^{\infty} c_m I_m^E \phi^m \quad \text{with} \quad I_m^E = \int_0^{\infty} \left[p^E(z)\right]^m, \qquad (6.5)$$

where the dependence from on ion energy and fluence has been highlighted. Since I_m^E can be numerically calculated from the known profile $p^E(z)$ for the two ion energies employed in the implantations (see Table 6.1), it is possible to fit the experimental OPD and ALD data with the real and the imaginary part of Eq. 6.5, by employing the fluence ϕ as independent variable and a convenient set of complex coefficients ($c_m = a_m + ib_m$) as fitting parameters.

Table 6.2: Values of a_m and b_m coefficients resulting from the polynomial fitting of the data relevant to 2 MeV and 3 MeV proton implantations.

$E = 2$ MeV	a_m (cm^{3m})	b_m (cm^{3m})
$m = 1$	$(4.0 \pm 0.2) \times 10^{-23}$	$(3.2 \pm 0.7) \times 10^{-23}$
$m = 2$	$(1.4 \pm 0.4) \times 10^{-44}$	$(0.02 \pm 0.04) \times 10^{-44}$
$m = 3$	$(-5.4 \pm 1.1) \times 10^{-66}$	$(-1.7 \pm 0.1) \times 10^{-66}$
$E = 3$ MeV		
$m = 1$	$(4.2 \pm 0.1) \times 10^{-23}$	$(2.9 \pm 0.1) \times 10^{-23}$

As shown, respectively, in Fig. 6.4, it is found that, for the 2 MeV proton implantations, the data are well fitted by a third-degree polynomial, while, at comparable fluences, the data relevant to 3 MeV proton implantation are fitted by a linear expansion. This difference is attributed to the fact that 3 MeV protons are subject to a more pronounced longitudinal straggling, thus creating thicker damaged layers, but with a lower defect density in comparison to 2 MeV proton implantations (see Fig.6.5). As a consequence, at a same fluence level, the 3 MeV implantations explore a more limited range of defect densities, allowing the dependence of the OPD and ALD on the fluence to be well represented by a linear function. Nevertheless, as reported in Table 6.2, the first degree coefficients of the 3 MeV implantations are compatible, within the uncertainties, with those of the 2 MeV ones, confirming that the linear parts of the two polynomials reflect a same dependence of the optical properties on the local damage. Once the c_m parameters are determined, the variation of the real and imaginary parts of the refractive index can be expressed as a function of the induced vacancy density employing the polynomial expansions reported in Eq. 6.4. In Fig. 6.5 (right) the resulting trends are plotted for the third degree polynomial whose linear term is determined on the basis of the two data sets (2 MeV and 3 MeV proton implantations), while the second- and third-order coefficients were evaluated from the first data set (2 MeV proton implantation). The range of vacancy densities of Fig. 6.5 extends up to the values corresponding to the highest damage level reached in our study.

6.2.4 Multi-layer model and validation of the phenomenological model

As mentioned above, Eq. 6.5 was derived under the assumption that the interplay between the processes of refraction and absorption of the laser probe can be neglected, and in particular that internal reflections due to the variation of the refractive index can be disregarded. In order to test this relevant assumption a posteriori, we elaborated a complete multilayer model describing the propagation of the

laser probe in diamond, thus considering all the processes of refraction and absorption associated with the variation of the complex refractive index in the implanted material. We considered a simulation grid identical to that of the SRIM simulation, with a constant vacancy density $\nu_i = \nu(z_i)$ $(1 \leq i \leq 100$, and a complex refractive index $\widehat{n}_i = \widehat{n}_0 + \sum_{m=1}^{\infty} c_m \nu_i^m$, adopting for the parameters c_i the values obtained in the preceding section by the fitting of the experimental data. Our purpose was to verify that the phase shift OPD and the attenuation distance ALD calculated with a full multilayer model do not differ significantly from those measured. To this aim, the normal propagation of a plane wave through the series of layers with complex refractive indexes $\widehat{n}_i$ was derived by setting, at the layers interfaces, the appropriate boundary conditions of continuity of the electric field and of its derivative, exactly in the same way shown in chapter 3. Hence, we calculated the complex expression of the waves crossing the sample, either in an unimplanted region or in a region implanted at a fluence ϕ . By comparing the amplitude and phase shift of the transmitted wave with the reference incident wave it is possible to estimate the values of the optical path difference and the absorption length difference, for each value of energy and fluence. The resulting estimations of $OPD^E(\phi)$ and $ALD^E(\phi)$ differ from the polynomial fits shown in figure 6.4 no more than about 1% . This value is well below the experimental errors, thus confirming, a posteriori, the correctness of the initial assumption of negligibility of the inter-layer reflections and more generally of the interplay of the refraction and absorption processes.

6.3 Discussion and Conclusions

The dependence of the refractive index and of the extinction coefficient on the damage produced in diamond by 2-3 MeV H ions has been studied in the fluence range 10^{15}-10^{17} cm^{-2}. Measurements indicate an increasing trend up to vacancy densities of about 2.5-3$\times 10^{21}$ cm^{-3}, then suggesting a decreasing behaviour at least up to the value of 3.5$\times 10^{21}$ cm^{-3}. For the refractive index, the decreasing trend as the graphitization conditions are approached is not surprising, being the refractive index of graphite less than that of diamond. We also note the similar and consistent behaviour of the real and the imaginary part of the refractive index, which was measured with completely unrelated methods. Interestingly, although the vacancy densities interval which we were able to scan, ranging from about 6×10^{19} to 3.5×10^{21} cm^{-}3, includes the damage levels referred to in ref.[115] for carbon ions in the energy range 0.05-1.5 MeV, no initial decrease in refractive index with respect to the undamaged diamond has been observed in our experiment. This could be due to different damage mechanisms produced by heavier ions and/or much lower energy levels. In any case, the suggestion of employing light MeV ions in order to obtain thick, uniform areas with a relatively low refractive index with respect to pristine

diamond[102] is not supported by our results. The methodology of measurements and analysis which we have adopted for this study is of ease and versatile use, being susceptible to be employed in any transparent material with very large ranges of energies and fluencies.

Chapter 7

Ion-beam writing of waveguides in diamond

In the last chapter, the influence of hydrogen MeV ions on the optical properties of diamond was throughly investigated. Particularly, an empirical relation between the induced vacancy density, taken as an index of the radiation damage and the variation of the complex refractive index of diamond was determined for the wavelength radiation of 633 nm, and it was proved to be valid at least for protons in the energy interval 2-3 MeV. The knowledge of such relation, along with the possibility of a suitable modeling of buried damaged regions under the diamond surface, by means of ion implantation, opens the way to the engineering of monolithic photonic devices in diamond.

Proton beam writing is a well established tool for micro-photonics applications, having been developed since the beginning of this decade in various laboratories[135, 136, 137]. The range of materials on which this technique has been applied includes polymers [138] and glasses [121]. Two fabrication routes are commonly followed using proton beam writing. The first involves the direct micromachining of the microoptical components, usually in polymer. This method may typically require some post-irradiation processing like resist development, additional coating steps or thermal treatment in order to make the final device or component. Surface relief gratings, microlens arrays, photonic crystal templates and waveguide cores are all fabricated using this method. The second route that can be followed involves ion beam modification of the material to form a region with a refractive index different from that of the bulk. This is the chosen method when using non-polymeric materials, which we demonstrated, in the previous chapter, suitable for diamond. In fact, all the methods employed so far in the micro-fabrication of diamond for photonic applications exploit the refractive index contrast between diamond and air, and rely on material ablation to create structures such as photonic cavities and

waveguides. Ion beam modification of bulk optical properties of diamond could offer unique opportunities for a more rapid prototyping of microphotonic devices, exploiting also a much lower refraction index contrast than that between diamond and air. Moreover, since the same methodology (with much higher irradiation doses) can be employed in diamond for fabrication of structure such as microfluidic channels, direct beam writing could open the way to microfluidic devices with integrated optics for biosensing applications (lab-on cells), with possibility of selective optical and chemical stimulation of single cells.

In this chapter I report on a method to create optical waveguides in bulk diamond by means of a 3 MeV proton beam, from which we obtained controlled increments of the refractive index in rectilinear, 500 μm-long, 12 μm-wide structures below the diamond surface, down to a depth of about 50 μm [139]. While, in other contexts, measurements of near field profiles are employed to calculate the refraction index modifications[121, 140], the work reported in the previous chapter permitted us to calculate the mode profiles on the base of the refractive index variation and to verify their adherence to the experimentally obtained mode shapes. These were observed using a micro-interferometric set up usually employed in optical pathlength measurements and previously described, in its main characteristics, in chapter 6; the phase maps obtained will be proved to be directly interpretable as superpositions of the previously calculated guided modes.

7.0.1 Experimentals: implantation and measurements

To perform this study, three adjacent faces of a $3.0 \times 3.0 \times 0.5$ mm^3 sample of type IIa single-crystal chemical-vapor deposited diamond, cut along the $\langle 100 \rangle$ axes, were optically polished down to a roughness of some nanometers, and then implanted at the external scanning microbeam facility of the LABEC laboratory in Florence[123] . The beam was focused on the small polished side of the sample to an approximately Gaussian spot of 12 μm width, and scanned along a rectilinear path perpendicular to the two polished faces of the largest size in order to obtain implantation fluencies of 2×10^{16}, 1×10^{16}, 5×10^{15}cm^{-2} in the central region, with an estimated uncertainty not exceeding 5% (see Fig.7.2 for a schematics of the implantation set-up). The as-prepared structures were then observed with a commercial laser interferometric microscope (Maxim 3D Zygo, Connecticut, USA, www.zygo.com) along the longitudinal direction of the guide. The setup used has been proven useful to characterize refractive index variations by observation of the phase shift induced by thin planar structures, in order to perform optical path difference (OPD) measurements. Here I claim it to be useful for a different kind of measurement, since the phase information of the field emerging from the narrow, long structures implanted in diamond (see fig.7.2)can give indication about the amplitude of the guided modes. For this

reason, it is useful to resume the principle of the measurement in relation to our purposes (see also Fig.7.1).

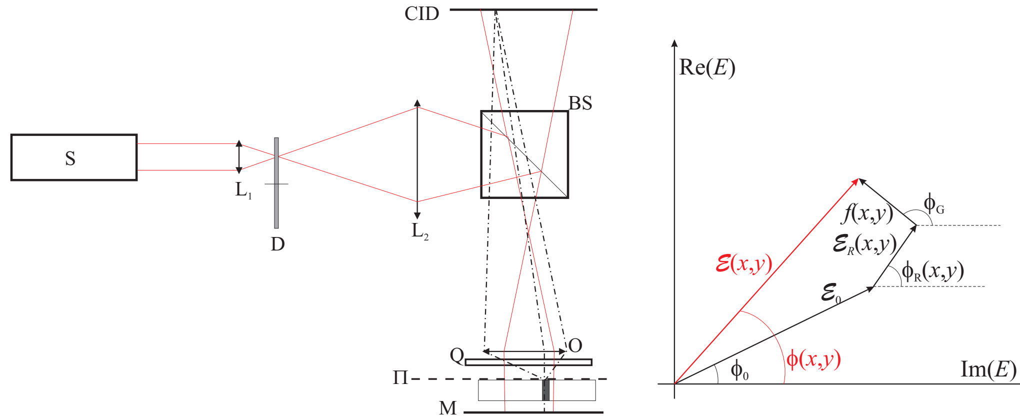

Figure 7.1: (left) Scheme of the principle of measurement of the micro-interferometer (see text for the explanation). (right) Scheme of the contribution to the overall electric field.

With reference to the description of the system in chapter 6 we only need to remind the fact that the objective O focuses on the plane of the CID camera sensor the light coming from the plane Π, at the upper surface of the diamond sample. That is, each pixel of the camera sensor registers the superposition of the plane wave reflected from the mirror M and of the image of the radiation coming from the plane Π, then forming the interference pattern with the radiation back-reflected by the beam splitter BS.

In figure 7.2 (left) an implantation scheme of the waveguides is drawn, pointing out the sample position, the implantation direction and the sight direction of the interferometer. The right side of the same figure reports an image of the interference pattern produced on the CCD plane by the 2×10^{16}cm^{-2} implantation, by two 1×10^{16}cm^{-2} and by three 5×10^{15}cm^{-2}implantations (from the left to the right). Fig. 7.3 represents the same areas in the false-color phase maps reconstructed by the computerized system of the instrument.

7.1 Intepretation of the phase maps

We show now that the phase maps obtained with the micro-inteferometer can be interpreted as a direct measurement of the amplitudes of the modes propagating along the guide. Let the electric field on the plane Π (in the polarization direction)

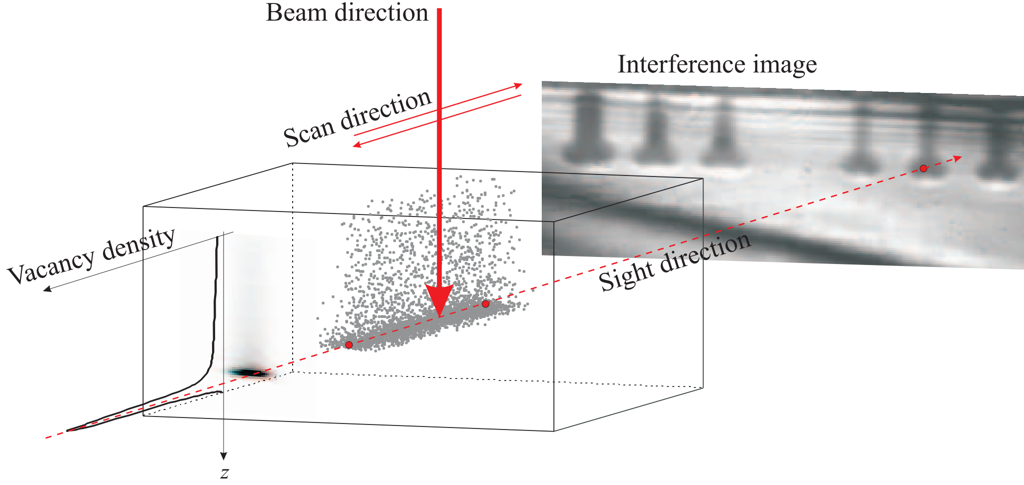

Figure 7.2: Scheme of the implantation geometry and interference pattern produced by the implantation at (from left to right) 2×10^{16}cm^{-2} fluence (one implantation), 1×10^{16}cm^{-2} (two implantations), 5×10^{15}cm^{-2} (the last three implantations).

be described by the real part of the function

$$E = \mathscr{E}\left(x, y\right) e^{i[\omega t + \phi(x,y)]}. \tag{7.1}$$

If the structures under consideration have a cross-sectional dimension comparable to that of the wavelength of the radiation, the radiation emerging from the diamond will be given by a principal plane-wave part plus a perturbation produced by the structures themselves. Consequently, the field on the plane Π will be given by the sum of three contributions: a principal part given by the back radiation reflected by the mirror M

$$E_0 = \mathscr{E}_0 e^{i(\omega t + \phi_0)}, \tag{7.2}$$

a secondary field deriving from the reflections on the surfaces of the sample, which is

$$E_R = \mathscr{E}_R\left(x, y\right) e^{i[\omega t + \phi_R(x,y)]}, \tag{7.3}$$

and a perturbation given by the contribution to the field of the structures under consideration. If the field can be considered as guided by the structures, this contribution can be simply written as

$$E_G = f\left(x, y\right) e^{i(\omega t + \phi_G)}, \tag{7.4}$$

were the function $f\left(x, y\right)$ is the amplitude map of the mode or a sum of different amplitudes maps.

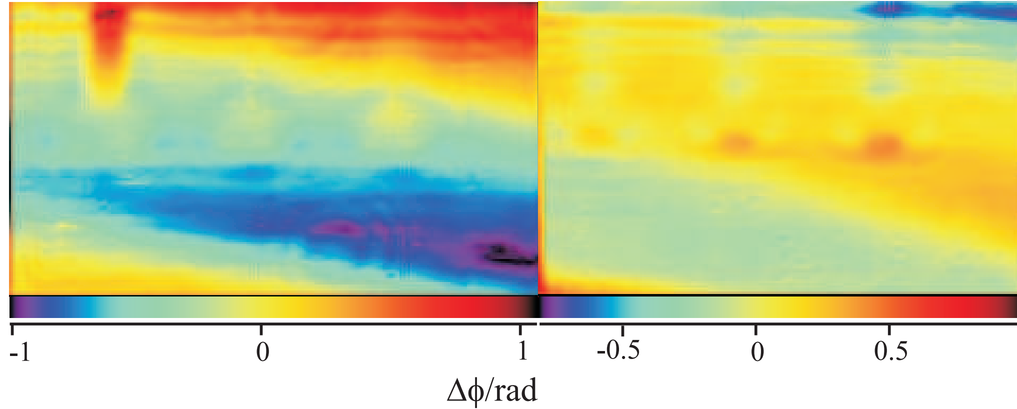

Figure 7.3: Phase maps corresponding to the same implantations of fig7.2.

If $\mathscr{E}_R$ and f are both small compared with $\mathscr{E}_0$, the phase difference $\Delta\phi = \phi(x, y) - \phi_0$, measured by the instrument, is given, at the lowest order, by:

$$\Delta\phi(x, y) = \frac{\mathscr{E}_R(x, y)}{\mathscr{E}_0} \sin(\phi_R(x, y) - \phi_0) + \frac{f(x, y)}{\mathscr{E}_0} \sin(\phi_G - \phi_0), \quad (7.5)$$

(see also Fig.7.1, right). Consequently, once the contribution of the reflections has been fitted and subtracted, the map of $\Delta\phi$ is simply proportional to the amplitude map of one of the modes which can propagate in the structure, or to a linear combination of several modes simultaneously propagating in the waveguide, each with its appropriate phase value ϕ_G.

7.1.1 Finite element modeling of the waveguides

In order to compare the experimental phase profiles with a superposition of modes propagating in the waveguides, a 2-dimensional finite element model (FEM) of the irradiated regions was employed, taking into account the local modifications in the refractive index induced by proton damage, quantified in terms of the induced vacancy density and calculated by means of a Monte Carlo simulation (SRIM) as reported in ref.[141]. Once given the vacancy density at every cell of the simulation grid, the local variation of refractive index at the He-Ne wavelength of 632.8 nm is calculated on the basis of the simple relation 6.3 [141], with the values of the parameters given in Tab. 6.2. The result is

$$\Delta n = (4.20 + 2.88i) \times 10^{-23} \frac{dN_{vacancies}}{dV/\text{cm}^3}. \quad (7.6)$$

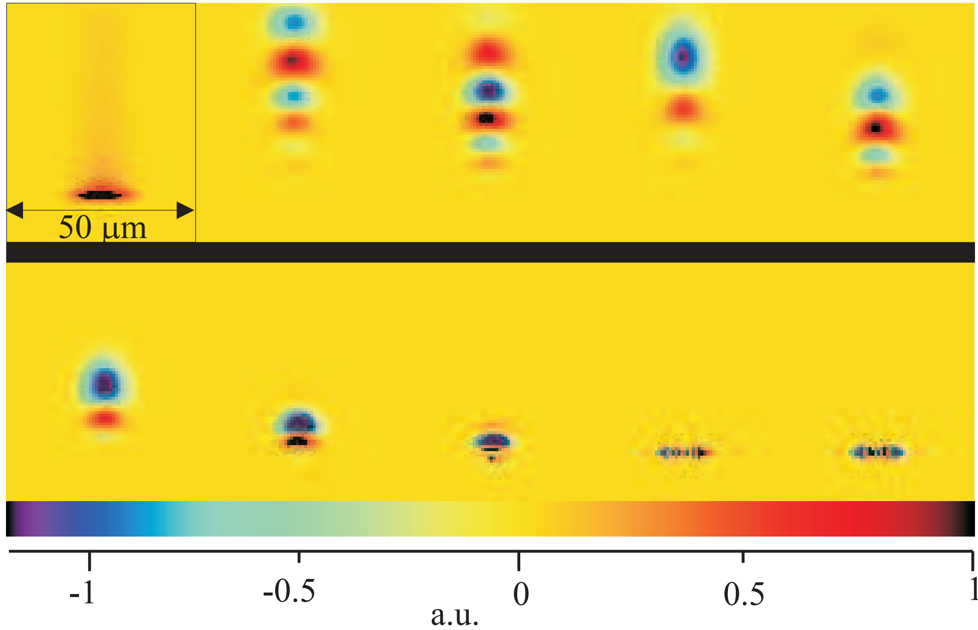

Figure 7.4: (top left) Map of the damage produced by the ion beam in term of vacancy density. (rest of the figure) In the same spatial scale, amplitude maps of 9 simulated modes propagating in the waveguide irradiated at $2 \times 10^{16}\text{cm}^{-2}$ fluence.

In figure 7.4 a map of the vacancy density, as calculated by SRIM, and an example of nine different numerically calculated modes propagating in the structures irradiated at the higher fluence are shown. At lower fluencies, progressively lower refractive index modifications imply a lower number of propagating modes, whose amplitude maps present fewer and wider lobes.

7.1.2 Fitting of the experimental maps

The experimentally obtained phase maps were compared with a superposition of the calculated amplitude maps, by fitting them with a linear combination of the propagating modes. Since the relative amplitudes of the modes excited in the waveguides depend in a sensitive way from the illumination conditions, different positions of the sample on the focal plane may imply different weights to be assigned at each particular mode. In figure 7.6 two different images of the implantations at fluencies of 2 and $1 \times 10^{16}\text{cm}^{-2}$ are shown along with the best fit obtained with 30 different propagation modes (ten for each structure) and two plane sinusoids, taking into account the reflections on the two planes. It is evident that the same set of propagation modes, though with different weights, fits the two images. The weight of each

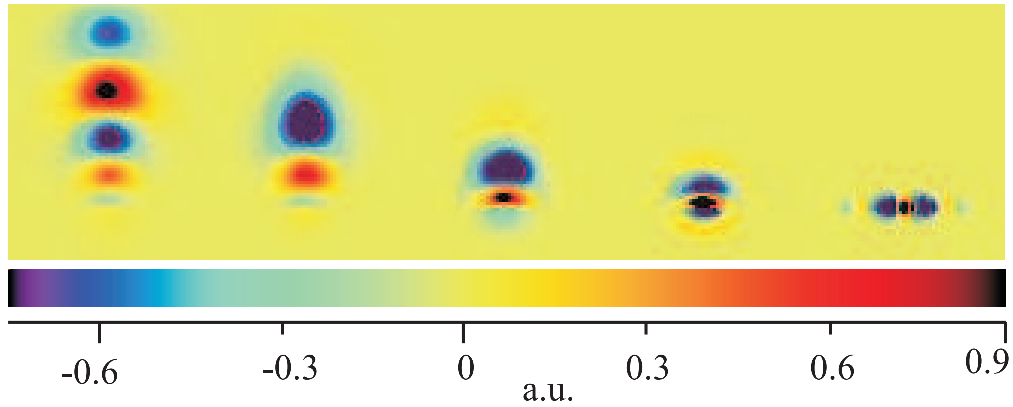

Figure 7.5: amplitude maps of 5 simulated modes propagating in the waveguide irradiated at $5 \times 10^{15}\mathrm{cm}^{-2}$ fluence.

mode is not of much significance, since it is proportional to the sinus of $\phi_G - \phi_0$, an angle which is supposed to vary randomly from a mode to another. In the same figure, an image of the $5 \times 10^{15}\mathrm{cm}^{-2}$ fluence waveguide is also shown, together with its 21-mode fit.

From the inspection of these images we conclude that the adherence of the fit to the experimental two-dimensional profiles is very good in the cap layer between 0 and about 45 μm in depth, where the relative damage is small, while at end-of-range the structures seems to be more diffuse, probably due to the distortion induced by diffraction on the highly opaque regions, which lies under the plane Π (see fig7.1), in correspondence with the considered structures.

7.1.3 Conclusions

There is sufficient evidence that the ion-beam writing method proposed in this letter gives the possibility to fabricate light-guiding structures in bulk diamond. Moreover, the micro-interferometric measuring method briefly exposed here provides a mean for a highly detailed study of the mode patterns propagating in the waveguides.

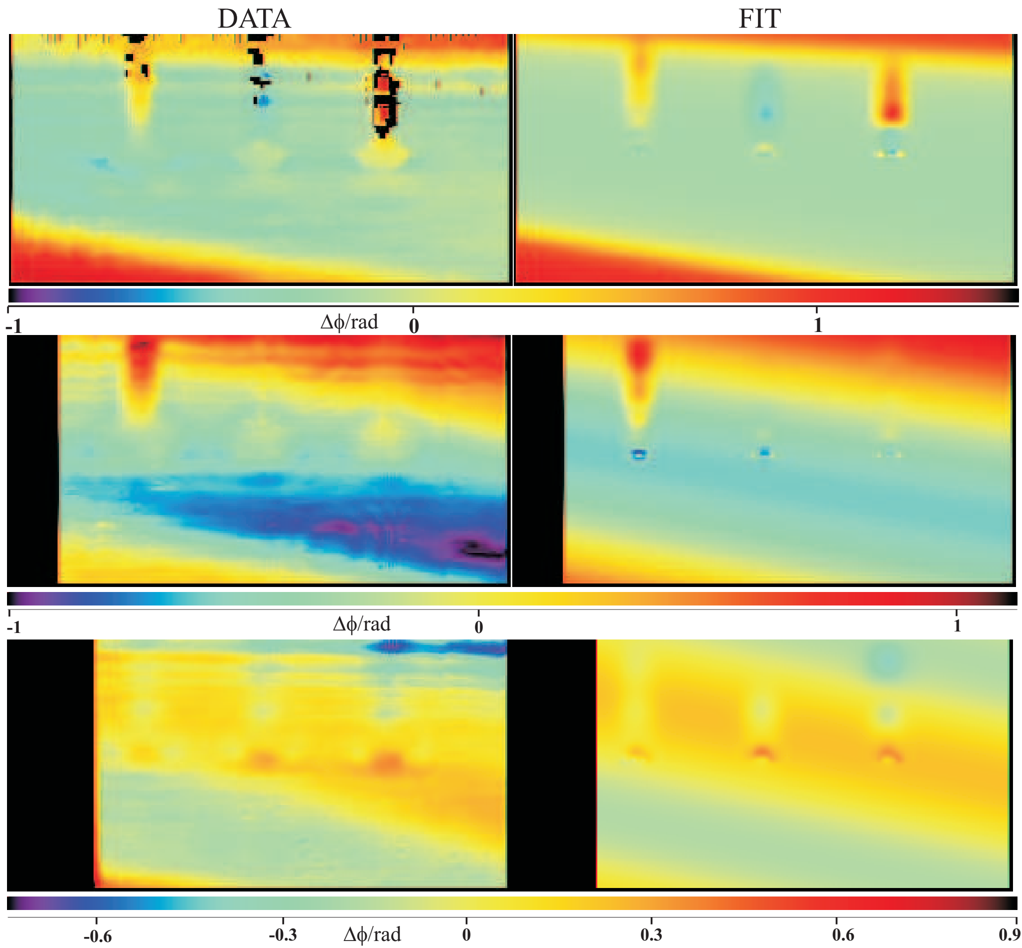

Figure 7.6: Comparison of the measured phase shift maps (left) and of the fit (right) obtained by linear superposition of modes amplitudes and a background taking into account multiple reflections effects. (top and middle) Images obtained from three adjacent guides irradiated at $2 \times 10^{16}\mathrm{cm}^{-2}$ (the left one) and at $1 \times 10^{16}\mathrm{cm}^{-2}$ (the onthers). (bottom) Images obtained by three equally irradiated guides at a fluence of $5 \times 10^{15}\mathrm{cm}^{-2}$.

Appendix A

Persson's theory of contact mechanics and applications

In this appendix Persson's theory of contact mechanics is exposed in the part regarding the calculation of the rate of contact between a rough, perfectly rigid surface and a flat elastic media. The theory is applied to the diamond surfaces studied in chapter 4 and a comparison is made with the results of the theory of section 4.2. Some weak aspects of Persson's theory are also evidenced and possible ways toward the solution of some difficulties are shown.

Consider a nominally flat surface of radius r_0 and area A_0, and let $r_\zeta = r_0/\zeta$ be the resolution with which the rough surface's profile $h(\mathbf{x})$ and the stress contact $p(\mathbf{x})$ are observed. If p_0 is the nominal surface stress on the area A_0 and p_ζ is the (average) stress on the effective contact area A_ζ at the resolution r_ζ, we have obviously

$$p_0 A_0 = p_\zeta A_\zeta, \tag{A.1}$$

so that the rate of effective contact $R(\zeta)$ is given by

$$R(\zeta) \equiv \frac{A_\zeta}{A_0} = \frac{p_0}{p_\zeta}. \tag{A.2}$$

The purpose of the theory is find an analytical expression for the rate of contact in dependence on the known quantities, essentially the surface profile $h(\mathbf{x})$ and the load p_0 on the nominal area A_0.

It is important to note that, up to now, the notion of "resolution" of the observation is yet matematically not well defined. Persson doesn't remove this ambiguity even in the more extensive presentation of the theory[36]. We will try to suggest a way to overcome this difficulty, underlining the passages were further

mathematical work should be done. We begin noting that stress $p(\mathbf{x})$ in a given point $\mathbf{x}$ is given by

$$p(\mathbf{x}) = \int \widehat{p}(\mathbf{q}) e^{i\mathbf{q}\cdot\mathbf{x}} d^2\mathbf{q}, \tag{A.3}$$

and defining the complex quantity

$$p_\zeta(\mathbf{x}) \equiv p_q(\mathbf{x}) \equiv \int_{|\mathbf{q}|<q_0\zeta\equiv q} \widehat{p}(\mathbf{q}) e^{i\mathbf{q}\cdot\mathbf{x}} d^2\mathbf{q}, \tag{A.4}$$

with $q_0 \equiv \frac{2\pi}{r_0}$. In this way, $q \equiv q_0\zeta$ is interpreted as a cut-off spatial wavenumber for the fourier analysis of our problem, dependent on the detail with which we are able to observe the phenomena involved. At this point $A_\zeta \equiv A_q$ can be defined as the the total area on which the real part of $p_q(\mathbf{x})$ is "significantly" greater than zero (the notion of "significance" is obviously yet non well defined) and saying that p_q is the average value of the real part of $p_q(\mathbf{x})$ on this area. We define also the area $A_q(p)$ on which the real part of $p_q(\mathbf{x})$ is greater than zero but lesser than p, so that it is possible to express the probability distribution $P(p,q)$ of having a pressure p on the area A_q as:

$$P(p,q) = \frac{1}{A_q}\frac{dA_q(p)}{dp} = \frac{1}{A_q}\int_{\Gamma_{q,p}} \frac{dl}{|\nabla \Re p_q(\mathbf{x})|}, \tag{A.5}$$

were $\Gamma_{q,p}$ is the 1-dimensional profile over which $\Re p_q(\mathbf{x}) = p$. Now we can express the mean value p_q as

$$p_q = \frac{\int_0^\infty pP(p,q)\,dp}{\int_0^\infty P(p,q)\,dp}, \tag{A.6}$$

and the rate of contact $R(q)$ as

$$R(q) = \frac{p_0\int_0^\infty P(p,q)\,dp}{\int_0^\infty pP(p,q)\,dp}. \tag{A.7}$$

It is worth noting that the distribution $P(p,q)$ is not normalized. To the aim of finding an expression for the rate of contact $R(q)$, we will determine a differential equation for the distribution $P(p,q)$. Let us start from equation A.5, and write

$$P(p,q) = \frac{1}{A_q}\int dp' \int_{\Gamma_p} \frac{dl}{|\nabla \Re p_q|}\delta(p-p') = \frac{1}{A_q}\int_{A_q} \delta(p - \Re p_q(\mathbf{x}))\, d^2\mathbf{x}. \tag{A.8}$$

If we consider a statistical ensemble of surfaces with similar characteristics, we can substitute the average on the area with an average over the ensemble, and write (from this point on it is understood the sign of real part before $p_q(\mathbf{x})$ and similar quantities):

$$P(p,q) = \langle \delta(p - p_q(\mathbf{x}))\rangle, \tag{A.9}$$

where $\mathbf{x}$ is whatever point of effective contact at the scale r_q. Now we can find a differential relation for the distribution P. We have

$$P(p, q+\Delta q) = \langle \delta(p - p_{q+\Delta q}(\mathbf{x})) \rangle = \langle \delta(p - p_q(\mathbf{x}) - \Delta p_{q,\Delta q}(\mathbf{x})) \rangle, \tag{A.10}$$

which can be re-written as

$$P(p, q+\Delta q) = \left\langle \int dp' \delta(p' - \Delta p_{q,\Delta q}(\mathbf{x})) \, \delta(p - p' - p_q(\mathbf{x})) \right\rangle. \tag{A.11}$$

Now, statistical independence of averages at different scales permits to infer, from this relation and from Eq.A.9:

$$P(p, q+\Delta q) = \int dp' \langle \delta(p' - \Delta p_{q,\Delta q}(\mathbf{x})) \rangle \, P(p - p', q). \tag{A.12}$$

Noting that

$$\langle \delta(p' - \Delta p_{q,\Delta q}) \rangle = \frac{1}{2\pi} \int dw \left\langle e^{iw\left(p' - \Delta p_{q,\Delta q}\right)} \right\rangle \approx \delta(p') + \frac{1}{2} \left\langle \Delta p_{q,\Delta q}^2 \right\rangle \frac{\partial^2}{\partial p'^2} \delta(p'), \tag{A.13}$$

we have finally, substituting in Eq.A.12, the following:

$$P(p, q+\Delta q) = P(p, q) + \frac{1}{2} \left\langle \Delta p_{q,\Delta q}^2 \right\rangle \int dp' P(p - p', q) \frac{\partial^2}{\partial p'^2} \delta(p'), \tag{A.14}$$

that is

$$\frac{\partial}{\partial q} P(p, q) = f(q) \frac{\partial^2}{\partial p^2} P(p, q), \quad \text{with} \quad f(q) = \frac{1}{2} \frac{\left\langle \Delta p_{q,\Delta q}^2 \right\rangle}{\Delta q}. \tag{A.15}$$

Equation A.15 is a diffusion type equation, in which the "temporal" coordinate is q and the "spatial" one is the stress p, with a diffusion constant dependent on q itself. The diffusion constant $f(q)$ is defined on the basis of a statistical ensemble of surfaces, on which the square of the (real part of the) difference $p_{q+\Delta q}(\mathbf{x}) - p_q(\mathbf{x}) \equiv \Delta p_{q,\Delta q}$ is averaged. The boundary conditions and the initial values for the equation A.15 are respectively

$$P(0, q) = P(\infty, q) = 0 \quad \text{and} \quad P(p, q_0) = \delta(p - p_0). \tag{A.16}$$

The solution of Eq.A.15, with the boundary and initial conditions A.16, can be straightforwardly verified to be

$$P(p, q) = \frac{2}{\pi} \int_0^\infty \sin(sp_0) \sin(sp) \exp\left[-s^2 \int_{q_0}^q f(q') \, dq'\right] ds. \tag{A.17}$$

This expression defines the dependence of the distribution $P(p,q)$ on the statistical characteristics of p_q.

Now, multiplying both terms of Eq.A.15 by p and integrating we have

$$\frac{\partial}{\partial q}\int_0^\infty pP(p,q)\,dp = -f(q)\left|P(p,q)\right|_{p=0}^{p\to\infty} = 0. \tag{A.18}$$

Thus

$$\int_0^\infty pP(p,q)\,dp = \int_0^\infty pP(p,q_0)\,dp = \int_0^\infty p\delta(p-p_0)\,dp = p_0. \tag{A.19}$$

On the other hand, integrating Eq.A.15 directly, we have

$$\frac{\partial}{\partial q}\int_0^\infty P(p,q)\,dp = f(q)\left|\frac{\partial}{\partial p}P(p,q)\right|_{p=0}^{p\to\infty} = -f(q)\frac{\partial}{\partial p}P(0,q), \tag{A.20}$$

which implies:

$$\int_0^\infty P(p,q) - \delta(p-p_0)\,dp = -\int_{q_0}^q f(q')\frac{\partial}{\partial p}P(0,q')\,dq'. \tag{A.21}$$

It follows, from Eqs.A.7,A.19 and A.21 that

$$R(q) = 1 - \int_{q_0}^q f(q')\frac{\partial}{\partial p}P(0,q')\,dq'. \tag{A.22}$$

Now, substituting expression A.17 it is easy to find that

$$\int_{q_0}^q f(q')\frac{\partial}{\partial p}P(0,q')\,dq' = 1 - \frac{2}{\pi}\int_0^\infty \frac{\sin(sp_0)}{s}\exp\left[-s^2\int_{q_0}^q f(q')\,dq'\right]ds, \tag{A.23}$$

which imply, changing the variable of integration:

$$R(q) = \frac{2}{\pi}\int_0^\infty \frac{\sin x}{x}\exp\left[-x^2\frac{1}{p_0^2}\int_{q_0}^q f(q')\,dq'\right]dx. \tag{A.24}$$

The solution of the problem requires, at this point, the determination of the function $f(q)$, defined in Eq.A.15, in dependence on the surface profile. First note that

$$\Delta p^2_{q,\Delta q}(\mathbf{x}) = \left(p_{q+\Delta q}(\mathbf{x}) - p_q(\mathbf{x})\right)^2 = \iint_{\substack{q<|\mathbf{q}|<q+\Delta q \\ q<|\mathbf{q}'|<q+\Delta q}} \widehat{p}(\mathbf{q})\,\widehat{p}(\mathbf{q}')\,e^{i(\mathbf{q}+\mathbf{q}')\cdot\mathbf{x}}d^2\mathbf{q}d^2\mathbf{q}' \tag{A.25}$$

Averaging over the whole area A_0 and over a statistical ensemble of surfaces we have, remembering $\int e^{i(\mathbf{q}+\mathbf{q}')\cdot\mathbf{x}d^2\mathbf{x}} = 2\pi\delta(\mathbf{q}+\mathbf{q}')$:

$$f(q) = \frac{1}{2}\frac{\left\langle\overline{\Delta p^2_{q,\Delta q}}\right\rangle}{\Delta q} = \frac{\pi}{A_0\Delta q}\int_{q<|\mathbf{q}|<q+\Delta q}\langle\widehat{p}(\mathbf{q})\,\widehat{p}(-\mathbf{q})\rangle\, d^2\mathbf{q}. \tag{A.26}$$

At this point we have to face the problem of determining a relationship between the Fourier components of the local pressure and the surface profile. If we assume that, at a given external pressure p_0, the elastic surface profile is $h_{p_0}(\mathbf{x})$, we can solve the problem exactly as we did in the perfect adherence case in section 4.2, in the no-friction and in the vertical-displacement case, writing $\widehat{p}(\mathbf{q}) = Jq\widehat{h}_{p_0}(\mathbf{q})$. Obviously, this assumption only transform the problem into that of the determination of the profile $h_{p_0}(\mathbf{x})$. Persson poses simply $h_{p_0}(\mathbf{x}) = h(\mathbf{x})$, stating an approximation which, in my opinion, is justified only in the limit $p_0 \to \infty$. In order to overcome this difficulty, it may be convenient to state that the surface profile of the elastic medium follows that of the rigid one "almost" exactly down to a resolution which depends itself on the ratio of uni-axial stress p_0 to the modulus J. In this case, The Fourier transform of the profile $\widehat{h}_{p_0}(\mathbf{q})$ obeys the relation:

$$\widehat{h}_{p_0}(\mathbf{q}) = \widehat{h}(\mathbf{q}) \times \Psi_{\frac{p_0}{J}}(q), \tag{A.27}$$

where the function $\Psi_{\frac{p_0}{J}}(q)$ can be an empirical function that operates a cut at frequencies which are increasing with the ratio $\frac{p_0}{J}$. With this assumption, the Persson's development of the theory results only slight modified: keeping in mind that

$$\left\langle\widehat{h}_{p_0}(\mathbf{q})\,\widehat{h}_{p_0}(-\mathbf{q})\right\rangle = \frac{\Psi^2_{\frac{p_0}{J}}(q)}{(2\pi)^4}\iint\langle h(\mathbf{x})\,h(\mathbf{x}')\rangle\, e^{-i\mathbf{q}\cdot(\mathbf{x}-\mathbf{x}')}d^2\mathbf{x}d^2\mathbf{x}' \tag{A.28}$$

$$\frac{\Psi^2_{\frac{p_0}{J}}(q)}{(2\pi)^4}\iint\langle h(\mathbf{x}+\mathbf{x}')\,h(\mathbf{x}')\rangle\, e^{-i\mathbf{q}\cdot\mathbf{x}}d^2\mathbf{x}d^2\mathbf{x}' = \frac{A_0\Psi^2_{\frac{p_0}{J}}(q)}{(2\pi)^4}\int\langle h(\mathbf{x})\,h(\mathbf{0})\rangle\, e^{-i\mathbf{q}\cdot\mathbf{x}}d^2\mathbf{x},$$

from Eq.A.26 we finally have

$$f(q) = \frac{1}{2}J^2q^3\Psi^2_{\frac{p_0}{J}}(q)\,C(q) \quad \text{with} \quad C(q) = \frac{1}{(2\pi)^2}\int\langle h(\mathbf{x})\,h(\mathbf{0})\rangle\, e^{-i\mathbf{q}\cdot\mathbf{x}}d^2\mathbf{x}. \tag{A.29}$$

Substituting Eq.A.29 in Eq.A.24 we find

$$R(q) = \frac{2}{\pi}\int_0^\infty \frac{\sin x}{x}\exp\left[-x^2\frac{1}{2}\left(\frac{J}{p_0}\right)^2\int_{q_0}^{q} q'^3\Psi^2_{\frac{p_0}{J}}(q')\,C(q')\,dq'\right]dx. \tag{A.30}$$

From this relation, it is evident that the rate of contact of the two surfaces depends on the ratio between the normal stress p_0 and the modulus J, of the order of the elastic

constants of the material, multiplyed by a factor which depends on the statistical characteristics of the rough surface and, via the factor $\Psi^2_{\frac{p_0}{J}}(q)$, on the pressure itself. In figure A.1 the rate of contact and its complement to 100% are plotted as functions of the product $P = \sqrt{\frac{1}{\int_{q_0}^{q} q'^3 \Psi^2_{\frac{p_0}{J}}(q') C(q') dq'}} \times \frac{p_0}{J}$. Following Persson approximation i)

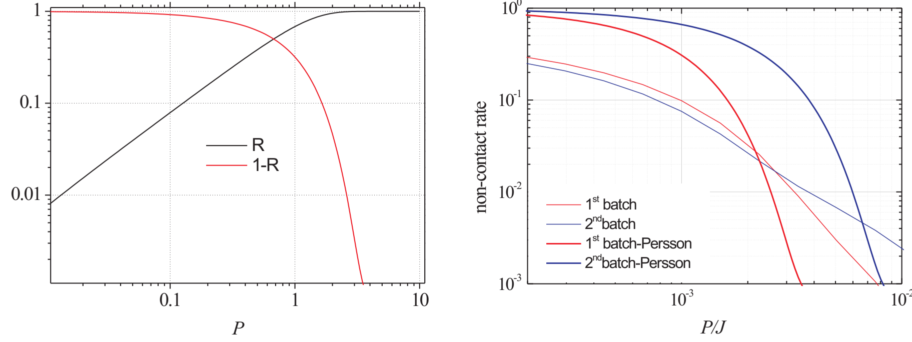

Figure A.1: (left) Behavior of the rate of contact and of its complement to 100% as functions of normal stress p_0. (right) Comparison of the predictions of the Persson's theory and of the theory developed in section 4.2 for the first and the second batch of samples at our disposition.

$\Psi^2_{\frac{p_0}{J}}(q) = 1$, and stating ii) $p_0 << J$, it holds the noticeable approximation:

$$R(q) = \sqrt{\frac{2}{\pi \int_{q_0}^{q} q'^3 C(q')\, dq'}} \times \frac{p_0}{J}, \tag{A.31}$$

which states the proportionality between the rate of contact and the normal stress in case of small loads. In my opinion the two statements i) and ii) are mutually incompatible, and the real behavior of $R(q)$ for small loads depends also on the effective form assumed by the function $\Psi^2_{\frac{p_0}{J}}(q)$, probably giving a power low in p_0/J. Nevertheless, for high values of the load, the approximation $\Psi^2_{\frac{p_0}{J}}(q) = 1$ can be considered as well founded, and the corresponding values of $R(q)$, in Eq. A.30, are probably a good approximation.

At this point, we can try to compare the predictions of the theory exposed in section 4.2 with those of Persson's theory. The form found for the function $C(q)$ involve the correlation function $\langle h(\mathbf{x})\, h(\mathbf{0})\rangle$, which is very useful, for instance, when only the fractal properties of a surface are known. In our case we dispose of detailed 2-dimensional maps of the specific diamond and silicon surfaces to be bonded, and

a little more analysis will allow us to find a more useful expression. The integral at the exponent in Eq.A.30 can be written as

$$\int_{q_0}^{q} q'^3 C\left(q'\right) dq' = \int d^2\mathbf{x} \left\langle h\left(\mathbf{x}\right) h\left(\mathbf{0}\right)\right\rangle \frac{1}{\left(2\pi\right)^2} \int_{q_0<|\mathbf{q}|<q} d^2\mathbf{q} \cdot q^2 e^{-i\mathbf{q}\cdot\mathbf{x}}. \tag{A.32}$$

If the integral in the wavevector $\mathbf{q}$ were extended to the whole plane, it whould equal the laplacian of the Dirac distribution, in our case, we can define a "smoothed" laplacian $\triangle_q$ in this way:

$$\triangle_q F\left(x, y\right) \equiv \frac{1}{\left(2\pi\right)^2} \int_{q_0<|\mathbf{q}|<q} d^2\mathbf{q} \cdot q^2 F\left(\mathbf{x}\right) e^{-i\mathbf{q}\cdot\mathbf{x}}. \tag{A.33}$$

In this way, Eq.A.32 takes the form:

$$\int_{q_0}^{q} q'^3 C\left(q'\right) dq' =< \triangle_q h\left(\mathbf{0}\right) \cdot h\left(\mathbf{0}\right) > . \tag{A.34}$$

As an example of simple application of Eq.A.34, let us suppose the profile $h\left(\mathbf{x}\right)$ to be of a sinusoidal type with wavelength λ and amplitude h_0. In this case, if $q >> \frac{2\pi}{\lambda}$ the expression A.34 assume the value $\left(\pi\frac{h_0}{\lambda}\right)^2$. A look to the plot of Fig.4.1 reveals that an almost total contact is reached if p_0 exceed some units times $\pi\frac{h_0}{\lambda}J$. This analysis is confirmed also by the exact solution of the sinusoidal problem, as reported in section 4.2.

Expression A.34 allows a drastic simplification for the calculations of the rate of contact when the profile is described in term of a matrix h_{ij}. If we define a discretized laplacian as $\triangle^k$:

$$\triangle^k h_{ij} = \frac{h_{i+k,j} + h_{i,j+k} - 4h_{ij} + h_{i-k,j} + h_{i,j-k}}{k^2 \Delta x^2}, \tag{A.35}$$

we can write the rate of contact, at the resolution k, as

$$R_k = \frac{2}{\pi} \int_0^{\infty} \frac{\sin x}{x} \exp\left(-x^2 \frac{1}{2} \left(\frac{J}{p_0}\right)^2 \left\langle \triangle^k h_{00} \cdot h_{00} \right\rangle\right) dx. \tag{A.36}$$

I calculated the value of $\left\langle \triangle^k h_{00} \cdot h_{00} \right\rangle$ for a set of surfaces profile of the first and the second batch of diamond samples that we had at our disposition. I found values of 0.00098 and 0.0023, respectively, which gives curves of the R_k (with $k = 1$) as a functions of p_0/J which are represented in figure A.1 (right), together with the corresponding curves determined by the theory exposed in section 4.2. Persson's theory gives a same shape of the curve, with an horizontal translation which extent depends on the characteristics of the sample. In this case, the second batch,

giving a higher value of $\left\langle \triangle^k h_{00} \cdot h_{00} \right\rangle$ (due mainly to the high spatial-frequencies behavior) results to perform worser than the first one, loosing the indication of a better behavior at the lower pressures. The two theories, letting aside the position of the elbow, which is approximately correct, seems to predict quite different behaviors. An experimental investigation, for instance by development of the silicon raman shift method outlined in section 4.4, could help to discriminate the correct theoretical approach.

Appendix B

Additional proofs to chapter 6

B.1 Swelling and optical path difference

We have to show that the complex optical path difference ($COPD$) due to the variation of the refractive index only, in its real and imaginary part, depends on the measured one ($COPD_m$) and on the swelling height h in the following way:

$$COPD = COPD_m - (\widehat{n}_0 - 1)\, h. \tag{B.1}$$

Let each point, initially at the height z inside diamond, displace, as an effect of the damage, to the new height z' given by

$$z' = z + h(z). \tag{B.2}$$

so that

$$\frac{dz'}{dz} = 1 + \frac{dh}{dz} \equiv 1 + \sigma\,(z)\,. \tag{B.3}$$

Suppose $\sigma\,(z) \ll 1$ for every value of z. This is a very good approximation, in fact, the observed swelling, which is related to the function $\sigma\,(z)$ by the relation:

$$h = z'\,(0) = h\,(0) = \int_{-\infty}^{0} \frac{dh}{dz} dz = \int_{-\infty}^{0} \sigma\,(z)\, dz \tag{B.4}$$

is (at most) about 30 nm, while the region over which σ is appreciably non null has a width W_{Bragg} about 3 μm (about the full-width half maximum of the Bragg peak), so that

$$\sigma \approx \frac{h}{W_{\text{Bragg}}} \leq 0.01 \tag{B.5}$$

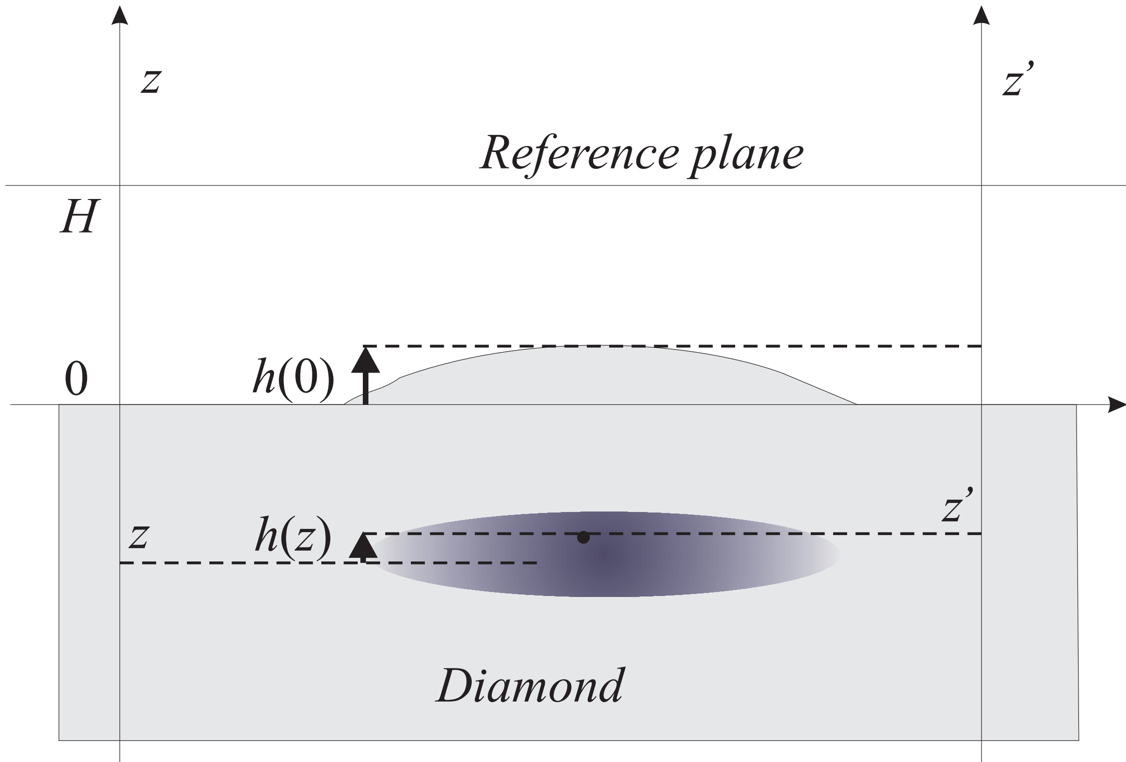

Figure B.1: Scheme of the displacement of each point inside diamond due to radiation damage. z is the height of a given point before damage, z' is the height after damage, $h(z)$ is the displacement $z' - z$.

Let now the refraction index inside diamond be

$$\widehat{n} = \widehat{n}_0 + \Delta\widehat{n}, \tag{B.6}$$

where $\widehat{n}_0$ is the refraction index of un-damaged diamond. Our experimental results indicate that

$$\left|\frac{\Delta\widehat{n}}{\widehat{n}_0}\right| \leq \frac{0.11}{2.41} \approx 0.05. \tag{B.7}$$

If we assume that the variation of the refraction index over distances of the order of $h(z)$ (less then 30 nm) is very small, we can write:

$$\widehat{n}(z') = \widehat{n}_0 + \Delta\widehat{n}(z + h(z)) \cong \widehat{n}_0 + \Delta\widehat{n}(z) + \frac{d\Delta\widehat{n}}{dz} h(z) \cong \widehat{n}_0 + \Delta\widehat{n}(z). \tag{B.8}$$

Now, the measured $COPD$ ($COPD_m$) is given by the difference between the optical

path *inside* and *outside* the damaged area, so we can write

$$COPD_m = \left[\int_{-\infty}^{h} \widehat{n}\left(z'\right)dz' + \int_{h}^{H} dz'\right] - \left[\int_{-\infty}^{0} \widehat{n}_0 dz' + \int_{0}^{H} dz'\right]. \quad \text{(B.9)}$$

Were H is the distance between the undamaged free surface of diamond and a reference plane (see also figure B.1) The first integral of Eq.B.9 can be written as

$$\int_{-\infty}^{h} \widehat{n}\left(z'\right)dz' = \int_{-\infty}^{0} \widehat{n}\left(z'\right)\frac{dz'}{dz}dz = \int_{-\infty}^{0} \left(\widehat{n}_0 + \Delta\widehat{n}\left(z\right)\right)\left(1+\sigma\left(z\right)\right)dz =$$
$$\int_{-\infty}^{0} \widehat{n}_0 dz + \int_{-\infty}^{0} \Delta\widehat{n}\left(z\right)dz + \widehat{n}_0\int_{-\infty}^{0} \sigma\left(z\right)dz + \int_{-\infty}^{0} \Delta\widehat{n}\left(z\right)\sigma\left(z\right)dz. \quad \text{(B.10)}$$

If $\Delta\widehat{n}$ and σ are, as previously assumed, small compared with the unit, their product (which is lesser than about 0.0005) in the last integral can be neglected. Thus, considering $COPD = \int_{-\infty}^{0} \widehat{n}\left(z\right)dz$ and $h = \int_{-\infty}^{0} \sigma\left(z\right)dz$, the equation B.9 can be written as

$$\begin{aligned} COPD_m = & \left[\int_{-\infty}^{0} \widehat{n}_0 dz + \int_{-\infty}^{0} \Delta\widehat{n}\left(z\right)dz + \widehat{n}_0\int_{-\infty}^{0} \sigma\left(z\right)dz + \int_{h}^{H}\right] - \\ & \left[\int_{-\infty}^{0} \widehat{n}_0 dz + \int_{0}^{H} dz\right] = \\ & \int_{-\infty}^{0} \widehat{n}_0 dz + COPD + \widehat{n}_0 h + (H-h) - \int_{-\infty}^{0} \widehat{n}_0 dz - H = \\ & COPD - \left(\widehat{n}_0 - 1\right)h \end{aligned} \quad \text{(B.11)}$$

which is what we had to prove.

B.2 Fluence calculation

I prove here that if the raster scanning of each implanted region Ω is uniform and if the dimensions L of the square region are much wider than the beam width l, we can assume that the fluence in the central region equals the ratio of the deposited charge Q to the area A_Ω scanned by the center of the beam. In fact, given $\phi\left(\mathbf{x}\right) = \frac{d^2q}{dSdt}$ the distribution of the beam current density, the fluence at a give position $\mathbf{y}$ is

$$\phi\left(\mathbf{y}\right) = \int_{0}^{T} \phi\left(\mathbf{y} - \mathbf{x}\left(t\right)\right)dt = \int_{0}^{T} dt\frac{1}{A_\Omega}\int_{\Omega} \phi\left(\mathbf{y}-\mathbf{x}\right)d^2\mathbf{x}. \quad \text{(B.12)}$$

If $\phi\left(\mathbf{x}\right) = 0$ for $|\mathbf{x}| > r$ and $\mathbf{y}$ is chosen in such way that $|\mathbf{y}-\mathbf{x}| > r$ for every $\mathbf{x}$ not belonging to the region Ω, thus $\int_\Omega \phi\left(\mathbf{y}-\mathbf{x}\right)d^2\mathbf{x} = \frac{dq}{dt}$ and

$$\phi\left(\mathbf{y}\right) = \frac{1}{A_\Omega}\int_{0}^{T} \frac{dq}{dt}dt = \frac{Q}{A_\Omega}, \quad \text{(B.13)}$$

as we had to prove.

Acknowledgments

I wish, at the end of my Ph. D. program, to acknowledge the contributions which made possible this work.

First of all, a special thank goes to my tutor, Dr. Silvio Sciortino, who gave me an essential help in the experimental work and contributed with frequent and useful discussions to the modelistic and theoretical efforts at the basis of a large part of this dissertation.

Then, Prof. Giuliano Parrini, who formed, together with Dr. Sciortino and me, the nucleus of the group that started the activity with Silicon-On-Diamond (SOD) in Florence, and which contributed to the project in all its phases with original ideas, material work and useful discussions.

Several Researchers of the LENS (European Laboratory of Nonlinear Spectroscopy) laboratories gave us an unreplaceable help in the fabrication and characterization of SOD samples. Prof. Roberto Bini made available the resources of the Matter Under Extreme Conditions laboratories for all the fabrication activities and most of the characterization analyses. Dr. Margherita Citroni gave us the necessary help in the laser bonding of the silicon and diamond samples. Dr. Mario Santoro and Dr. Federico Gorelli gave an absolutely essential contribution in the phase of the spectroscopic characterization of the Silicon-On-Diamond samples. Dr. Gabriele Ferrari helped in the characterization of the laser beam. All these researchers gave also contributions in term of ideas to the definition of the project.

Ing. Alessio Fossati contributed to the design of many mechanical parts which were necessary in SOD Fabrication.

Prof. Molesini, Dr. Maurizio Vannoni and Mr. Andrea Sordini, of the National Institute of Optics (INO), gave an invaluable help in the optical characterization of the diamond and silicon samples, moreover, their experience was useful in the definition of the cleaning and mounting procedures of the silicon and diamond samples.

Mr. Mirko Brianzi gave us an invaluable technical support during all the time of this Ph. D. work.

The local section of the National Institute of Nuclear Physics, especially in the person of its director Prof. Pier Andrea Mandò, supported us in terms of funding and technical support.

A very profitable collaboration with the Laboratorio Beni Culturali (LABEC) of Florence and with the Experimental Physics Department and INFN of Turin allowed the fulfillment of a research program in the field of ion-beam optical modification of diamond samples. I wish to thank here the researchers whom I worked with during these three years: Dr. Lorenzo Giuntini, which was one of my college colleagues a long time ago, together with Dr. Silvio Sciortino whom I have already mentioned above, Dr. Silvia Calusi, Dr. Mirko Massi, Dr. Paolo Olivero, Dr. Federico Bosia, Prof. Enrico Vittone.

I also wish to thank Dr. Paola Verrucchi for her revision of the fifth chapter, a necessary introduction, in my view, to the experimental work done in the study of ion-induced modification of the optical characteristics of diamond.

I do not want to neglect the contribution of the Italian Ministry of Public Instruction, which gave me a three year permit to fulfill my Ph. D. program, and of the Istituto Statale di Istruzione Superiore Tecnica e Liceale Russell-Newton, which forwent my work during the same amount of time.

To my wife Elsa goes my gratitude for her esteem, encouragement, support and sympathy during this long period of work, and to all my relatives and friends for their sympathy and esteem.

At the end, but not least, I want to acknowledge the contribution of Someone who I believe to be behind every sincere attempt to draw slightly ahead the subtle line which separates knowledge from ignorance. *"To God only wise, be glory through Jesus Christ for ever"*. (Epistle to Romans, chapter 16, verse 27)

Bibliography

[1] J.R. Powell. *Proc. Of IEEE*, 96 (8):1247, 2008.

[2] D.A. Muller. A sound barrier for silicon? *Nature Materials*, 4:645–647, september 2005.

[3] G.K. Celler and S. Cristoloveanu. Frontiers of silicon-on-insulator. *Journal of Appl. Phys.*, 93 (9):4955, 2003.

[4] A. Aleksov, J. M. Gobien, X. Li, J. T. Prater, and Z. Sitar. Silicon-on-diamond an engineered substrate for electronic applications. *Diamond Relat. Mater.*, 15:248–253, 2006.

[5] Ming Zhu, Paul K Chu, Xuejie Shi, Man Wong, Weili Liu, and Chenglu Lin. Formation of silicon-on-diamond by direct bonding of plasma-synthesized. *Appl. Phys. Lett.*, 85 (13):2532–2534, 2004.

[6] P. K. Chu. *IEEE Circuits and Systems Magazine*, 5:18, 2005.

[7] Katerina Raleva, Dragica Vasileska, and Stephen M. Goodnick. *IEEE Electron Device Letters*, 29:621, 2008.

[8] A.V. Sukhadolau, E.V. Ivakin, V.G. Ralchencko, A.V. Khomich, A.V. Vlasov, and A.F. Popovich. Thermal conductivity of cvd diamond at elevated temperatures. *Diamond and Relat. Mater.*, 14:589–593, 2005.

[9] J. Philip, P. Hess, T. Feygelson, J. E. Butler, S. Chattopadhyay, K. H. Chen, and L. C. Chen. Elastic, mechanical, and thermal properties of nanocrystalline diamond films. *Journal of Appl. Phys.*, 93 (4):2164–2171, 2003.

[10] Tsuneyuki Yamane, Naoto Nagai, Shin ichiro Katayama, and Minoru Todoki. Measurement of thermal conductivity of silicon dioxide thin films using a 3-omega method. *J. Appl. Phys.*, 91:9772–9776, 2002.

[11] A. BenMoussa, A. Theissena, F. Scholzeb, J.F. Hochedeza, U. Schuhlec, W. Schmutzd, K. Haenene, Y. Stockmang, A. Soltani, D. McMullini, R.E. Vestj, U. Krothb, C. Laubisb, M. Richterb, V. Mortete, S. Gissota, V. Delouillea, M. Dominiquea, S. Kollerd, J.P Halaing, Z. Remese, R. Petersenf, M. DOlieslaeger, , and J.-M. Defise. Performance of diamond detectors for vuv applications. *Unknown Journal*, 568:398–405, 2006.

[12] M. Rebisz-Pomorska, D. Tromson, A. Isambert, B. Marczewska, and P. Bergonzo. Single crystal chemical vapor deposited diamond detectors

for intensity-modulated radiation therapy applications. *J. Appl. Phys.*, 106:084509, 2009.

[13] RD42. Cern collaboration: Development of diamond tracking detectors for high luminosity experiments at the lhc. *http://greybook.cern.ch/programmes/experiments/RD42.html.*

[14] RD50. Cern collaboration: Radiation hard semiconductor devices for very high luminosity colliders. *http://rd50.web.cern.ch/rd50/.*

[15] RD39. Cern collaboration: development of super-radiation hard cryogenic silicon detectors. *http://www.hip.fi/research/cms/tracker/RD39/php/home.php.*

[16] N. Wermes. Pixel detectors for charged particles. *Nucl. Instrum. Methods Phys. Res. A*, 604:370, 2009.

[17] K. Bakowicz and J. Mitura. *Wide Bandgap Mater.*, 9:261–272, 2009.

[18] P. Ariano, A. L. Giudice, A. Marcantoni, E. Vittone, E. Carbone, and D. Lovisolo. A diamond-based biosensor for the recording of neuronal activity,. *Biosens. Bioelectron.*, 24:2096, 2009.

[19] M. Bonnauron, S. Saada, L. Rousseau, G. Lissorgues, C. Mer, and P. Bergonzo. High aspect ratio diamond microelectrode array for neuronal activity measurements. *Diamond Relat. Mater.*, 17:1399, 2008.

[20] T.N. Rao and A. Fujishima. *Diamond and Relat. Mater.*, 9:384, 2000.

[21] F. Maier, M. Riedel, B. Mantel, J. Ristein, and L. Ley. Origin of surface conductivity in diamond. *Phys. Rev. Lett.*, 85:3472–3475, 2000.

[22] Kenta Sugata, Minoru Tachiki, Tohru Fukuda, Hokuto Seo, and Hiroshi Kawarada. Nanoscale modification of the hydrogen-terminated diamond surface using atomic force microscope. *Jpn. J. Appl. Phys*, 41:4983–4986, 2002.

[23] T. V. Kononenko, M. S. Komlenok, V. P. Pashinin, S. M. Pimenov, V. I. Konov, M. Neff, V. Romano, and W. Lthy. Femtosecond laser microstructuring in the bulk of diamond. *Diamond Relat. Mater.*, 18:196–199, 2008.

[24] R. Walker, S. Prawer, D. N. Jamieson, K. W. Nugent, and R. Kalish. Formation of buried p-type conducting layers in diamond. *Appl. Phys. Lett.*, 71:1492–1494, 1997.

[25] A. Hartl, E. Schmich, J.A. Garrido, J.Hernando, S. C. R. Catharino, S.Walter, P. Feulner, A. Kromka, D. Steinmuller, and M. Stutzmann. Protein-modified nanocrystalline diamond thin films for biosensor applications. *Nature Materials*, 3:736, 2004.

[26] A. Argoitia T. Suzuki. Current status of the heteroepitaxy of cvd diamond. *Phys. Stat. sol. (a)*, 154:239, 1996.

[27] X. Jiang and C.P. Klages. Recent developments in heteroepitaxial nucleation and growth of diamond on silicon. *Phys. Stat. sol. (a)*, 154:175, 1996.

[28] A. Aleksov, X. Li, N. Govindaraju, J.M. Gobien, S.D. Wolter, J.T. Prater, and Z. Sitar. Silicon-on-diamond: An advanced silicon-on-insulator technology. *Diamond Relat. Mater.*, 14:308–313, 2005.

[29] J. Widiez, M. Rabarot, S. Saada, J.-P. Mazellier, J. Dechamp, V. Delaye, J.-C. Roussin, F. Andrieu, O. Faynot, S. Deleonibus, P. Bergonzo, and L. Clavelier. Fabrication of silicon on diamond (sod) substrates by either the bonded and etched-back soi (besoi) or the smart-cut technology. *Solid State Electronics l*, 54 (2):158–163, 2010.

[30] A. Kaiser, D. Kueck, P. Benkart, A. Munding, G.M. Prinz, A. Heittmann, H. Huebner, R. Sauer, and E. Kohn. Concept for diamond 3-d integrated uv sensor. *Diamond Relat. Mater.*, 15:1967–1971, 2006.

[31] V. Kasarev, V. Kryukov, M. Kuznetsov, S. M. Pintus, M. A. Lamin, O. Pchelyakov, and L.V.Sokolov. Growth of silicon on diamond substrates. *Russian Microelectronics*, 34:37, 2005.

[32] G.N. Yushin, S.D. Wolter, A.V. Kvit, R. Collazo, B.R. Stoner, J.T. Prater, and Z. Sitar. Study of fusion bonding of diamond to silicon for silicon-on-diamond technology. *Appl. Phys. Lett.*, 81:3275–3277, 2002.

[33] G.N. Yushin, A. Aleksov, S.D. Wolter, F. Okuzumi, J.T. Prater, and Z. Sitar. Wafer bonding of highly oriented diamond to silicon. *Diamond Relat. Mater.*, 13:1816–1821, 2004.

[34] G. A. Slack and J. Bartram. Thermal expansion of some diamondlike crystals. *J. Appl. Phys.*, 46 (1):89–98, 1975.

[35] Y. Okada and Y. Tokumaru. Precise determination of lattice parameter and thermal expansion coefficient of silicon between 300 and 1500 k. *J. Appl. Phys.*, 56 (2):314–320, 1984.

[36] B.N.J. Persson. Theory of rubber friction and contact mechanics. *Journal of Chemical Physics*, 115:3840, 2001.

[37] J. Wagner, C. Wild, and P. Koidl. Resonance effects in raman scattering fromo polycrystalline diamond films. *Appl. Phys. lett.*, 59:779–781, 1991.

[38] R.E. Shroeder, R.J. Nemanich, and J.T. Glass. Analysis in the composite structures in diamond thin films by raman spectroscopy. *Phys. Rev. B*, 41:3738–3745, 1990.

[39] M.H. Brodsky, Manuel Cardona, and J.J. Cuomo. Infrared and raman spectra of the silicon-hydrogen bonds in amorphous silicon prepared by glow-discharge and sputtering. *Phys. Rev. B*, 16:3556–3571, 1977.

[40] Z. Iqbal and S. Veprec. *Journal of Physics C*, 15:377, 1982.

[41] E. Bustarret, M.A. Hachica, and M. Brunel. Experimental determination of the nanocrystalline volume fraction in silicon thin films from raman spectroscopy. *Appl. Phys. Lett.*, 52:1675–1677, 1988.

[42] M. Friedrich, S. Morley, B. Maintz, S. Deutchmann, D.R.T. Zahn, and V. Hoffermann. Detection of ultrathin sic layer by infrared spectroscopy. *Phys. stat. sol. (a)*, 145:369–377, 1994.

[43] Stefano Lagomarsino. Phenomenological model of silicon-on-diamond laser bonding. *submitted to Diamond and Related Materials*, 2010.

[44] P. Baeri and E. Rimini. *Materials Chemistry and Physics*, 46:169, 1996.

[45] S. Lagomarsino, G. Parrini, S. Sciortino, M. Santoro, M. Citroni, M. Vannoni, A. Fossati, F. Gorelli, G. Molesini, and A. Scorzoni. *Appl. Phys. Lett.*, 1:1, 2010.

[46] A.I. Savvatimskiy. *Carbon*, 43:1115, 2005.

[47] F.V. Bunkin and M.I. Tribelskii. *Sov. Phys. Usp.*, 23:105, 1980.

[48] J. H. Yoo, S. H. Jeong, X. L. Mao, R. Greif, and R. E. Russo. *Appl. Phys. Lett.*, 76:783, 2000.

[49] E.J. Yoffa. *Phys. Rev. B*, 21:2415, 1980.

[50] T. Sjodin, H. Petek, and H.L. Dai. *Phys. Rev. Lett.*, 81:5664, 1998.

[51] P.L. Silvestrelli, A. Alavi, M. Parrinello, and D. Frenkel. *Phys. Rev. Lett.*, 77:3149, 1996.

[52] A.Lietoila and J. F. Gibbons. *Journal of Applied Physics*, 53:3207, 1982.

[53] D. Agassi. *Journal of Applied Physics*, 55:4376, 1984.

[54] J. Sik, J. Hora, and J. Humlicek. *Journal of Applied Physics*, 84:6291, 1998.

[55] Jr. G. E. Jellison and D. H. Lowndes. *Appl. Phys. Lett.*, 51:352, 1987.

[56] K.P. O'Donnell and X. Chen. *Appl. Phys. Lett.*, 58:2924, 1991.

[57] C. J. Glassbrenner and G. A. Slack. *Phys. Rev.*, 134:A1058, 1964.

[58] J. R. Olson, R. O. Pohl, J. W. Vandersande, A. Zoltan, T. R. Anthony, and W. F. Banholzer. *Phys. Rev. B*, 47:14850, 1987.

[59] Hidekazu Kobatake, Hiroyuki Fukuyama, Izuru Minato, and Takao Tsukada andSatoshi Awaji. *Journal of Applied Physics*, 104:054901, 2008.

[60] L. E. Fried and W. M. Howard. *Phys. Rev. B*, 61:8734, 2000.

[61] A. S. Okhotin, A. S. Pushkarskii, and V. V. Gorbachev. *Thermophysical Properties of Semiconductors.* Atom Publ. House, Moscow, 1972.

[62] Won-Kyu Rhim and Kenichi Ohsaka. *Journal of cristal growth*, 208:313, 2000.

[63] C.C. Yang, J.C. Li, and Q. Jiang. *Solid State Communications*, 129:437, 2004.

[64] A. J. Sabbah and D. M. Riffe. *Phys. Rev. B*, 66:165217, 2002.

[65] Stephen Y. Chou, Chris Keimel, and Jian Gu. Ultrafast and direct imprint of nanostructures in silicon. *Nature*, 417:835–837, 2002.

[66] H. R. Hertz. Ueber die beruehrung elastischer koerper. *Gesammelte Werke*, 1, 1895.

[67] F.P. Bowden and D. Tabor. The area of contact between stationary and between moving surfaces. *Proceedings of the Royal Society of London*, 169(938):391–413, 1939.

[68] J.F. Archard. Elastic deformation and the laws of friction. *Proceedings of the Royal Society of London*, 243(1233):190–205, 2010.

[69] B. N. J. Persson, F. Bucher, and B. Chiaia. Elastic contact between randomly rough surfaces: Comparison of theory with numerical results. *Phys. Rev. B*, 65:184106, 2002.

[70] B. N. J. Persson. Adhesion between elastic bodies with randomly rough sur-

faces. *Phys. Rev. Lett.*, 89:245502, 2002.

[71] E. Anastassakis, A.Pinczuk, E. Burstein, F. H. Pollak, and M. Cardona. Effect of static uniaxial stress on the raman spectrum of silicon. *Solid State Communications*, 8:133–138, 1970.

[72] M. Holtz, J.C. Carty, and W.M. Duncan. Ultraviolet raman stress mapping in silicon. *Applied Physics Letters*, 74:2008, 1999.

[73] J.I. Cirac and P. Zoller. Quantum computation with cold trapped ions. *Physical Review Letters*, 74:4091, 1995.

[74] R.A. Campos, B.E.A. Saleh, and M.C. Teich. Quantum mechanical lossless beam splitter: Su(2) symmetry and photon statistics. *Phys. Rev. A*, 40:1371, 1989.

[75] I.L. Chuang and Y. Yamamoto. Simple quantum computer. *Phys. Rev. A*, 52:3489, 1995.

[76] Q.A. Turchette, C.J. Hood, W. Lange, H. Mabuchi, and H.J. Kimble. Measurement of conditional phase shifts for quantum logic. *Physical Review Letters*, 25:4710, 1995.

[77] Y. Nakamura, Y.A. Pashkin, and J.S. Tsai. *Nature*, 398:786, 1999.

[78] G.K. Brennen, C.M. Caves, P.S. Jessen, and I.H. Deutsch. Quantum logic gates in optical lattices. *Physical Review Letters*, 82:1060, 1999.

[79] D. Kielpinski, C. Monroe, and D. J. Wineland. Architecture for a large-scale ion-trap computer. *Nature*, 417:709, 2002.

[80] Daniel Loss and David P. DiVincenzo. Quantum computation with quantum dots. *Phys. Rev. A*, 57:120, 1998.

[81] Miro Kroutvar, Yann Ducommun, Dominik Heiss, Max Bichler, Dieter Schuh, Gerhard Abstreiter, and Jonathan J. Finley. Optically programmable electron. *Nature*, 432:81, 2004.

[82] B.E. Kane. A silicon-based nuclear spin quantum computer. *Nature*, 393:133, 1998.

[83] Pieter Kok and Brendon W. Lovett. Qubits in the pink. *Nature*, 444:49, 2006.

[84] Steven Prawer and Andrew D. Greentree. Diamond for quantum computing. *Science*, 320:1601, 2010.

[85] Eduard C. Reynhardt and Grant L. High. Dynamic nuclear polarization of diamond. i. solid state and thermal. *Journal of Chemical Physics*, 109:4090, 1998.

[86] T. A. Kennedy, J. S. Colton, J. E. Butler, R. C. Linares, and P. J. Doering. Long coherence times at 300 k for nitrogen-vacancy center spins in diamond grown by chemical vapor deposition. *Applied Physics Letters*, 83:4190, 2003.

[87] A. Lenef, S. W. Brown, D. A. Redman, S. C. Rand, J. Shigley, and E. Fritsch. Electronic structure of the n-v center in diamond: Experiments. *Physical Review B*, 53:13427, 1996.

[88] Igor Aharonovich, Chunyuan Zhou, Alastair Stacey, Julius Orwa, Stefania

Castellett, David Simpson, Andrew D. Greentree, Franois Treussart, Jean-Francois Roch, and Steven Prawer. Enhanced single-photon emission in the near infrared from a diamond color center. *Phys. Rev. B*, 79:235316, 2009.

[89] Igor Aharonovich, Stefania Castelletto, Brett C. Johnson, Jeffrey C. McCallum, David A. Simpson, Andrew D. Greentree, and Steven Prawer. Chromium single-photon emitters in diamond fabricated by ion implantation. *Phys. Rev. B*, 81:121201, 2010.

[90] Chunlang Wang, Christian Kurtsiefer, Harald Weinfurter, and Bernd Burchard. *Journal of Physics B: Atomic, Molecular and Optical Physics*, 39:37, 2006.

[91] E. Gu, H. W. Choi, C. Liu, C. Griffin, J. M. Girkin, I. M. Watson, M. D. Dawson, G. McConnell, and A. M. Gurney. Reflection transmission confocal microscopy characterization of single-crystal diamond microlens arrays. *Applied Physics Letters*, 84:2754, 2004.

[92] Mark P. Hiscocks, Christopher J. Kaalund, Franois Ladouceur, Shane T. Huntington, Brant C. Gibson, Steven Trpkovski, David Simpson, Eric Ampem-Lassen, Steven Prawer, and James E. Butler. Reactive ion etching of waveguide structures in diamond. *Diamond and Related Materials*, 17:1831, 2008.

[93] Mark P. Hiscocks, Kumaravelu Ganesan, Brant C. Gibson, Shane T. Huntington, Franois Ladouceur, and Steven Prawer. Diamond waveguides fabricated by reactive ion etching. *Optics Express*, 16:19512, 2010.

[94] T. M. Babinec, B. J. M. Hausmann, M. Khan, Y. Zhang, J. R. Maze, P. R. Hemmer, and M. Loncar. Unknown title. *Nature Nanotechnology*, 5:195, 2010.

[95] B. J. M. Hausmann, M. Khan, Y. Zhangn, T. M. Babinec, K. Martinick, M. McCutcheon, P. R. Hemmer, and M. Loncar. Unknown title. *Diamond and Related Materials*, 19:621, 2010.

[96] T. M. Babinec, J. T. Choy, K. J. M. Smith, M. Khan, and M. Loncar. Unknown title. *arXiv:1008.1431v1 [quant-ph]*, 2010.

[97] J. P. Hadden, J. P. Harrison, A. C. Stanley-Clarke, L. Marseglia, Y L. D. Ho, B. R. Patton, J. L. OBrien, and J. G. Rarity. *arXiv:1006.2093v1 [quant ph]*, 2010.

[98] C. F. Wang, Y-S. Choi, J. C. Lee, E. L. Hu, J. Yang, and J. E. Butler. Observation of whispering gallery modes in nanocrystalline diamond microdisks. *Applied Physics Letters*, 90:081110, 2007.

[99] M. A. Nielsen and I.L. Chuang. *Quantum Computation and Quantum Information*. Cambridge University Press, 2000.

[100] Carl Pomerance. A tale of two sieves. *Notices of the AMS*, 43:1473, 1996.

[101] R.F. Service. *Science*, 329:5592, 2010.

[102] S. Snjezana Tomljenovic-Hanic, A. D. Greentree, C. Martijn de Sterke, and S. Prawer. Flexible design of ultrahigh-q microcavities in diamond-based photonic crystal slabs. *Optics Express*, 17:6465, 2009.

[103] C. F. Wang, R. Hanson, D. D. Awschalom, E. L. Hu, T. Feygelson, J. Yang, and J. E. Butler. Fabrication and characterization of two-dimensional photonic crystal microcavities in nanocrystalline diamond. *Applied Physics Letters*, 91:201112, 2007.

[104] G. D. Fuchs, V. V. Dobrovitski, D. M. Toyli, F. J. Heremans, and D. D. Awschalom. *Science*, 326:1520, 2009.

[105] P. Neumann, J. Beck, M. Steiner, F. Rempp, H. Fedder, P. R. Hemmer, J. Wrachtrup, and F. Jelezko. *Science*, 329:542, 2010.

[106] P. Neumann, R. Kolesov, B. Naydenov, J. Beck, F. Rempp, M. Steiner, V. Jacques, G. Balasubramanian, M. L. Markham, D. J. Twitchen, S. Pezzagna, J. Meijer, J. Twamley, F. Jelezko, and J. Wrachtrup. *Nature Physics*, 6:249, 2010.

[107] E. Togan, Y. Chu, A. S. Trifonov, L. Jiang, J. Maze, L. Childress, M. V. G. Dutt, A. S. Srensen, P. R. Hemmer, A. S. Zibrov, and M. D. Lukin. *Nature*, 466:730, 2010.

[108] Barbara A. Fairchild, Paolo Olivero, Sergey Rubanov, Andrew D. Greentree, Felix Waldermann, Robert A. Taylor, Ian Walmsley, Jason M. Smith, Shane Huntington, Brant C. Gibson, David N. Jamieson, and Steven Prawer. Fabrication of ultrathin single-crystal diamond membranes. *Advanced Materials*, 20:4793, 2008.

[109] D. M. Toyli, C. D. Weis, G. D. Fuchs, T. Schenkel, and D. D. Awschalom. *Nano Letters*, 10 (8):3168, 2010.

[110] T. van der Sar, J. Hagemeier, W. Pfaff, E. C. Heeres, T. H. Oosterkamp, and D. Bouwmeester andR. Hanson. *arXiv: 1008.4097v1 [quant-ph]*, 2010.

[111] D. Englund, B. Shields, K. Rivoire, F. Hatami, J. Vukovi, H. Park, and M. D. Lukin. *Nano Letters (in press)*, DOI: 10.1021/nl101662v, 2010.

[112] J. Meijer, B. Burchard, M. Domhan, C. Wittmann, T. Gaebel, I. Popa, F. Jelezko, and J. Wrachtrup. Generation of single color centers by focused nitrogen implantation. *Applied Physics Letters*, 87:261909, 2005.

[113] F.C. Waldermann, P. Olivero, J. Nunn, K. Surmacz, Z.Y. Wang, D. Jaksch, R.A. Taylor, I.A. Walmsley, M. Dragansk, P. Reichart, A.D. Greentree, D.N. Jamieson, and S. Prawer. Creating diamond color centers for quantum optical applications. *Diamond and Related Materials*, 16:1887–1895, 2007.

[114] R. L. Hines. Radiation damage of diamond by 20-kev carbon ions. *Phys. Rev.*, 138:A1747, 1965.

[115] K.L. Bhatia, S. Fabian, S. Kalbitzer, Ch. Klatt, W. Kratschmer, R. Stoll, and J.F.P. Sellschop. Optical effects in carbon-ion irradiated diamond. *Thin Solid Films*, 324:11, 1998.

[116] Y. Fu and N. K. A. Bryan. *Optical Engeneering*, 42:2214, 2003.

[117] H. Bjrkman, P. Rangsten, and K. Hjort. *Sensors and Actuators*, 78:41, 1999.

[118] S. Gloor, V. Romano, W. Lthy, H. P. Weber, V. V. Kononenko, S. M. Pimenov,

V. I. Konov, and A. V. Khomich. *Appl. Phys. A*, 70:547, 2000.

[119] M. G. Jubber, M. Liehr, J. L. McGrath, J. I. B. Wilson, I. C. Drummond, P. John, D. K. Milne, R. W. McCullough, J. Geddes, D. P. Higgins, and M. Schlapp. Atom beam treatment of diamond films. *Diamond and Related Materials*, 4:445, 1995.

[120] A.V. Khomich, V.I. Kovaleva, E.V. Zavedeevb, R.A. Khmelnitskiyc, and A.A. Gippius. Spectroscopic ellipsometry study of buried graphitized layers in the ion-implanted diamond. *Vacuum*, 78:583, 2005.

[121] A. A. Bettiol, S. Venugopal Rao, E. J. Teo, J. A. van Kan, and Frank Watt. Fabrication of buried channel waveguides in photosensitive glass using proton beam writing. *Applied Physics Letters*, 88:171106, 2006.

[122] Feng Chen, Lei Wang, Yi Jiang, Xue-Lin Wang, Ke-Ming Wang, Gang Fu, Qing-Ming Lu, Christian E. Rter, and Detlef Kip. Optical channel waveguides in nd:yvo4 crystal produced by o+ ion implantation. *Applied Physics Letters*, 88:071123, 2006.

[123] L. Giuntini, M. Massi, and S. Calusi. The external scanning proton microprobe of firenze: A comprehensive description. *Nuclear Instruments and Methods in Physics Research A*, 576:266, 2007.

[124] James F. Ziegler. Srim-2003. *Nuclear Instruments and Methods in Physics Research B*, 219220:10271036, 2004.

[125] E. W. Maby, C. W. Magee, and J. H. Morewood. Volume expansion of ion-implanted diamond. *Applyed Physics Letters*, 39:157, 1981.

[126] J. F. Prins, T. E. Derry, and P. F. Sellschop. Physical review b. *Volume expansion of diamond during ion implantation*, 34:8870, 1986.

[127] M. Massi, L. Giuntini, M. Chiari, N. Gelli, and P.A. Mand. The external beam microprobe facility in florence: Set-up and performace. *Nuclear Instruments and Methods in Physics Research B*, 190:276, 2002.

[128] Pier Andera Mand. Advantages and limitations of external beams in applications to arts and archeology, geology and environmental problems. *Nuclear Instruments and Methods in Physics Research Section B*, 85:815, 1994.

[129] A. M. Piegari A. K. Sytchkova, J. Bulir. Transmittance measurements on variable coatings with enhanced spatial resolution. *Chinese Optics Letters*, 2010.

[130] W. Wu and S. Fahy. Molecular-dynamics study of single-atom radiation damage in diamond. *Physical Review B*, 49:3030, 1994.

[131] C. Uzan-Saguy, C. Cytermann, R. Brener, V. Richter, M. Shaanan, and R. Kalish. Damage threshold for ion-beam induced graphitization of diamond. *Applied Physics Letters*, 67:1194, 1995.

[132] P. Olivero, S. Rubanov, P. Reichart, B. C. Gibson, S. T. Huntington, J. R. Rabeau, A. D. Greentree, J. Salzman, D. Moore, D. N. Jamieson, and S. Prawer. Characterization of three-dimensional microstructures in single-

crystal diamond. *Diamond and Related Materials*, 15:1614, 2006.

[133] D.P. Hickey, K.S. Jones, and R.G. Elliman. Amorphization and graphitization of single-crystal diamond a transmission electron microscopy study. *Diamond and Related Materials*, 18:1353, 2009.

[134] A. V. Khomich, R. A. Khmelnitskiy, V. A. Dravin, A. A. Gippius, E. V. Zavedeev, and I. I. Vlasov. *Physics of the Solid State*, 49:1161, 2007.

[135] A.A. Bettiol, T.C. Sum, F.C. Cheong, C.H. Sow, S. Venugopal Rao, J.A. van Kan, E.J. Teo, K. Ansari, and F. Watt. A progress review of proton beam writing applications in microphotonics. *Nuclear Instruments and Methods in Physics Research B*, 231:364, 2005.

[136] I. Rajta, I. Gomez-Morilla, M.H. Abraham, and A.Z. Kiss. Proton beam micromachining on pmma, foturan and cr-39 materials. *Nuclear Instruments and Methods in Physics Research B*, 210:260, 2003.

[137] F. Munnik, F. Benninger, S. Mikhailov, A. Bertsch, P. Renaud, H. Lorenz, and M. Gmur. High aspect ratio, 3d structuring of photoresist materials by ion beam liga. *Microelectronic Engineering*, 67-68:96, 2003.

[138] T.C. Sum, A.A. Bettiol, H.L. Seng, I. Rajta, J.A. van Kan, and F. Watt. Proton beam writing of passive waveguides in pmma. *Nuclear Instruments and Methods in Physics Research B*, 210:266, 2003.

[139] S. Lagomarsino, P. Olivero, F. Bosia, M. Vannon, S. Calusi, L. Giuntini, and M. Massi. Evidence of light guiding in ion-implanted diamond. *Physical Review Letters*, 105:233903, 2010.

[140] Mark L. von Bibra and Ann Roberts. Refractive index reconstruction of graded-index buried channel waveguides from their mode intensities. *Journal of Lightwave Technology*, 15:1695, 1997.

[141] P. Olivero, S. Calusi, L. Giuntini, S. Lagomarsino, A. Lo Giudice, M. Massi, S. Sciortino, M. Vannoni, and E. Vittone. Controlled variation of the refractive index in ion-damaged diamond. *Diamond And Related Materials*, 19:428, 2009.